3D printing of composites in the Alumina-Zirconia system:

from an engineering approach for the development of

slurries to sintered samples with high microstructural properties

By

Barbara Inserra

******

Supervisors:

Prof. Jean Marc Tulliani, Supervisor

Prof. Paola Palmero, Co-Supervisor

Doctoral Examination Committee:

Prof. Valeria Cannillo, Referee, Università di Modena Reggio Emilia, Italy

Prof. Frank Kern, Referee, University of Stuttgart, Germany

Politecnico di Torino

2023

Declaration

I hereby declare that, the contents and organization of this dissertation constitute my own original work and does not compromise in any way the rights of third parties, including those relating to the security of personal data.

Barbara Inserra

2023

…‹‹Half is better than all…››, poi però é lei a
fare colpo su di me quando, per tutta risposta, mi
dice che perdere é *yin* e vincere *yang*,

    ma che perdere è il miglior modo di vincere

Carrère E., Yoga

Elio e le storie tese, *Il circo discutibile*

Acknowledgments

First and foremost, I am extremely grateful to my supervisors, Prof. Jean-Marc Tulliani and Prof. Paola Palmero for their invaluable advice, continuous support, and patience during my PhD study. I would like also to express gratitude to Dr. Bartolomeo Coppola for his treasured support which was really influential in shaping my experiment methods, he provided me knowledge and expertise. Thanks should also go to Dr. Nicola Cavallini for his precious help with the PCA, and to Prof. Paola Rivolo for her treasured support with the Raman analysis.

I am so grateful to my office mates and lab mates, for your help and moral support, you helped me without knowing it, you did it just being yourselves. Cross our paths was more than enjoyable and your friendship is a precious luck for me, gave me the chance to grew up not only as a scientist, but I grow up also as a woman. I will always remember our lunch time reading the *Promessi Sposi*, the crow that stole my cheese, the secret Santa or the mountains hiking. In these years I routed a piece of this path with a lot of people: Enrico, Tanguy, Alberto, Matteo, Claire, Julien, Alessandra. A special mention goes to Giuseppe, Mehdi, Francesca, Arianna, Alberto and Luca, I will never forget the cherished time spent together, thank you for being good friends.

I would like to express my gratitude to my family, especially to my mom and Letizia. Their belief in me has kept my spirits and motivation high during this process. I would also like to thank my cat, Little Sophie, the real breadwinner, for all the entertainment and emotional support of this 19 years.

Thank you, to Francesca and Lucio, always there for me, and always here with me. You are the family that I chose.

Thank you, Mafalda, with your happiness you get always a smile from me.

Thank you, Yo, for hold me up in this path for a while, I'm changed also thanks to you.

And finally, thank you Barbara for your resilience and your non-stop effort to be the better version of yourself, well, nobody can tell that you didn't attempt it!

Abstract

The aim of this PhD work is to explore and develop printable slurries via DLP (Digital Light Processing) Stereolithography having, as a ceramic matrix, a biphasic ($Ce_{11}ZA_{16}$) or triphasic ($Ce_{11}ZA_8Sr_8$) composite powder in the zirconia-alumina system. A powder engineering strategy made possible the tailoring of the composition, the microstructure, and the features of the final materials. The methodological approach taken allowed the exploitation of the high potentiality of the Ce-TZP composites to explore the feasibility of obtaining printable formulations for complex composition ceramics, while maintaining the morphological and microstructural characteristics that characterize such composites when obtained by conventional shaping methods, thanks to the high-resolution offered by the stereolithographic additive manufacturing technique. Extensive research in the field of stereolithography has been carried out, but it is evident the paucity of publications on Ce-TZP composites. Thus, filling the gap in the previously published studies was one of the objectives of this research joining the outstanding aging resistance of the material to the extremely high dimensional resolution of DLP-stereolithography, laying the groundwork for future biomedical application.

In the first chapter, through detailed bibliographic research, the state-of-the-art of zirconia-alumina composites obtained by additive manufacturing methods was developed, paying particular attention to the DLP-stereolithography. The first part of the chapter deals with the transformation toughening proper of zirconia and the beneficial effect of alumina addition in the powder composition and the advantageous influence of the ceria in the aging resistance of zirconia. The second part is focused on the DLP-stereolithography features of the printable slurries, the

resin, and on the removal of the organic fraction for the consolidation of the parts through debinding and sintering.

The second chapter deals with the elaboration process of $Ce_{11}ZA_{16}$ composite powders demonstrating an optimum control of the entire process. The raw powders' dispersion with the addition of the suitable dispersant (Disperbyk-103 in our case) and the proper ball milling time allows the preparation of homogeneous slurries obtaining outstanding microstructures of the fired parts.

The third chapter shows the elaboration process of $CeZA_8Sr_8$ via surface modification of a zirconia-based composite powder with inorganic precursors of the secondary phases. The final formulation contains 8 vol% of alumina and 8 vol% of an aluminate phase. The adopted approach such as the powder dispersion, addition of the dopants, spray drying, and the thermal treatments for the decomposition of the nitrates guarantees to the final composite powder to be uniformly dispersed in the acrylic resin and printed at the end. Highly dense sintered parts were then obtained.

The fourth chapter is dedicated to the development and characterization of slurries printable with DLP-stereolithography. The slurries without and after the addition of the dispersant were characterized from the point of view of the rheology, while the effect of the solid loading and the amount of dispersant on the slurry behaviour were investigated, and the characteristics of the printed parts. In the closing section of the chapter the printing process parameters, and their correlations, were studied through the Principal Components Analysis (PCA).

In the last part of the thesis, the main results of a full description of the printed parts in terms of phase composition, microstructure, and mechanical characterization of the hardness and fracture strength are presented. The adopted procedure for the preparation of the powders and the slurries was successful in developing composites

having highly homogeneous microstructures. Particularly, in the $Ce_{11}ZA_8Sr_8$ a complex microstructure was obtained with an excellent distribution of the round-shaped alumina and elongated strontium aluminate grains, as secondary phases, inside the fine zirconia matrix. A strong influence of the printing parameters and the debinding cycle on the microstructure and on the mechanical features was revealed.

I hereby declare that, the contents and organisation of this dissertation constitute my own original work and does not compromise in any way the rights of third parties, including those relating to the security of personal data.

…………………………..…………..

Barbara Inserra

Contents

Chapter 1

An overview on zirconia-based materials

The purpose of this bibliographic chapter is to report the state of the art of the 3D printing of zirconia-alumina in the literature in order to define the appropriate context of this Ph.D work. In the first part, the characteristics of the zirconia-alumina powders used to prepare the printable slurries will be described. In particular, the transformation toughening of zirconia materials will be described with particular emphasis on its effects on the mechanical properties and stability of the printed parts. A literature overview of the most relevant zirconia-containing materials is provided. The second part focuses on the production of ceramic parts through additive manufacturing techniques providing a description of the features of the slurry and its influence on the microstructure and mechanical properties of the finished parts.

1.1 Zirconia-based composites, an overview

Zirconium (Zr) is a greyish metal, with a density of 6.49 g/cm³ and melting and boiling temperatures of 1852 °C and 3580 °C, respectively. It is characterized by a hexagonal crystalline lattice. Zr does not exist in nature in pure form but combined with silicate oxide with the mineral name zircon ($ZrSiO_4$). As an oxide (ZrO_2) it is known as Baddeleyite[1].

Since ancient times, Zircon has been regarded as a gemstone. The name zirconium derives from the Arabic word *Zargon* which signifies "golden in color". In turn, the origin of the word *Zargon* comes from the two Persian terms *Zar* (Gold) and *Gun* (Color). Zirconia, the metal dioxide (ZrO_2), was discovered in 1789 by the German scientist Martin Heinrich Klaproth as by-product obtained after burning zircon gems. Zirconia has long been used as a ceramic pigment combined with rare earth oxides. In addition, due to their high-temperature ionic conductivity zirconia ceramics are excellent as solid electrolytes in fuel cells and in oxygen sensors. Helmer and Driskel published the first study on the use of ZrO_2 as a biomaterial in 1969[2]. The interest in employing zirconia as a ceramic biomaterial is due to its

excellent mechanical strength and toughness, chemical and dimensional stability, and Yoùung's modulus in the same order of magnitude of stainless steel alloys [3].

At least five known solid phases of ZrO_2 ceramics exist but under normal processing conditions (pressureless, conventional thermal cycles etc.), only three phases are observed, depending on temperature and the addition of the stabilizer [4]. The three polymorphs of zirconia are: monoclinic (m), tetragonal (t) and cubic (c) (schematic representation in figure 1.1). Pure zirconia is monoclinic at room temperature. This phase is stable up to 1170° C. Then it is tetragonal between 1170 °C and 2370 °C and cubic from 2370 °C to 2750 °C (melting point). Moreover, at lower temperature and with increasing pressure ZrO_2 exhibits two additional orthorhombic (I and -II) polymorphs [5].

T-M conversion is a reversible athermal martensitic transformation that shows important temperature hysteresis of 200 °C, a volume change of transformation strain (3-4 %) and a significant shear strain (14–15%). Sintered zirconia components, if unstabilized, are prone to disintegration [6].
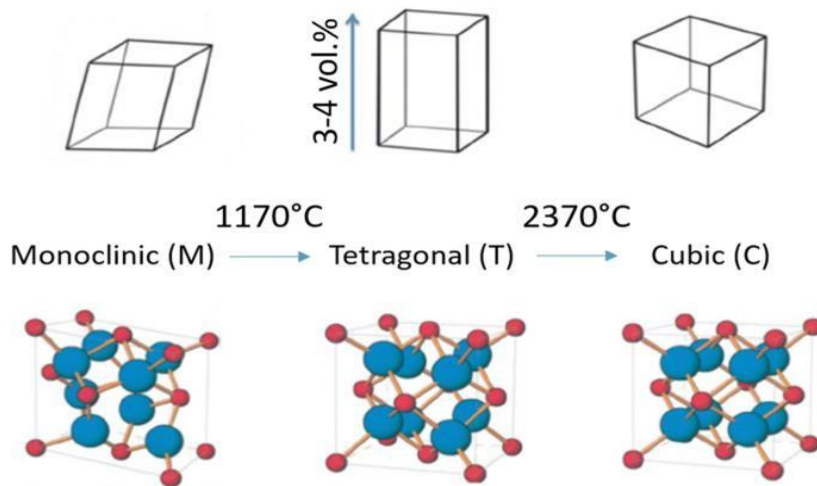
Figure 1.1 Schematic representation of the transformation of ZrO_2. From left to right the polymorphs monoclinic (M), tetragonal (T), and cubic (C) [7]

Because of the strong covalent Zr–O bond, monoclinic zirconia, from the thermodynamic point of view, is stable at lower temperatures and a sevenfold coordination number is favored. The co-ordination number of Zr^{4+} cations in tetragonal and cubic-ZrO_2 is 8.

Zirconia changes its structure to make space for the oxygen ion vacancies generated at high temperature. The structure has eightfold coordination (t or c) but the effective coordination number is near 7 due to the interaction of Zr^{4+} ions with the oxygen ion vacancies [6]. Ruff and Ebert's [7] description of the primary method for using zirconia in engineering and preventing transformation-induced cracking is still relevant today.

Tetragonal and/or cubic phase stability can be entirely or partially achieved by alloying pure zirconia with another oxide [8,9]. The stabilizer oxides form solid solutions with ZrO_2.

The monoclinic phase is the stable structure of ZrO_2 at room temperature. The introduction of stabilizing oxides, with usually lower valence cations than Zr^{4+}, like CaO, MgO, Y_2O_3, La_2O_3, Gd_2O_3, CeO_2 to zirconia-alloys can retain the high-temperature tetragonal structure, which is metastable at ambient temperature [10]. Dopant ions replace Zr^{4+} ions in the cation network, these included undersized (Fe^{3+}, Ga^{3+}) and oversized (Y^{3+}, Gd^{3+}) trivalent ions as well as undersized (Ge^{4+}) and oversized (Ce^{4+}) tetravalent ions. Oxygen unfilled sites are associated with the Zr cations for oversized dopants, and with two dopant cations in the case of undersized dopants. In both cases, the number of Zr cations coordinated by seven oxygens (rather than eight) rises, which stabilizes the tetragonal phase [4,11]

The tetragonal matrix is transformed to in the monoclinic phase when the constraint of the matrix loosens, for example when a crack advances in the material. The stress field, related to the expansion and due to the phase transformation opposes the stressfield that causes the propagation of the crack.

Since the energy involved with crack propagation is lost during the T-M transformation in overcoming the compression stresses brought on by volume expansion, toughness is increased (Fig.1.2) [3].
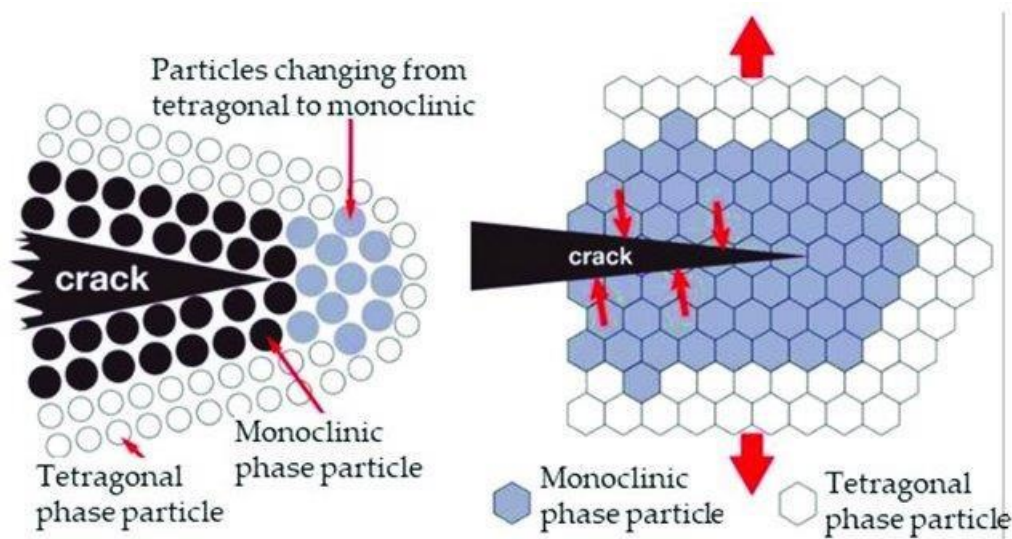
Figure 1.2 Image of stress-induced transformation toughening process [12].

The transformation toughening mechanism is the increase in fracture toughness of a material. Is the direct result of a phase transformation occurring at the tip of an advancing crack [1]. A variation in the stress intensity factor can be related to the transformation toughening mechanism (eq. 1.1)

$$\Delta K = K\, tip - K\, \infty \qquad\qquad\qquad (1.1)$$

When the applied stress ($K\infty$) is greater than the crack tip stress intensity factor (K_{tip}), crack tip shielding occurs ($\Delta K < 0$). ΔK indicates the resultant toughening effect. For a successful transformation toughening a metastable phase must be present in the material transformable to a stable one stress-induced in the crack-tip stress field. The transformation must be immediate (no long-range diffusion) and have to be related with a change of shape or volume, or both. The deviatoric nature of the transformation concede it to be stress-induced. The toughening is a crack shielding process, the transformation strains generate local stresses that oppose further crack opening. When a load is applied a stress-induced transformation happen at the crack tip producing a transformed area. The initial process zone at the tip of a stationary crack (figure 1.3a) has no net effect on the toughness of the material but, as the crack grows, a 'wake' of transformed material is left behind (figure 1.3b) leads to an increase of the toughness [1].
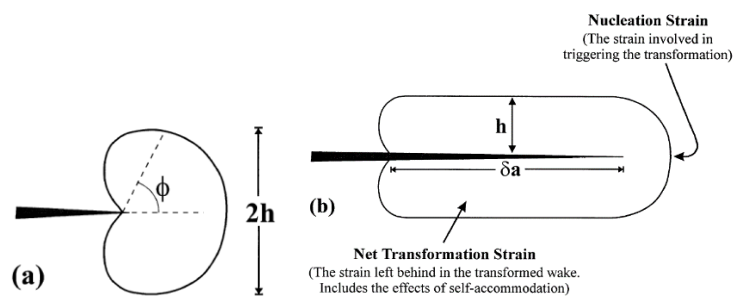
Figure 1.3 (a) Stationary crack with a cardioid shape and (b) Transformed 'wake' of half-height h, after the crack has moved forward by a distance δa.

The retention of the maximum amount of t-ZrO_2, at room temperature or at the applied temperature, is necessary for the effectiveness of the transformation toughening [13].

According to their microstructure zirconia ceramics are divided into four major categories. (Figure 1.4):

- Fully Stabilized Zirconia (FSZ) is obtained using stabilizers at high concentrations (> 8 mol% Y_2O_3). It is extensively employed, in its cubic form, for the realization of fuel cell electrolytes and oxygen sensors.

- Partially Stabilized Zirconia (PSZ) shows a cubic matrix with nanosized tetragonal or monoclinic particles precipitated having a peculiar lenticular morphology (~ 200 nm diameter and 75 nm thick). These precipitates may be present within the cubic matrix grains or at grain boundaries. PSZ ceramics are obtained by adding lime or magnesia. Mg^{2+} and Ca^{2+} divalent cations are the most common used to obtain PSZ but also YSZ can be obtained in the partially stabilized zirconia form (4-7 mol% Y_2O_3).

- Tetragonal Zirconia Polycrystals (TZP) is a material obtained by adding ceria or yttria as stabilizers. It shows ~ 100% t-ZrO_2 phase [6], even though a secondary cubic phase might be present [14]. Others strategies to stabilize the tetragonal phase is to reduce the grain size to nanoscale [15], reduction O^- vacancies or with anion lattice dopants (N, C).

- Zirconia Toughened Alumina (ZTA) is a composite consisting on polycrystalline alumina ceramic containing up to 20 vol% ZrO_2 as a dispersed phase in the tetragonal phase.

- Alumina Toughened Zirconia (ATZ) shows alumina particles in a fine zirconia matrix. ATZ is a composite obtained by the incorporation of alumina particles into the yttria-stabilized tetragonal zirconia polycrystalline (Y-TZP). Alumina provides high hardness, wear resistance, and stiffness of the alumina particles while zirconia gives high fracture toughness and strength of the Y-TZP matrix. The ATZ toughening is founded on the crack deflection around the alumina particles, stress dissipation due to the fracture mode transition from intergranular to transgranular, and crack branching and bridging by the formation of microcracks owing to the mismatch of the thermal expansion between alumina and the Y-TZP matrix [1].
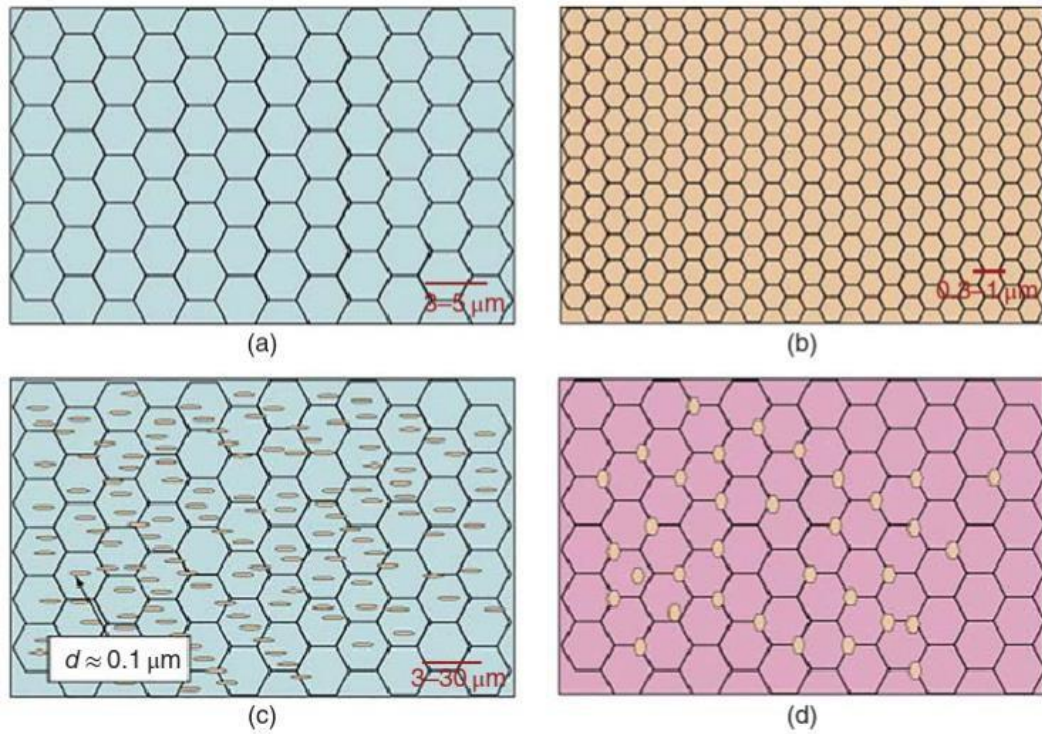
Figure 1.4 The main types of ZrO_2 ceramics and composites are represented schematically by the following microstructures: (a) cubic, fully stabilized zirconia (FSZ); (b) tetragonal zirconia polycrystal (TZP); (c) partially stabilized zirconia (PSZ), cubic matrix with tetragonal precipitates; (d) zirconia-toughened alumina (ZTA), Al_2O_3 matrix with tetragonal zirconia grains at the grain boundaries. Source [16].

1.1.1 Ceria-Doped Zirconia (Ce-TZP)

Partially stabilized zirconia (PSZ), and in particular tetragonal Zirconia polycrystalline (TZP) ceramics show remarkable mechanical properties such as high bending strength and fracture toughness. The most prominent TZP members are yttria-stabilized zirconia (Y-TZP) and ceria-stabilized zirconia (Ce-TZP) [17].

In this study, it was chosen to develop printable slurries starting from Ce-TZP as a starting powder because it shows, besides the very high resistance to corrosion of ceramics material in general, an excellent Low-Temperature Degradation (LTD) resistance [9]. The low-temperature ageing resistance is a phenomenon observed for the first time by Kobayashi [18] in 1981.

The nature of cerium as a tetravalent cation guarantees the charge neutrality of the system, since it leads to any oxygen vacancies formation. For this reason, the use of trivalent dopants such in Y-TZP materials, may be disadvantageous due to the susceptibility of the material to humid environments. This phenomenon is due to the uptake of hydroxyl (OH^-) compounds into oxygen vacancy sites which counteracts the stabilization. In wet conditions, the t/m transformation may happen without having been triggered by mechanical stress [19]. The ceria stabilization is due to lattice expansion because of the larger size of the Ce^{4+} cation in comparison with Zr^{4+}. Stabilizer oxide must be used in large quantities (~12 mol% CeO_2); as the symmetry is not reduced by the stabilizer cations, Ce-TZP is very transformable [19]. The stabilization of the tetragonal phase act by introducing oxygen vacancies or by the expansion of the cations lattice obtaining the decrease of 'oxygen overcrowding' around Zr cations. With tetravalent cations, the oxygen vacancies in the zirconia lattice are rare and are not able to stabilize the tetragonal phase. It was demonstrated that the addition of oversized cations dilates the cation network and thus decreases the oxygen overcrowding around Zr cations [4].

Chacun et al.[20] studied the LTD entity of 3Y-TZP materials when exposed to steam (140 °C for 7 days at atmospheric pressure) and revealed a 30% reduction of hardness, biaxial flexural strength, and Young's modulus. When 12Ce-TZP was exposed to the same aging treatment the mechanical properties decrease by only 2%. Ce-TZP shows also excellent defect resistance and ductility before failure due to a larger stress-induced transformation ability compared to 3Y-TZP. On the other hand, Ce-TZP, as respect to Y-TZP, shows a lower strength (~600 MPa and ~1000 Mpa, respectively) and a lack of translucency, an important aspect for dental prothesis. Both aspects are related to the challenge to produce Ce-TZP with grain

size as small as that of 3Y-TZP. Dense Ce-TZP shows a grain dimension of 1.5–2 µm while 3Y-TZP lower than 0.5 µm [4]. The intrinsic characteristics of Ce-TZP make it an outstanding biocompatible material, that is widely used for dental implants, osseointegrations, and orthopaedical implants such as a valid substitute for titanium ones [20]. A lot of patients showed allergy to titanium alloys or metallic implants, furthermore, due to their color, they are also less aesthetic because they can be visible through the gums (figure 1.5), while zirconia dental implants are invisible and completely camouflaged with the natural color of the teeth.

Figure 1.5 Comparison between a titanium implant and a zirconia one

As said, some zirconia ceramics, like Y-TZP, are susceptible to humid air, water vapor, and other aqueous fluids over a temperature range of 65-500 °C, but in aqueous solutions, the effect is more catastrophic at lower temperatures and the degradation rate decreases with time. Poor ageing resistance leads to surface phase transformations, and, as a consequence, the mechanical properties weaken [21]. The degradation is caused by the *t/m* transformation that starts from the surface of the sample and progresses to the inner part associated with the consequent formation of micro- and macro-cracks [22].

The nucleation of the transformation leads to a sequence of happenings "neighbor to neighbor". The transformation of one-grain leads to the increase of its volume that, as a cascade, stresses up the neighbouring grains, microcracking the material by opening a path for the penetration of water into the inner of the specimen. The entity of the grain growth depends on the microstructure features such as porosity, residual stresses, grain size, etc. (figure 1.6) [21].
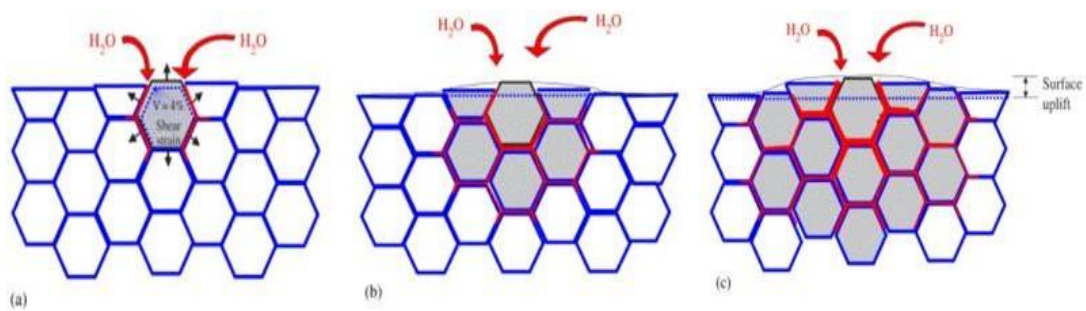
Figure 1.6 Ageing process representation that occurs in a cross-section. (a) Nucleation on a superficial grain leads to microcracking and stresses the neighbouring grains. (b) Growth of the transformed zone leads to extensive microcracking and surface roughening. In grey the transformed grains, and the red areas around the transformed grains represent the water penetration due to microcracking

Sato et al. [23] demonstrated that by increasing the CeO_2 content and by reducing the grain sizes, the transformation rate of aged Ce-TZP decreased. Ce-TZPs with a quantity of $CeO_2 < 10$ mol% and exposed to water vapor exhibited an increase in the superficial monoclinic volume fraction, but by increasing the ceria amount to 12 mol% the resistance to the aging increases considerably [22] [24].

The amount of t/m stress-induced conversion that occurred during fracture is depicted in figure 1.7 (A). With the decrease of ceria concentration, the monoclinc

11

phase, generated during the stress-induced transformation, increases. The monoclinic phase content increases also with a rise in the grain size.

This implies that under any applied stress, the monoclinic phase is produced in the larger tetragonal grains containing a small amount of ceria. In figure 1.7 (B) the bending strengths of Ce-TZP containing different amounts of ceria oxide are depicted. The results show that the bending strength of Ce-TZP was higher when the ceria amount was 10 to 12 mol % with grains smaller than 1 micrometer. For lower CeO_2 concentrations the material is unstable, the strength is limited by the low critical stress which induces transformation. For higher ceria amount, the transformation is inhibited, and the strength is limited by the critical size of the flaw. With a decrease in CeO_2 concentration and whatever the grain size, the fracture toughness rises, as depicted in figure 1.7 (C).
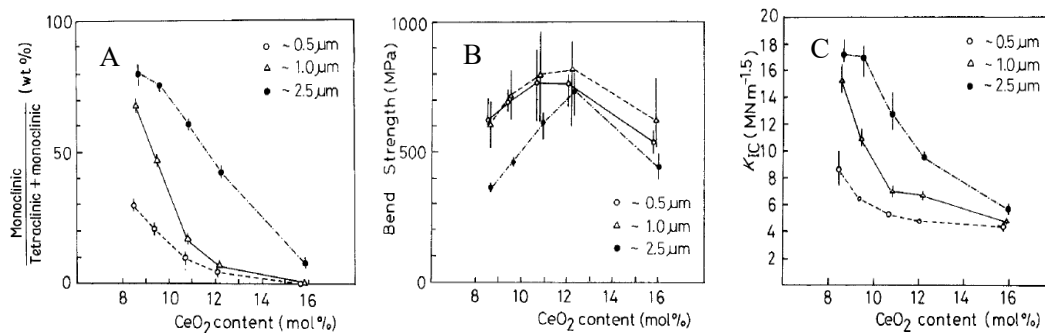
Figure 1.7 (A) Monoclinic fraction on fractured surface; (B) bending
strength; (C) Ce-TZP ceramics fracture toughness according to the ceria
amount and the grain size [25]

Due to the high transformability, prior to failure, Ce-TZP ceramics show a significant non-linear, permanent deformation. Ce-TZP shows a pronounced pseudoplastic behavior among ceramic materials and can bend before fracturing. The LTD resistance of Ce-TZP can be better understood from the metastable phase

diagram in figure 1.8 (A). It can be observed in the zirconia - ceria phase diagram that the material is fully tetragonal at the sintering temperature (1400-1550 °C); however, as it cools down, it becomes metastable with the generation of monoclinic crystals at a T_0 (*t/m*) temperature of ~ 400 °C [9,26]. The region of (meta) stability of the tetragonal phase, highlighted by the T_0 (*t/m*) line, is wider with respect to the yttria-zirconia phase diagram (B). T_0 (*t/m*) indicates the equilibrium temperature between tetragonal and monoclinic phases in a compositionally homogeneous sample [27].

(A)   **(B)**
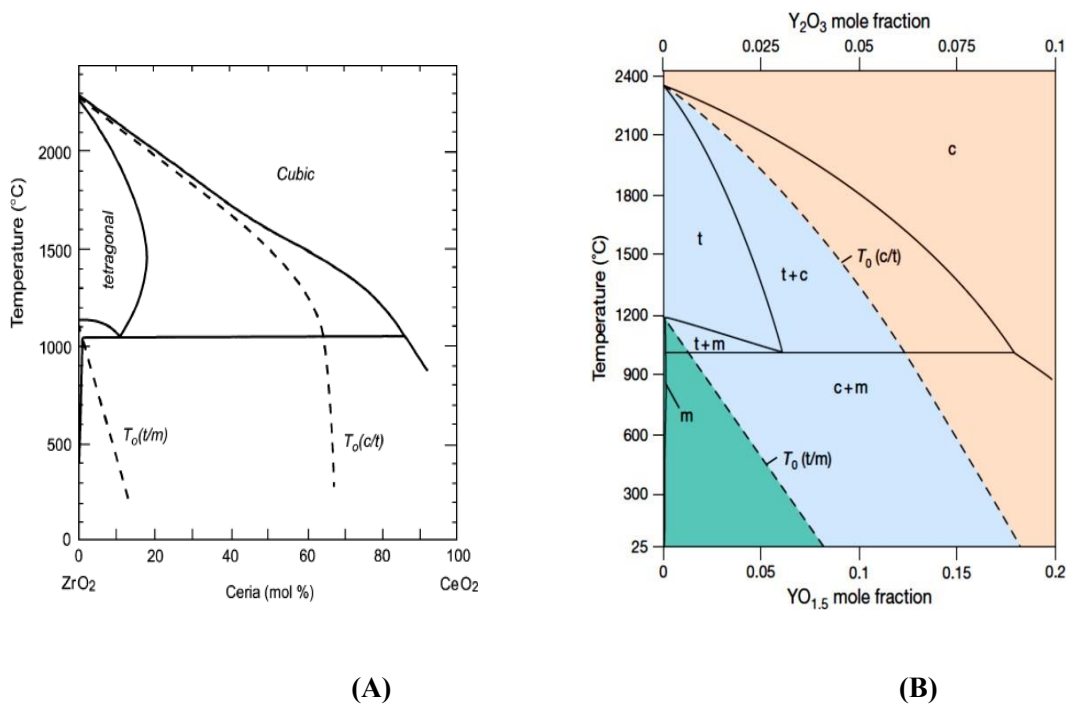
Figure 1.8 Zirconia-ceria phase diagram (A) and Zirconia-yttria phase diagram (B)

According to the diagram, a typical Ce-TZP composition capable of *t/m* transformation contains 8 mol% of CeO_2; above 12 mol% the system is not transformable. The mostly used compositions, most of all in the biomedical field, contain ceria in the range 10 mol% (referred as 10Ce-TZP) and 12 mol% (referred as 12Ce-TZP).

Chevalier et al. [9] studied the *t/m* transformation kinetics of Ce-TZP under aging conditions (134 °C, 2 bars). The aging resistance of 10-Ce-TZP is far higher than the corresponding YSZ composites, and the kinetic of the degradation is very slow. From the simulated in vivo test (it is clear that the lifetimes of Ce-TZP prosthesis far exceed the life expectancy of a human being (figure 1.9).
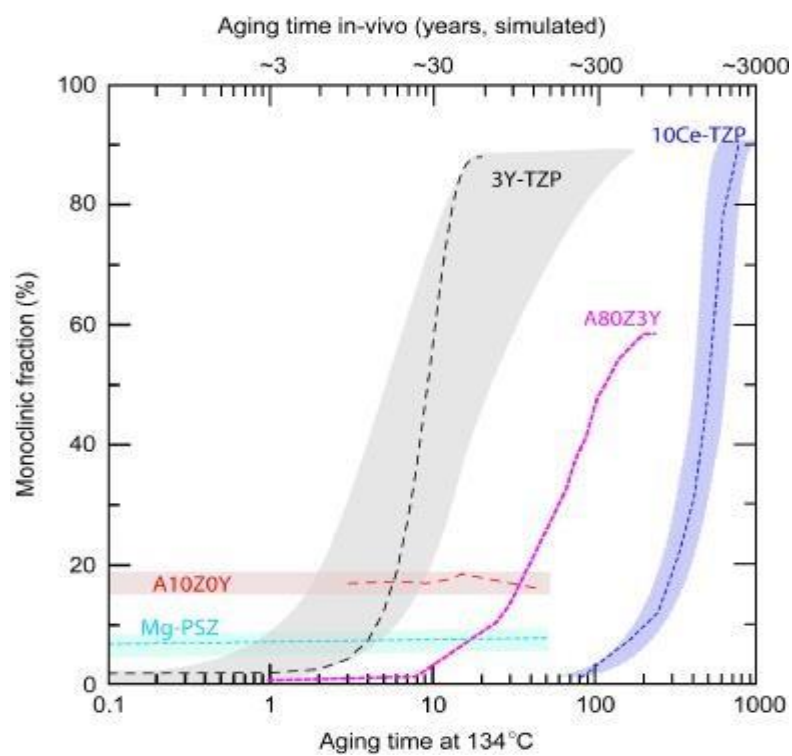
Figure 1.9 Low-temperature degradation kinetics of 10 mol% of Ce-TZP compared to 3Y-TZP, alumina-toughened zirconia (A80Z3Y), and zirconia-toughened alumina (A10Z0Y) measured at 134 °C and expected at 37 °C

1.1.2 Ce-TZP–alumina composites

As discussed in deep in the previous chapter ceria-stabilized zirconia (Ce-TZP) shows high aging resistance and toughness despite a medium strength (~500 MPa) caused by the grain growth during sintering and because of transformation-limited strength. Thus, developing zirconia-based ceramics with both high strength and high toughness is challenging. In this regard two categories of materials exist; the high-strength one for which the failure is governed by the pre-existing flaws, and the high-toughness one with a strength limited by the tetragonal to monoclinic transformation [28]. In order to enhance the strength through microstructure refinement, Ce-TZP composites with the addition of different ceramic oxides were developed, an example of this is the composite Ce-TZP/alumina [29–31]. An alternative consists of developing "in situ" platelets reinforced composites with Ce-TZP zirconia reinforced with alumina and strontium or lanthanum aluminates that represent an interesting combination of strength and fracture toughness.

Sato et al. [32], in 1989, demonstrated that the hardness and the Young's modulus of the alumina/Ce-TZP composites were higher with respect to pure Ce-TZP ceramics. In 1997 Nawa et al. produced an intra-granular microstructure with Al_2O_3 particles of 10-100 nm embedded into the grains of zirconia.

In Nawa's study, the bending strength, hardness, and elastic modulus increase as the content of alumina increases. On the other side, as the alumina content increases, a decrease in the fracture toughness was observed also, this behavior is coherent with the reduction of transformability [26] (figure 1.10).
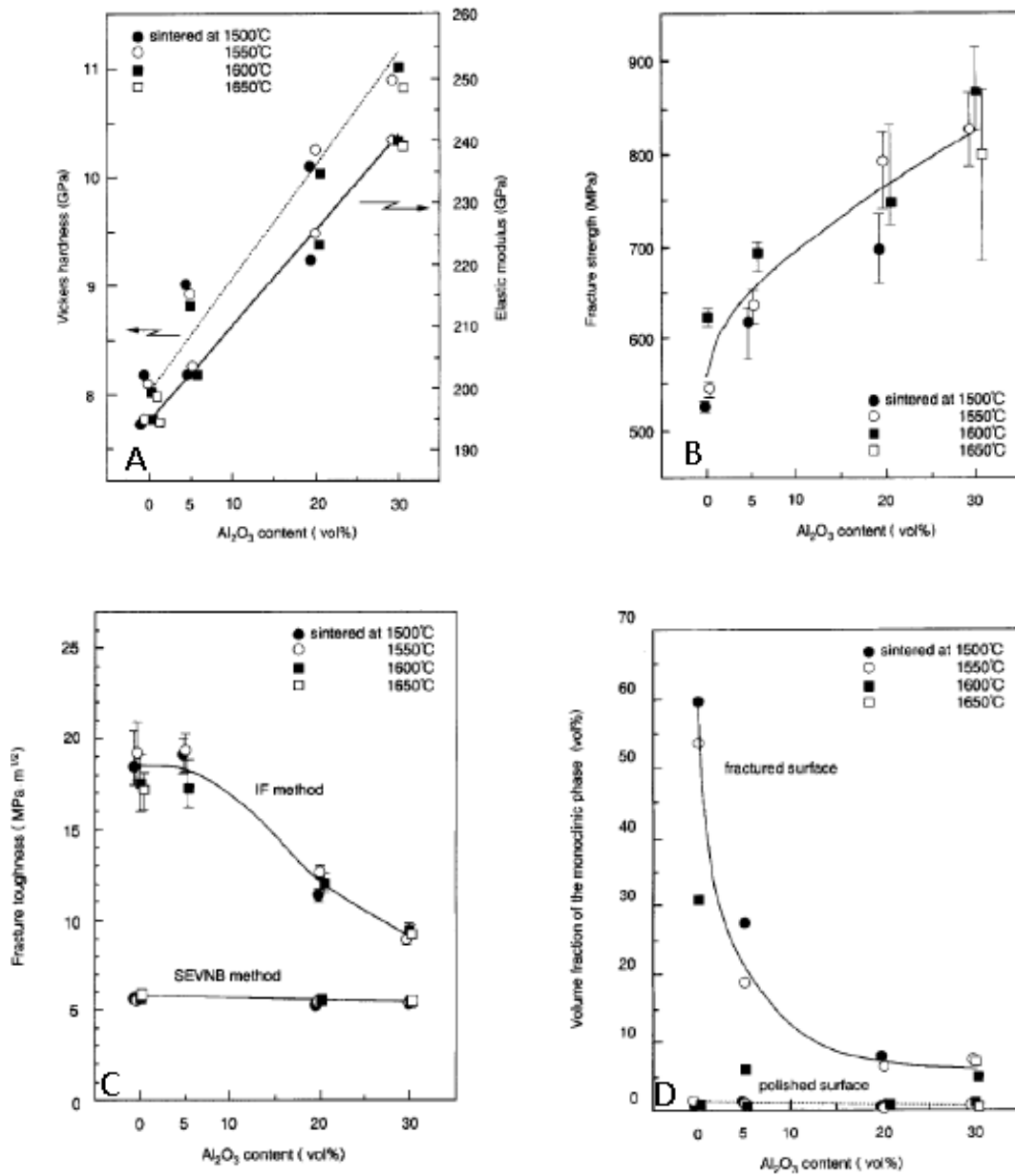
Figure 1.10 12Ce-TZP/Al$_2$O$_3$ behavior as a function of the alumina amount in the composite' formulation. A: Vickers hardness, B: fracture strength, C: fracture toughness, D: monoclinic volume fraction on the fractured surface, and the polished one [33]

Cutler et al. [34] were the first to investigate Ce-TZP strengthened by in situ formed strontium hexaaluminate ($SrAl_{12}O_{19}$, referred often as SA6). They developed three-phases zirconia-based composites having a composition of 12Ce-TZP/Al_2O_3/$SrAl_{12}O_{19}$ where the alumina was added in the range 15-30 vol% while by the addition of 0.5-8 wt% of $SrZrO_3$ the aluminate phase was obtained, in accordance with the reaction:

$$SrZrO_3 + 6Al_2O_3 \rightarrow SrAl_{12}O_{19} + ZrO_2 \qquad (1.2)$$
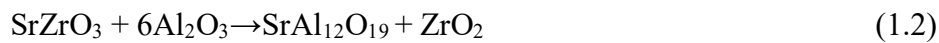
A zirconia matrix having Ce-TZP grain size of 1-3 μm, equiaxed Al_2O_3 grains of 0.1-1 μm and $SrAl_{12}O_{19}$ platelets with a length of 1-3 μm was obtained.

According to the composition, bending strength in the 500-700 MPa range, fracture toughness of 10-15 MPa√m and hardness of 10-14 GPa were achieved. Particularly, the toughness decreased with the alumina content while strength and hardness showed the showed the opposite trend [26].

1.1.3 The martensitic transformation

The model of martensite transition created by Bain in 1924 was related to the change that takes place during the quenching of steel: austenite, which is generated at a high temperature, converts to martensite by fast cooling in order to prevent species diffusion [35]. Numerous metal alloys, as well as minerals and ceramics like zirconia, undergo martensitic transformations [36].

This transition exhibits both favorable (toughening) and unfavorable effects (low temperature degradation, microcracking) [37]. When cooling pure zirconia, the tetragonal ($P4_2/nmc$) to monoclinic ($P2_1/c$) transformation takes place at around

1223 K (M_s) and is followed by a shear strain of about 0.16 and a volume expansion of about 0.04. When heated, the transition happens at around 1423 K (As) and is reversible. A completely tetragonal phase microstructure, with a Ms temperature such that spontaneous transition does not take place upon cooling to room temperature, may be achieved by alloying oxides such as Y_2O_3 or CeO_2. The transformation can then be triggered by exposure to water, by low temperature treatments (typically 350-500 K) in steam autoclaves [37]. The phase change that takes place at the point when a crack starts to spread causes in the material the increase of fracture toughness (Figure 1.2). For an effective transformation, a metastable phase must be present in the material and the transformation of this phase to a more stable state must be stress-induced in the field of the crack-tip. The transformation must occur instantly, without the need for time-dependent processes like long-range diffusion, and it must be followed by a modification in shape or volume. Similar to a crack shielding technique, the toughening process causes local compressive stress that prevent new cracks from forming. The converted product must not be more brittle than the parent phase from which it originates in order to guarantee that there is a net improvement in the material's toughness. As the crack grows, a 'wake' of transformed material is left behind and the strains remaining in this wake of transformed material lead to an increase in toughness (Figure 1.2).

Internal stresses will unavoidably be produced by the stress-induced martensite when embedded in a stiff matrix, changing the local stress field. If transformation crystallography permits it, a further transformation takes place close to the original martensite plate in response to this local stress field. A martensitic transformation is an athermal, diffusionless modification in the crystal structure that require the simultaneous shift of atoms over lengths less than an atomic diameter. This transformation leads to a macroscopic shape change of the transformed region [38] (Figure 1.4).

The toughness of a traditionally brittle ceramic could be increased by a factor of 4 or more [38]. The first thermodynamic model for zirconia tetragonal to monoclinic transformation was discussed by Lange et. al [39] considering an idealized configuration of a tetragonal particle embedded in an infinite matrix. The change of total free energy during the *t-m* transformation(ΔG_{t-m}) can be expressed by:

$$\Delta G_{t-m} = \Delta G_c + \Delta U_{se} + \Delta U_s \tag{1.3}$$

Where ΔG_c (<0 at low temperature) in chemical free energy is the difference between the *t* and *m* phase. This term depends on temperature, composition, and oxygen vacancy content.

ΔU_{se} (>0) is the change in elastic strain energy associated to the transformed particles. This is related to the size and shape of the particles and the matrix elastic modulus. A stiff matrix like alumina increases ΔU_{se}, stabilizing the tetragonal phase. Also tensile stresses influence ΔU_{se}, destabilizing the tetragonal phase. ΔU_s (>0) is the variation of energy related to the formation of new interfaces when the $t \rightarrow m$ transformation occurs.

If $\Delta G_{t-m} > 0$ the particle remains in the tetragonal state, if the value turns negative the tetragonal particle becomes unstable/metastable and might convert into its monoclinic state [14].

As a result of the martensitic transformation t-m, the total Gibbs free energy changes in the following way:

$$\Delta G_{t-m} = V(-\Delta G_{ch} + \Delta G_{str}) + S\Delta G_{sur} \tag{1.4}$$

where *ch* refer to the chemical free energy, *str* to the strain energy including both shear and dilatational energy, and *sur* the surface energy including the surface free energy, twinning energy and micro-cracking energy. V is the volume and S, area of transformation. The equilibrium temperature between the t-m transformation, T_0, is

the temperature at which ΔG_{ch}=0, and the M_s is defined as the temperature at which $\Delta G_{t\text{-}m}$=0[6].

ΔU_{se} is directly related to the surrounding matrix modulus, this value increases with a stiff matrix such as alumina and decreases in presence of internal stresses.

From the crystallographic point of view, a correspondence between the parent (tetragonal) and the product (monoclinic) phase exists in the $t \rightarrow m$ transformation (Figure 1.11).
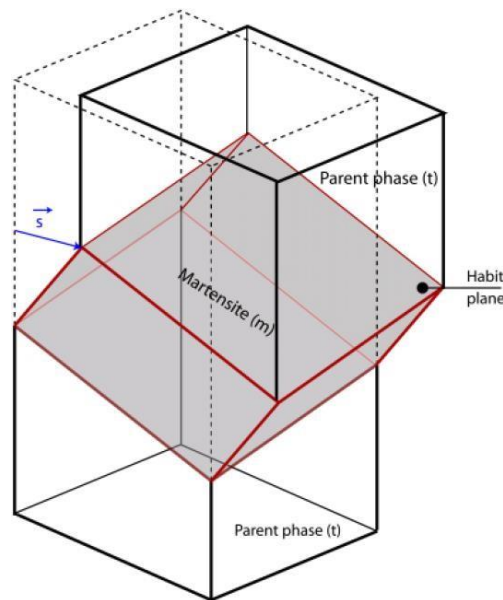
Figure 1.11 Schematic representation of the martensitic tetragonal to monoclinic transformation, the crystallographic correspondences between the tetragonal (parent) and monoclinic (product) phases are shown [9].

If a break releases the mechanical restraint in the metastable tetragonal phase and enables it to transition to the monoclinic phase, the energy required to propagate the crack through a dense zirconia-containing metastable zirconia rises. This can only occur below the temperature T_0 (t/m), that is the martensite start temperature (TMS).

To calculate the stress-shielding arising from the transformation-induced strains near the crack tip, the linear elastic fracture mechanics [28] is employed. The applied stress intensity factor K_I is shielded by the stress-induced transformation, and as a result, the true stress intensity factor at the crack tip K_{Itip} is lower than that applied by the external forces, in agreement with

$$K_{Itip} = K_I - K_{ish} \tag{1.5}$$

The higher the applied stress intensity factor, the larger the conversion area and the shielding effect, resulting in the expression

$$K_{Ish} = C_{sh}K_I \qquad . \tag{1.6}$$

with

$$C_{sh} = \frac{0.214 \, EV_f \, e^T(1-v)}{(1-v) \, \sigma_m^c} \left(\frac{\sqrt{3}}{12\pi} \right) \tag{1.7}$$

Where E is the Young's modulus, V_f the volume fraction of transformable particles, e^T is the volume dilatation associated to the transformation, v the Poisson ratio, and σ_m^c is the critical local stress leading to phase transformation. The toughening of zirconia depends on the critical local stress leading to phase transformation, σ_m^c that depends in turn on the magnitude of the undercooling below the T_0 (t/m) temperature: the larger is the T_0 (t/m) value, the lower is the critical stress for stress phase transformation and the larger is the transformation toughening [14].

1.2 Additive manufacturing of zirconia ceramics

Recently, additive manufacturing (AM) has successfully established itself as an efficient technology to produce ceramics with high dimensional accuracy with a sensitive reduction of costs and production times [40].

As discussed above, zirconia is a ceramic oxide that possesses outstanding mechanical properties: compression strength of about 2000 MPa, a flexural strength of 900–1200 MPa [3] and fracture toughness of 5–10 MPa m$^{1/2}$ [41]. ZrO_2 shows also good ionic conductivity, thermal and chemical stability, and resistance to aggressive environments [3,42]. It is extensively utilized in the biomedical field due to its well-known biocompatibility. Thanks to its aesthetic characteristics zirconia has been widely used in dentistry to produce implants, crowns, bridges, and veneers [17]. Zirconia has also been used for other applications, including solid oxide fuel cells [43], thermal barriers, optical coatings, catalysis or catalytic supports, and sensors [44].

To produce zirconia ceramics several plastic forming methodologies have been employed such as injection molding, slip casting, tape casting, and gel casting.

Another forming technologies adopted is the dry pressing. Even if, compared to pressing methods, plastic forming methodologies allow more complex parts to be obtained, some limitations exist such as low machining precision, and difficulty to produce complicated forms are typical drawbacks of these traditional technique that can be avoided with the 3D printing techniques [45].

Although many researches concentrate on 3D printing of alumina [46–59] or zirconia [60–68], few researches have been conducted on Al2O3-ZrO_2 [69–73] composites. In addition, few papers deal with Ce-ZrO_2-based composites fabricated by SLA or DLP [74,75]. The above results clearly show that there is a gap in the scientific literature on ZrO_2-Al_2O_3 composites produced by AM techniques.

The ISO/ASTM 17296 standard on Additive Manufacturing Technologies defines AM as the "process of joining materials to make objects from three-dimensional

3D) model data, usually layer by layer, as opposed to subtractive manufacturing and formative manufacturing methodologies" [76].

The ISO/ASTM standard divides additive manufacturing (AM) processes into two categories: direct processes, in which components are produced in a single operation, and indirect processes, in which parts are manufactured in two or more steps. With the indirect methods to manufacture green bodies, an organic binder must be used. Postprocessing treatments like debinding and sintering are also fundamental to obtain dense parts [77]. Additive manufacturing techniques can be used to fabricate different materials such as polymers, metals, or, ceramics [63,70,78–81]. Ceramic additive manufacturing (C-AM) uses a four-stage process: model creation and slicing, printing, post- treatment, and heat treatment that permit to overcome some of the intrinsic constraints of ceramics, such as their formability and processability.

The production of ceramics and ceramic matrix composites through additive manufacturing techniques is in an early stage if compared with the AM of polymers and metals [78]. According to the raw materials C-AM can be classified into three different subgroups: solid-based, powder-based, and slurry-based methods [82–84].

To manufacture zirconia ceramics the most important AM techniques adopted include selective laser sintering (SLS), selective laser melting (SLM), vat-photopolymerization techniques (which include stereolithography (SLA) and Digital Light Processing (DLP)), ink-jet printing (IJP), fused deposition modeling (FDM) [40]. Among the AM technologies, stereolithography (SLA) and DLP are one of the slurry-based techniques that provide the best resolution, precision, and surface finishing of the printed parts.

1.2.1 Stereolithography (SLA)

The term "stereolithography" is composed by the word "*stereo*", which describes a 3D process, and "*lithography*", which is the print of recessed or elevated structures on a plane surface. In SLA, a photosensitive resin loaded with ceramic powder is photopolymerized with a layer-by-layer process using lasers, LED or liquid crystal display (LCD) [46] to build up a solid structure. High design freedom is allowed by this technology.

A CAD model of the object to print is first created and then, converted to compatible files by creating a Standard Tessellation Language (STL) data.

The printing of ceramics with SLA involves three steps: first, a layer of the suspension is spread on the platform and exposed to UV light for curing. A second layer is then spread on the top surface of the previously cured layer and irradiated too. Then, when all the parts are printed, a thermal treatment is necessary to burn out the organic matter and densify the ceramic skeleton.

Through exposure to specific wavelengths, selected areas of the photocurable monomer resin are solidified. Single layers are stacked one onto one other until the final structures are created. To guarantee that uncured monomers are polymerized, the printed parts can be post-cured using heat treatment or exposure to UV light [85].

1.2.2 Digital light processing

In stereolithography, photo-sensitive materials are exposed to UV-light to obtain polymerized components [86]. The significant difference between Digital Light Processing (DLP) and stereolithography resides in that DLP induces an instantaneous entire layer polymerization using digital micro-mirrors devices (DMD). In contrast, in SLA, a single point is exposed at a time (Figure 1.12). As a result, DLP offers a higher printing speed, a lower cost, and a higher resolution [87]

than SLA and other technology competitors at the expense of lower local energy density[88].

The key component of the DMD is an array of mirrors, each one representing a single pixel. Individual tilting of each mirror enables fast switching of pixels. The fast-switching speed of the DMD is fundamental for realizing grayscale illumination and controlling the exposure time and the energy dosage. This pixel-based mechanism makes DLP excellent for illumination of sharp corners but can cause saw-tooth type surface roughness on curved surfaces. Because of that when a higher resolution is necessary, the pixel size must be reduced with appropriate optics. Since DMD has a fixed number of mirrors, this leads to shrinkage of the image and reduces maximum geometry size. Large parts are thus often printed at lower resolutions than small ones.
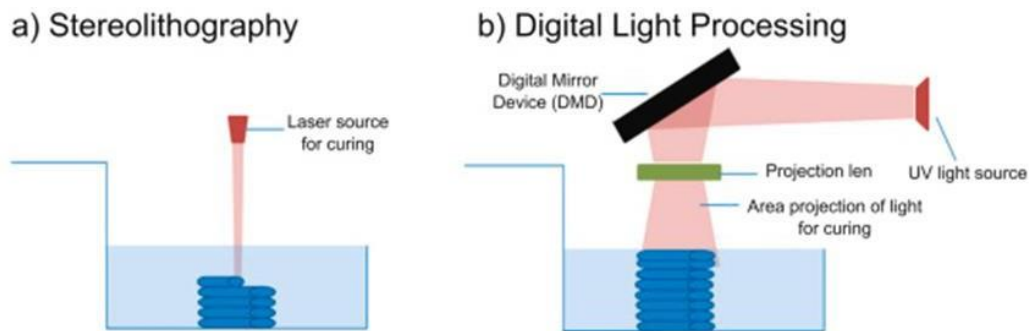

Figure 1.12 Comparison between (A) Stereolithography and (B) Digital Light Processing[89]

1.2.3 Challenges in SLA and DLP

The DLP process is well-known for its sub-micron precision even if ceramic particles with high refractive index can hinder the curing depending on to the thickness of the layer and the concentration of the slurry. To remove the polymer,

the components are thermally treated, and then sintered to densify the ceramic skeleton. In SLA and DLP, each layer photopolymerizes and stacks one after the other. During the photopolymerization process, the UV light interacts with the medium, where absorption and scattering interactions happen [90]. The monomer and the ceramic particles absorb part of the UV-light, while the other part is scattered in random directions. This interaction attenuates the light, which reduces the effectiveness of the cure depth [91,92]. The cure depth is a key component of the printing process since it influences the interlayer adhesion and the layer thickness, together with rheological characteristics of the resin [66,93]. Inadequate curing depth cause delamination and constrains the layer thickness. The cure depth and interlayer adhesion could be improved by rising the energy dose, the challenge is maintaining a high dimensional lateral resolution and avoid an excess of the lateral dimensions by the adoption of the suitable printing and curing strategies [92].

Delamination between layers may also be caused by slurries with inadequate rheological characteristics. In the conventional manufacture of ceramics, shrinkage and dimensional changes during the sintering step are well known. Dehurtevent et al.[94] demonstrated that changing the solid loading and particle dimension, affect the directional shrinkage. Cracks might occur either during the printing or after the printing strep. These can be mitigated by setting a cure depth larger than the layer thickness, enabling a strong interlayer adhesion. Light attenuation affects the lateral resolution and can cause delamination. A strong light scattering can be caused by the difference of the refractive index between solid (ceramic particles) and liquid fraction (monomer) of the photocurable slurry [95].

Cracks and microstructural defects also occur during the thermal debinding step because of the pressure build-up of the volatile compounds [55]. A rapid thermal debinding program decomposes the organics in a too-short period causing the release of spatial expansion stress that will be higher than the binding force between ceramic particles; then, a catastrophic series of events will be initiated, such as the formation of surface cracks [96].

1.3 Suitable photocurable ceramic resin

In SLA, the characteristics of the ceramic suspension are determined by two aspects, rheology and light absorption [74].

Homogenous slurries with a high solid loading and low viscosity are necessary to produce components with no defect and high performances.

For the SLA of ceramics, the solid loading must be higher than 40 vol% to prevent any defect after debinding and sintering [90,97].

The extent of shrinkage depends on the solid loading of the slurries. The shrinkage is inversely correlated with the solid loading which must be as high as possible. However, the viscosity increases with the solid load content, which is undesirable for obtaining a highly homogeneous microstructure. When the solid loading exceeds 31 vol %, the viscosity starts to increase exponentially [90]. A high solid loading may lead to a difficult debinding too, because of an impeded diffusion of gases [98]. The solid content affects the rheology, from a conventional Newtonian behavior seen for pure resins to a shear-thinning behavior for concentrated slurries. Furthermore, high viscosity makes the suspension more stable by decreasing the sedimentation effect during the photopolymerization, but, at the same time, it reduces the flowability [80,99,100]. Chen et al.[101] fabricated ZrO_2 by SLA from a 42 vol% suspension with a viscosity of 3.01 Pa·s at the shear rate of 30 s^{-1}. Komissarenko [61] produced a ZrO_2 photosensitive resin with a solid loading of 33 vol% and low viscosity of 1.6 Pa·s at 30 s^{-1}. Wang et al. [102] developed zirconia ceramic with a shrinkage of 11.1% using a slurry with a solid loading of 14 vol%.

Li et al. [103], optimized the dispersant (Disperbyk-103) amount in zirconia suspensions. They obtained a 42 vol% of solid load by the addition of 3.5 wt% of dispersant. A low viscosity (<5 Pa·s at 30 s^{-1} shear rate) with a shear-thinning behavior was obtained.

Zhang et al.[64] manufactured high solid loading (55 vol%) ZrO_2 slurries with a low viscosity (1.65 Pa s at the shear rate of 200 s^{-1}) thanks to the addition of 2 wt% of the dispersant KOS110.

The slurry often requires the addition of a dispersant to maintain resin stability, and to increase the repulsion forces between particles to prevent agglomerations [104]. The long chain structure of the dispersant adheres on the surface of the ceramic particles, causing electrostatic and/or steric repulsion. In this way, the agglomeration of the particles is avoided, the viscosity is lowered, and appropriate rheological behavior is ensured [105].

The suspension should have an appropriate viscosity, so that a fresh liquid layer can be deposited after printing each layer.

Thus, a printable slurry must show a shear thinning behaviour with the viscosity that decreases with the increasing shear rate [106]. For systems with recoating devices, the optimal viscosity for printing is typically less than 20 Pa · s at a shear rate of 100 s^{-}

^{1} and 3 Pa·s at a shear rate of 30 s^{-1} [107], at 25 °C. When the concentration of dispersant is low it is in an unsaturated adsorption state, insufficient to overcome the attractive forces between the particles. Due to the Brownian motion, the particles that had not adsorbed the dispersant will tend to aggregate with each other and the slurry will be unstable and very viscous [107].

When the amount of dispersant reaches saturation, the unadsorbed dispersant molecules will be in the inter-particle framework, causing flocculation, instability, and an increase of the viscosity [48]. In this case, the slurry exhibits a shear thickening behaviour, and the flow of the slurry is hindered (as shown in figure 1.13) [108].

With an optimal amount of dispersant, a "protective" adsorbed layer will form on the particles' surface. This layer causes the repulsion between the particles and the

attractive forces are suppressed. As a result, low viscosity and high dispersibility of the ceramic suspension may be obtained thanks to the reduced degree of particle agglomeration and flocculation [106]. According to Kim at al. [106] the surface roughness of printed parts is also influenced by the dispersant concentration; the surface becomes smoother as the dispersant concentrations increase.
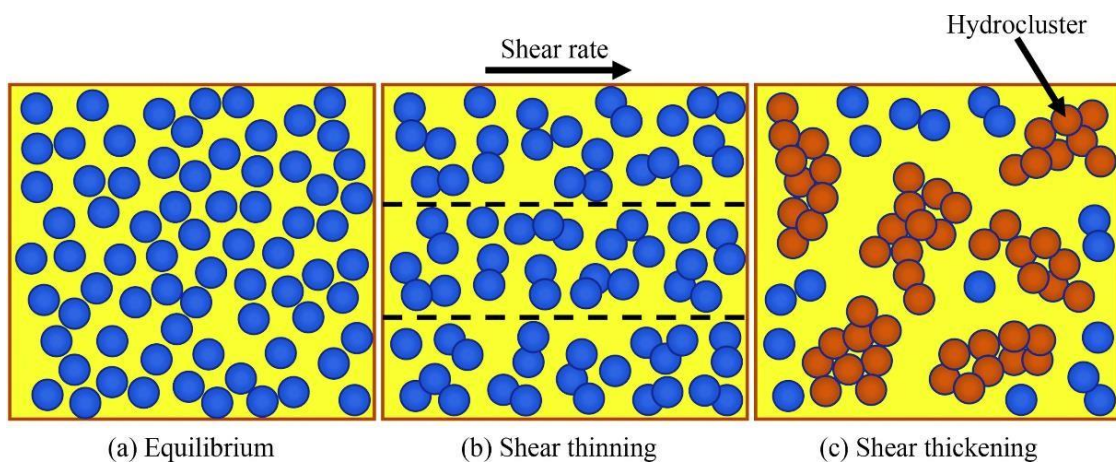
Figure 1.13 The mechanism of shear thickening [10]

Li et al [109] investigated the behavior of 12 dispersants in zirconia suspensions. They identified DISPERBYK-103 as the best candidate, and successfully prepared high solid loading (42 vol%) slurries with the addition of 3.5 wt% of dispersant.

Generally, there are two categories of photocurable ceramic resins: aqueous (acrylamide-based) and non-aqueous (acrylate- and epoxy-based) resins. [110]. The aqueous resin, from one side is free from volatile organic compounds, and, on the other side, shows disadvantage related to the low strength of the green body.

In contrast, non-aqueous ceramic resins provide higher strength for the cured body. Another crucial factor is the homogeneity of the dispersion. Ceramic suspensions should exhibit good stability of dispersion in order to manufacture structures with sufficient homogeneity and high density [106]. A homogeneous dispersion of ceramic powders in the photocurable slurry is beneficial for enhancing the curing

performance of the suspension, as well as the shaping and preparation of the green body. Ultrasonic dispersion or ball-milling are often used to improve the homogeneity of the ceramic suspensions. Furthermore, it is demonstrated that the mutual attraction between the ZrO_2 particles increases as the solid loading increases [111]. Cai et al. [108] studied the effects of slurry mixing methods and solid loading on the rheological properties and demonstrated that the viscosity reached by the multi-step mixing method was lower than that by the one-step mixing method. Electrosteric dispersants contain a mix of poly(meth)acrylic acid and ammonium ions. The ions interact with the organic media and generate an absorbing band at 365 nm.

Cailliet et al. [74] tested four dispersants: Disperbyk 111 and Rhodafac-RS-610-E that exhibit a steric repulsion effect. Synthron B03 and Darvan C–N with an electrosteric effect, a combination of electrostatic and steric dispersions. In Caillet's study, the amount of dispersant added to a 45 vol% Ce-TZP powder, ranged from 1 to 3.5 wt% and the optimum amount was found in the 1.5 wt% of Rhodafac-RS-610-E. Additives and dispersants can absorb a certain amount of light, thus reducing the photon flux available for the photochemical reaction. Generally, steric dispersants exhibit a low absorption of UV light. The resolution is affected by the absorbance of the photoinitiator at the actinic wavelength, also called near ultraviolet (UV), a critical aspect for the light penetration in-depth of each layer. Another important aspect is the photopolymerization reaction attenuated by the UV light scattering. ZrO_2 has a large refractive index, which could result in more UV light absorbed or scattered by the ceramic matrix material, leading to reduced curing depth. Therefore, the presence of Al_2O_3, as second phase with a lower refractive index, into ZrO_2 could alleviate this phenomenon [112].

1.3.1 Light - polymer interaction

In stereolithography, through UV-light exposure, a chain reaction starts by reactive species (free radicals or ions) and transforms a multifunctional prepolymer into a cross-linked polymer. Since most prepolymers do not generate initiating species after UV exposure, the introduction of organic molecules with low molecular weight (initiators) to start the polymerization, through photophysical and photochemical reaction, is necessary. The light-polymer interaction is a photophysical process, which does not involve chemical changes, but only sets electrons into motion. When a chromophore (a functional group with electrons from π and η orbitals) absorbs light, the photon reacts with an atom or group of atoms and induces transitions between the ground state and the excited states. In Franck - Condon theory, 10^{-5} s is the time necessary to absorb a photon and transit to an excited state.

When a molecule absorbs the light, the electrons are set into motion by the oscillating electric field, which is promoted from the highest occupied molecular orbital to an unoccupied molecular orbital with the formation of an excited singlet state molecule with a short life (less than 10^{-8} s), which disappears by dissipating the excited energy. The light absorption by a molecule and the evolution of the excited states can be better understood through the Jablonski energy diagram [113]

(Figure 1.14)

The absorption of energy E from the photon, given by hv where h is Planck"s constant (6.62 x 10^{-34} J.s) and v is the frequency of the radiation, which must be at least as high as the as the energy difference ΔE between the ground state and the excited one. During the transition, the interaction between the electric component of the radiation and the molecule happens with consequent variation in the molecule's dipole moment. Light absorption is given by $\varepsilon\beta L$, where ε is the extinction coefficient, β is the concentration of the absorption species

(photoinitiators), and L is the light-path length. During the photon-molecule interaction, a valence electron moves from the highest occupied molecular orbital to an unoccupied one, with the formation of an excited singlet state molecule with a short life (less than 10^{-8} s) that disappears dissipating the excited energy [114].
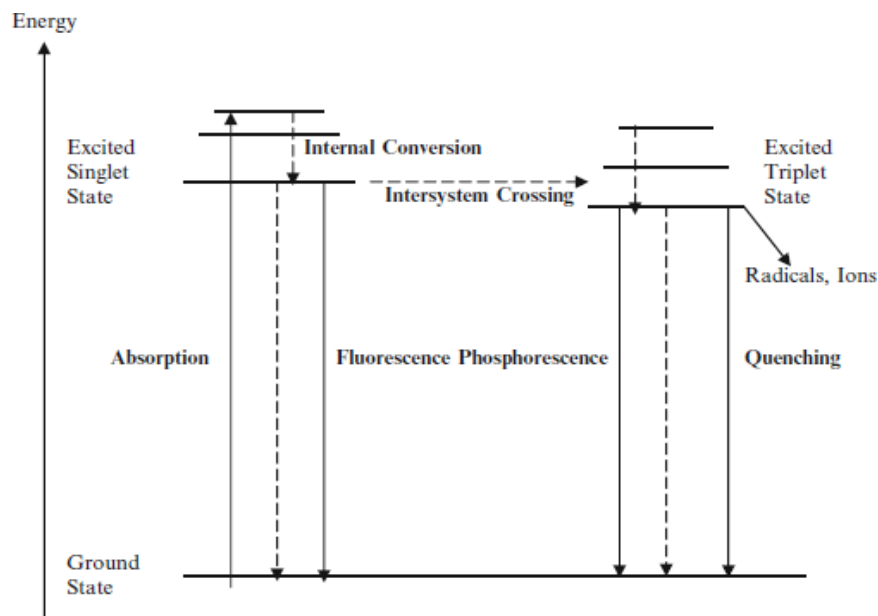
Figure 1.14 The Jablonski energy diagram [113]

Bagheri et al. [115] studied in deep the photopolymerization in 3D printing providing an overview of novel 3D printable photopolymers and challenges that limit the use of conventional photopolymers. They discussed as well recent progress of controlled living radical photopolymerization techniques in 3D printing, which will open the way to innovative 3D materials with living features and post-printing modifications.

3D photo-cross-linking strategy is based on the use of liquid monomers/oligomers curable through light source exposure at a specific wavelength. A photoinitiator is

necessary to convert photolytic energy into the reactive species (radical or cation) which can drive the chain growth via the radical or cationic mechanism. High molar extinction coefficient photoinitiators at short wavelengths (UV < 400 nm) are used to start the photochemical reaction. These systems show some shortcomings: UV photons have a low penetration depth (~100 μm), resulting in a time-consuming printing job. For bioprinting, UV light is risky for cellular photodamage such as genetic and chromosomal instability in cells. Prolonged high-energy UV exposure might lead to collateral reactions of degradation of reactant and/or products. Bagheri et al. found the near-infrared (NIR)-induced photopolymerization as a potential solution to all the previously described issues [115].

1.3.2 The curing mechanism

The curing reaction induced by a UV light supplies the energy to bond numerous small molecules, forming a highly cross-linked polymer.
The cured layer adheres to the previous ones and, through a layer-by-layer stacking process, the 3D structure is formed [106].
Radical polymerization allows photopolymerization, by generating reactive species (free radicals) by the interaction with the light and formation of an insoluble and cross-linked 3D network.
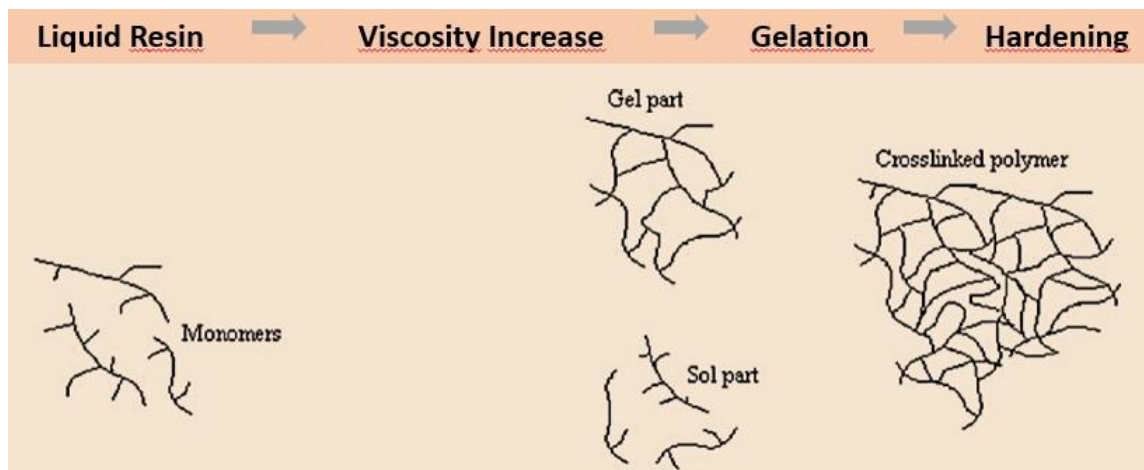
Figure 1.15 Illustration of the curing process [114]

During the curing reaction occur, the following processes occur:

- Gelation: transition from liquid to rubber

- Vitrification: transition from liquid or rubber to glass

During gelation, a molecular network is formed, and a *gel* and a *sol* phase coexist with consequently increasing of the viscosity. As the reaction further progresses, the amount of sol phase decreases, and the polymer becomes more cross-linked inhibiting molecular mobility.

During the vitrification, a thermo-reversible process occurs: a glassy solid material is formed due to an increase in the molecular weight of the cured polymer and the polymer cross-linking density. During the curing reaction, the glass transition temperature increases as a consequence of the increase in molecular weight and cross-linking density. The kinetics of the curing is deeply influenced by the UV-light intensity, the temperature, and the resin formulation [114].

The ceramic particles have a certain size distribution. According to the light scattering theory, both particles mean size and distribution affect the light scattering. The ceramic filler plays a key role within the suspension, interferes with

the penetration of radiation due to the mismatch between the refractive indexes of the monomer and the ceramic powder causing scattering [116].

Adake [118] investigated the spatial resolution upon cure depth and width of alumina suspensions printed by microstereolithography. They prepared two suspensions, the first by dispersing alumina in a monomer with a hydrophobic backbone structure (ends of the chain with $-CH_2-$), and the second with a hydrophilic backbone (ends of the chain with $-OH$). The curing behaviors of the two formulations were studied by monitoring the $C=C$ conversion.

The extent of gelation of the hydrophobic backbone resin causes excess broadening of cure width, reducing the spatial resolution of the printed parts.

1.3.3 The curing depth

In digital light processing technology, curing depth is an important parameter related to the UV energy the slurry is exposed to [101].

Cured thickness of a ceramic formulation versus the exposure time to UV irradiation is a parameter to assess the printability of a photocurable formulation. To measure the thickness of the cured layer, the photocurable formulation is spread on a substrate and a chessboard pattern is projected onto the surface. The cured layer is cleaned with paper and the thickness of the polymerized layer is measured with a digital micrometer.

Borlaf et al.[66] demonstrated that, even if the cure depth was deeper than the layer thickness, strong bonding between layers could not be assured. Insufficient exposure time could cause poor bonding between layers, and cracks could occur

during the debinding cycle, with a deleterious effect on the sample's properties. However, if the exposure time is too long, the slurry outside the printing region is partly cured due to the light scattering, resulting in poor precision of the green samples [119].

The curing depth is given by:

$$C_d \approx \frac{d}{Q} \frac{1}{\Phi} \, In \, \frac{E}{Ec} \qquad (1.8)$$

With

$$Q = \left(\frac{\Delta n}{n_0}\right)^2 \left(\frac{d}{\lambda}\right)^2 \qquad (1.9)$$

where, d is the mean particle size of the ceramic powder, Φ is the volume fraction of the powder in suspension, n_0 is the refractive index of the polymeric solution, Δ_n is the refractive index difference between the powder and the polymeric solution, and λ is the radiation wavelength.

Quantifying the effects of scattering is important to improve the reliability of the 3D printing process. The curing behavior depends on the absorption of the monomer solution and by the entity of the scattering of the ceramic particles.

The scattering theory has been developed to describe the interaction of light with particles in a liquid medium. The Mie theory describes the scattering of light of a round-shaped, isolated particle in an inert medium. For the ceramic photocurable suspension, the Mie theory cannot be used; due to the high solid loading, the particles cannot be considered isolated for photon scattering. Nearby ceramic particles cause cross-interactions and the scattering of a single particle is impossible to be analyzed separately [120]. According to the Mie theory, the liquid medium must be inert, however, the monomer solution is reactive.

By absorbing the photons, the monomer solution limits their propagation ability through the slurry affecting the predicted scattering length.

The UV penetration depth depends on the size of the ceramic particles, the distance between them (dispersion degree, solid load), and the refractive indexes (RI). The larger the difference in RI between the ceramic fraction and the resin, the smaller the penetration depth. The higher refractive index of ZrO_2 results in a smaller penetration depth with respect to Al_2O_3 leading to a smaller layer thickness and to the over-curing of the slurry due to the light scattering [121].

The refractive index (n) of α-Al_2O_3 has been reported to be 1.76 [122]. To the best of our knowledge, references of the RI of Ce-TZP could not be found. However, Shiraishi et al. [123] estimated it from the RI of pure ZrO_2 (n = 2.160) and pure CeO_2 (n = 2.2) and estimated a 10Ce-TZP's RI much closer to 2.160. This suggests that there is a large difference in refractive indexes between the Ce-TZP and the Al_2O_3 phases, provoking an important UV scattering at phase boundaries.

Moreover, small particle size tends to increase the scattering with detrimental effects on cure depth, this can be explained by the higher numbers of scattering centers [70].

Sun [124] discovered that the effects of the light scattering are strongest when the dimension of the ceramic powder is close to the laser wavelength and when there is an high contrast between the refractive index of the prepolymer and the particles. Li et al. [68] studied the light absorption of zirconia ceramics and found that absorbance decreases the curing depth and width.

Zhang [125] discussed the curing properties such as curing depth and width in the SLA process of 3Y–ZrO_2 dispersed in an acrylic-based resin. They obtained a penetration depth of the slurries of 17.2 ± 0.50 μm and a critical exposure of 4.80 ± 0.62 mJ/cm^2. the slurries of 17.2 ± 0.50 μm and a critical exposure of 4.80 ± 0.62 mJ/cm^2.

As depicted in figure 1.16, one of the critical phenomena in stereolithography is the propagation of the light through the matter [126]. When a photon travels through the ceramic suspension, it is scattered by ceramic particles, and its direction of propagation changes.

The incoming UV light is scattered by ceramic particles, which act as scattering centers [127]. The photons are absorbed either by the UV- curable solution or the ceramic particles. The photons absorbed by the UV-curable solution will initiate the polymerization reactions [124]. The light distribution in the slurry may influence the conversion rates of the monomer in the resin, which is a key parameter to define the degree of curing and the green parts' accuracy [126].

In a typical ceramic stereolithography process, the mean size of the particles is varied from 0.3 to 1 μm. A strong light scattering will occur when the particle size is close to the wavelength of UV light (0.364 μm) [124]. Scattering also reduces the depth of cure and the degree of secondary exposure between layers, resulting in the weakness of interlayer bonding [126].
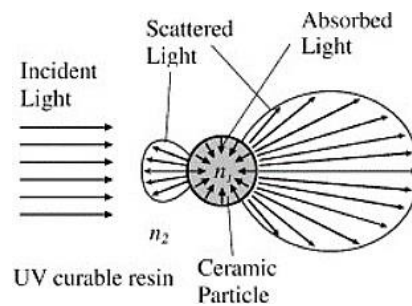

Figure 1.16 Schematic representation of absorption and light scattering in optically inhomogeneous media. n_1 is the refractive index of the ceramic particles, n_2 is the refractive index of the UV-curable resin.

1.4 The resin composition

Photocurable resins for SLA and DLP-stereolithography are constituted by the precursors which form a crosslinked network once polymerized and the photoinitiator which starts the reaction of polymerization. Inert dyes that absorb incident light and improve control over the polymerization might also be introduced. Diluents, surfactants, and stabilizers are examples of other additives that could be introduced in the resin (fig 1.17).
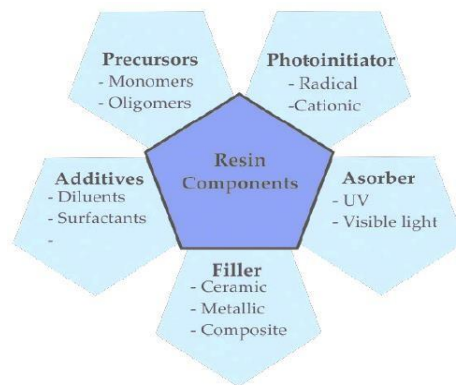
Figure 1.17 Resin composition in stereolithography [59]

1.4.1 Precursors

In stereolithography the precursors are liquid molecules that, after exposure to light, polymerize to form a 3D framework. Acrylate-based resins are commonly used in the SLA and DLP-stereolithography processes. These resins exhibit on one side high reactivities but on the other side, they show a shrinkage during printing, causing potential distortion of the printed part, and high sensitivity to oxygen, which inhibits the polymerization reaction.

Vinyl ethers are very reactive systems too that polymerize through a cationic mechanism. Epoxy systems, less reactive than acrylates and vinyl ethers, are also based on cationic photopolymerization, are inhibited by the humidity but are stable to the oxygen. Epoxy resins exhibit lower shrinkage compared to acrylate ones. Hybrid systems have been developed in order to benefit of both advantages of epoxy and acrylate systems in term of fast curing and low shrinkage rate [87].

Zheng et al. [128] prepared ZTA ceramics slurries with a solid loading of 50 vol% and viscosity less than 20000 mPa·s printable by DLP-stereolithography. UV-curable precursor mixtures were produced by diluting Ethylene Acrylate Copolymer (EA) with 1,6-Hexanediol diacrylate (HDDA), Di-TMPTA (weight ratio of 3:5:2), and Thermoplastic polyolefin (TPO). Good fluidity and curing properties were obtained.

1.4.2 Photoinitiators

The photoinitiator is the resin component that reacts to light, it is crucial since it governs the curing rate. The photoinitiator must be highly soluble in the prepolymer, have a high initiation efficiency, and storage stability. The photoproducts generated by the initiators shouldn't be toxic or cause polymer degradation over time and must be colorless.

There are two main categories of photoinitiators: *radical* and *cationic*. Some initiators (such as iodonium and sulfonium salts) have the capacity to start curing processes via both radical and cationic mechanisms. To enable a cure depth between 0.1 and 2.5 mm, photoinitiators are added in concentrations ranging from to 12 wt%.

The absorbance of the incident radiation by a *radical* photoinitiator leads to the formation of radicals. To avoid quenching (process which decreases the fluorescence intensity), the excited species must have a brief lifetime in presence of oxygen or the prepolymer. There are two major categories of radical initiators commonly used in stereolithography:

- Initiators that promote radical polymerization by photo-cleavage (type I) such as, α-amino ketones, benzoin ether derivatives, benzyl ketal, hydroxyalkylphenones, acylphosphine oxides, etc.

- Initiators that promote radical polymerization by hydrogen abstraction (type II) such as, aromatic diketones, benzophenone, xanthones, thioxanthones, phenylglyoxalates, camphorquinone, etc.

Onium salts, such as iodonium and sulfonium salts, are frequently used as *cationic* initiators because they generate reactive species when exposed to UV light. However, most of the onium salts absorb below 350 nm but, with sensitizers such as polycyclic aromatic hydrocarbons or aromatic ketones, the light yield can be increased. Other cationic photoinitiators are metallocene salts that can be used in combination with oxidizing agents.

Originally, free radical systems based on acrylate and methacrylate monomers were widely used in resins for DLP-stereolithography. However, acrylates are flammable, have an unpleasant odor, and might be dangerous.

1.4.3 Absorbers

Light absorbers reduce the penetration of light into the resin and limit the curing depth. The most commonly used UV absorbers are benzotriazole derivatives. Bail et al. [129] added the color-neutral UV absorbing additive 2-(2-hydroxyphenyl)-benzotriazole derivative in the acrylic resin in order to investigate the UV-absorber effect in the microstereolithography (operating wavelength at 405 nm).

Benzotriazoles are well-known light stabilizers that reduce the detrimental effects of long exposure to UV radiation such as in organic components or polymers. Bail demonstrated that the addition of 0.2 mol% of benzotriazole derivative effectively enhances the dimensional and geometrical properties of the stereolithography process even if the printing times slightly increased.

1.4.4 Fillers

A high content of fillers is beneficial to reduce the shrinkage of the printed parts during the binder burnout. The dimension of the filler particles must be smaller than the layer height [87]. As previously mentioned, in highly filled resins with particles in the size range of the light wavelength, scattering happens and affects resolution and cure depth. By reducing the difference between the refractive index of the matrix and the filler ,scattering decreases [91].

Badev et al. [112] explored the influence of the size and concentration of the filler particles (SiO_2, Al_2O_3, ZrO_2 and SiC) to the acrylate oligomer. They studied the

rheological behavior and reactivity of the slurry under UV radiation by stereolithography.

The study of the rheology of the suspensions after the addition of the fillers showed that the overall rheology did not affect the kinetics of photopolymerizatio

1.4.5 Additives

Rheological additives and stabilizers are necessary for extending shelf-life of slurries as well as stability during long printing jobs. Agglomeration and sedimentation of particles need to be avoided to ensure the homogeneity of the slurry. To this aim, dispersants such as oligomeric surfactants, long-chained acids like oleic acid [103], or phosphine oxides with aliphatic chains can be used [130].

1.4.6 Dispersing Agents

Thanks to the high molecular weight, the addition of the dispersant endows the ceramic powders with a thicker adsorption polymer layer leading to a stronger steric/electrostatic repulsion force offsetting the Van der Waals attractive force. After surface modification generated by the dispersant, the ceramic particles turn from surface hydrophilic to hydrophobic ones, which is beneficial for the wettability of powders into the resin thanks to the analogous chemical structure between the hydrophobic groups of the dispersant and the acrylate resin. The dispersant helps to reduce the network structure degree and the viscosity thus, the powders are homogeneously packed in the slurry. The addition of the dispersant enables the production of slurries with an enhanced solid loading, inhibits flocculation, and facilitates the spontaneous spreading of suspension.

The resin is an acrylate-based organic solution, the ion intensity is weak to generate zeta potential and the steric repulsion takes over [131,132]. The hydrophobic group ofdispersant should be highly compatible with the organic medium, if not the inter- particle interaction will lead to attractive forces. [133].

According to the DLVO theory, dispersants provide homogeneous dispersions, maintain desired rheological behavior, and interact with the particles by balancing the attractive and repulsive forces [107,134].

The nature of the interactions between the particles could be hard-sphere, electrostatic, steric or van der Waals. When particles act as a hard-sphere, the hard-sphere interaction takes place. The radius of the hard-sphere, R_{HS}, is bigger than the core radius at natural stability. Strong repulsive forces and a reduced hard-sphere diameter are caused by particle contact. The formation of agglomerates occurs when the ion concentration in an aqueous system increases and the interference between the double layers becomes strong enough for the van der Waals forces to take control. [95,134,135].

Three types of van der Waals interactions exist: dispersion (London), dipole-dipole (Keesom), and dipole-induced dipole (Debye). The strongest one is the London interaction. In absence of repulsive forces, the migration of the electron between two atoms produces high attraction between the particles. A stable colloidal is obtained when the attracting and repelling forces are in balance [95,136].

When the surface of the particles contains thick layers of surfactant, steric interaction occurs, the polymer segments' density in the interaction area increases, and the pressure forces the particles to separate. Steric stabilization happens when a polymer chain anchors the surface of a ceramic particle and the other side dissolves in the liquid phase. Surfactants are classified on the base of the nature of molecule charges: anionic, cationic, amphoteric, and non-ionic ones.

Anionic surfactants contain a negative hydrophobic part (alkali sulfonate, alkali sulphate, carboxylate, or phosphate group) with a hydrocarbon chain and/or a ring. Cationic surfactants consist of a positive hydrophobic group around pentavalent nitrogen. Depending on the pH of the solutions, amphoteric substances can operateas anionic or cationic surfactants. Non-ionic surfactants are not electrically charged, and the molecules react with water by ionizing or hydrogen bonding. The hydrophilic group is constituted of a hydroxyl group and/or ether bonds and their solubility in water is affected by the amount of surfactants and the solution' temperature [134].

Attractive and repulsive forces, viscous forces, and Brownian randomizing affect the flocculation that occurs when the ceramic particles overcome the energy barrier or when the energy barrier between particles is low. A flocculated suspension is unstable even if this phenomenon could be reversible or irreversible. When it is reversible, the attraction forces between the particles are weak, (figure 1.18 d-f), while on the contrary, in the irreversible case, the attraction forces between the particles are strong, (figure 1.18 a-c), this happens due to poor mixing conditions.

Xu et al. [133] successfully prepared UV-curable Al_2O_3 suspensions with the addition of 2 wt% of the commercial dispersant Disperbyk-111. They achieved a high solid loading of 55 vol%, and a low viscosity of 1.04 Pa.s at 30 s^{-1}. Through DLP-stereolithography, they printed complex-shaped parts with high density.

Sokola et al. [137] used the Disperbyk-103 to create stable zirconia slurries with a suitable viscosity (0.93 Pa.s at a shear rate of 10 s^{-1}) and high solid loading (40 vol%) thanks to the addition of 10 wt% (respect to the weight of powder) of BYK-103. Sintered parts with a 98.2% of TD were obtained.

Caillet et al. [74] investigated high loading photocurable slurries (45 vol%) prepared with Y-TZP, Ce-TZP and Ce-TZP/Al_2O_3. A viscosity of 10 Pa s^{-1} at 150 s^{-1} was obtained through the addition of 2 wt% of Disperbyk 111. CeO_2 is a well-known UV-absorbing material because of its wide band gap (3.37 eV); in Ce-TZP and Ce-TZP/Al_2O_3 affects the curing behavior, but the addition of the photoinitiators

BAPO (phenylbis (2,4, 6-trimethyl- benzoyl)phosphine oxide) and MMMP (2-methyl-4′-methylthio-2- morpholinopropiophenon) enables to achieve a layer thickness of 75 μm.
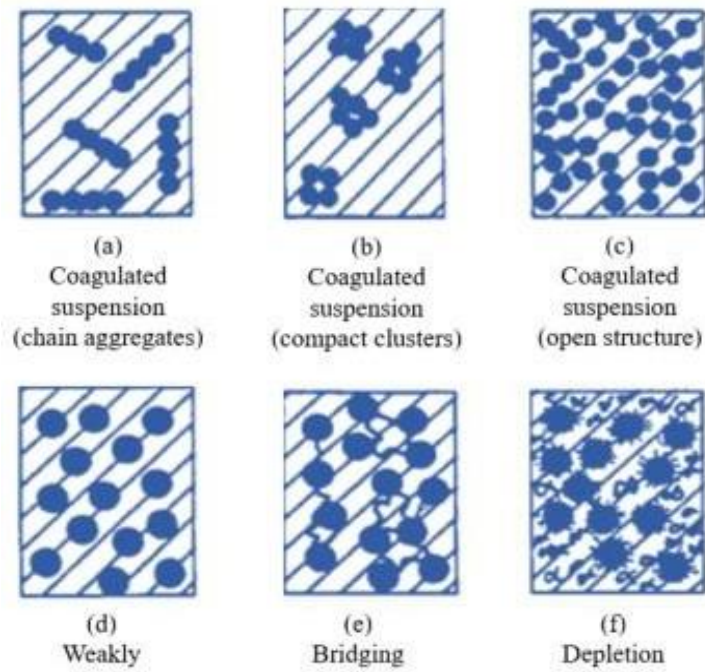

Figure 1.18: States of flocculation in suspensions [136]

1.5 Debinding

The debinding is considered the most critical step of the vat-photopolymerization process, it depends on several parameters, such as the slurry solid loading, the binders' chemical composition and the dimensions of the parts.

The debinding is the longest phase (80-100 hours are common) of the manufacturing process. Defects such as cracks, delamination, deformation, and collapse may occur, compromising the quality of the sintered parts [108].

During the debinding step, the polymerized resin, which acts as a matrix for the ceramic powder, decomposes and evaporates at high temperatures in a controlled temperature program. The burn-out of the organic compounds leads to shrinkage and the weight loss is proportional to the amount of organic matter in the slurry [98]. Thermogravimetric analysis (TGA) and Fourier transform infrared (FT-IR) spectroscopy are used to select the appropriate thermal cycle for debinding.

The success of the debinding process increases with an increase in the 'surface to volume ratio' of the parts: porous and reticulated structures are easier to debind compared to full dense parts or parts with thick walls. Furthermore, the gaseous pyrolysis products' mean diffusion length is important. Thinner parts are easier to debind than the thicker ones and spheres are the most challenging structures to debind. The optimization of the debinding cycles for specific geometries as well as for the type of ceramic powder and the used organic substances [98] is necessary in order to avoid cracks formation and distortions in final shape dimensions.

Previous studies [108,138] reported that, typically, mass loss starts at ~ 200 °C, and nearly complete organic material decomposition occurs below ~ 600 °C. The process is also influenced by physical characteristics like the particle size distribution and the quantity of filler material. After debinding, the parts are further heated to the sintering temperature of the ceramic powder to reduce the porosity and obtain dense ceramic parts [98].

Wang et al. [102] reported a two-step process: a low-temperature debinding (200–300

°C) and a high-temperature debinding (300–600 °C). In low-temperature debinding, the decomposition gases migrate from inside to outside via the formed interconnected pores. In the high temperature one, carbon oxidize after binder decomposition, and expanded CO_2 is released with consequent formation of cracks. To optimize the process and prevent fractures, slow ramps and extended temperature holding times may be necessary, resulting in a lengthy debinding procedure (on the order of up to 100 h).

Liu et al. [139], manufactured UV curable suspensions with low viscosity with the stereolithography technique. They adopted a 16 h debinding to transform green parts into transparent glassware. The evaporation of unpolymerized monomers provokes the formation of penetrating tunnels that help the organic matter escape out of the green parts thus, it was possible to adopt a fast debinding program.

By the addition of non-reactive diluents (butoxy ethyl acetate (BEA) and poly(ethylene glycol) 200 (PEG-200)) into the resin, Johansson [55] reduced the shrinkage, delamination, and intra-laminar cracks of the parts that typically occur during the debinding step. The non-reactive components decrease the shrinkage, reducing built-in stresses in the printed parts since they decompose rather than evaporate, leading to less residual porosity.

Zhou [140] et al. adopted a two-step debinding procedure consisting first of a vacuum pyrolysis step and a following air debinding. In addition, they used a liquid desiccant-based (PEG 400) drying process to decrease the shrinkage of the green parts during drying and improve the density. Highly dense (99.3% of TD) and defect-free Al_2O_3 cutting tools were fabricated via stereolithography. The Vickers hardness of the sintered parts was ~17.5 GPa.

According to Pfaffinger et al. [98] the debinding is highly influenced by the geometry and the dimension of the ceramic particles. Ceramic particles with a mean particle size < 1μm negatively affect the debinding process by increasing the risk of intralaminar cracks because of the micrometer pores limiting the diffusion of the

burn-off gases. Pfaffinger assets that one solution is the increasing of the debinding time.

Li at al. [141] studied the effect of the debinding under argon atmosphere of alumina ceramics printed via stereolithography. They observed a reduction of the volatilization rate of organics as respect to an air atmosphere by reducing the cracks and deformation of samples. The optimal debinding temperature was 500 °C which displayed a shrinkage of 2.3%, 1.9% and 3.4% in the X, Y and Z direction, respectively. At this temperature the open porosity was 35.6%.

He et al. [80] fabricated complex-shaped ZrO_2 ceramic parts through DLP-stereolithography. They used a two-step debinding cycle in order to inhibit the defects. At first, a vacuum debinding was performed to limit the decomposition rate of organic compounds of the green parts. Secondly, air debinding was performed

to remove the carbon residues. This two-step method effectively reduces defects such as cracks and bubbles. After sintering, they obtained a TD of 97.14%.

1.6 Sintering

To remove organic components from as-printed ceramic green bodies, post-debinding and sintering at high temperatures are required [106].

Sintering is the densification process of compacted powder, to reach the dense final ceramic product, in which interparticle pores are eliminated by atomic diffusion driven by thermal energy. A reduction of the inner and outer surface areas happens. The atomic diffusion may cause unavoidable grain growth besides contributing to densification, which are two competing processes in sintering. Higher density generally results in improvement of properties like strength and toughness. The literature has not paid much attention to the sintering kinetics of the SLA and DLP-streteolithography based 3D printed systems until now [142].

Borlaf et al. [71] developed zirconia and ATZ (alumina toughened zirconia, a zirconia matrix with alumina particles, at 20 wt% Al_2O_3) then printed through UV-LCM-DLP additive manufacturing technology. They sintered the printed samples at 1450 °C for 2 h, reaching a high fired density (~99%) and flexural strength (~800 MPa). Wu et al. [142] studied SLA-based 3D printed Al_2O_3 and CeO_2/ZrO_2 co-doped Al_2O_3 to observe the densification degree and grain growth. Full densification could be realized at 1550 °C with fine grains for Ce–ZrO_2/Al_2O_3 (figure 1.19).
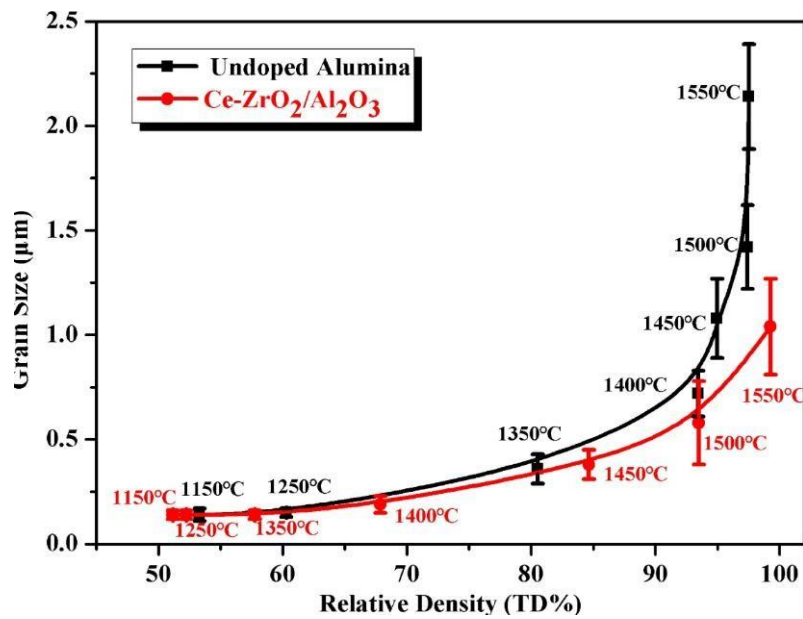
Figure 1.19 The sintering kinetic (Grain size versus TD %) of pure alumina and Ce$-$ZrO$_2$/Al$_2$O^{3}[142]

1.7 Mechanical properties

In ATZ (alumina toughened zirconia) composites, alumina provides high hardness, while tetragonal zirconia confers toughness, on account of its controlled change into the monoclinic phase. Despite the t $\rightarrow$ m phase transformation around the crack formation is the primary toughening mechanism, microcracking, crack deflection and bridging can also contribute to improve toughness. ATZ is highly used in structural ceramic applications, and biomedical applications, since its mechanical properties and toughness, tribological properties and biocompatibility are favoring implants' lifetime [143].

In ceramics with ZrO$_2$ matrix, the addition of Al$_2$O$_3$ inhibits the development of pores, which improves the densification and the mechanical properties. Besides, Al$_2$O$_3$ ceramics have a high modulus of elasticity, and their dispersion in the ZrO$_2$

matrix can play a role in pinning as well as bending and deflecting cracks, which enhances the fracture toughness [144]. As the amount of alumina increases the transformability of zirconia decreases. At first, the addition of alumina induces in the ZrO_2 matrix tensile residual cooling stress facilitating the phase transformation. The compressive stresses formed during transformation limits the toughness and the transformability.

Regarding the mechanical properties of ATZ composites, it is fundamental to take into account the residual stress generated in the matrix because of the mismatch in the thermal expansion coefficient of alumina (8×10^{-6} K^{-1}) and zirconia matrix (10.3×10^{-6} K^{-1}) resulting from the formation of hoop tensile and radial compressive stresses near the free surface [145]. The stiffer alumina counteracts the transformation toughening of the tetragonal zirconia by producing compressive stresses in the matrix [146]. This phenomenon makes the zirconia grains stable and unable to react quickly to external stresses. Thus, when a crack propagates, higher fracture energies are necessary for the crack to continue the damage started. This crack deflection mechanism enhancement fracture toughness. A higher transformability in porous than in dense bodies can be assumed due to the less effect of the constraining matrix as the porosity increases. The residual tensile stresses on the zirconia grains decrease by increasing porosity negatively affecting their tendency to transform [147].

The improvement in the ATZ mechanical properties is related also to other mechanisms such as crack deflection around the harder Al_2O_3 grains, even if this phenomenon is irrelevant for fine grain materials. When a crack tip reaches the alumina grain the crack have two possibilities: either it propagates through the alumina particles (transgranular fracture) or along the zirconia/alumina boundary (deflection) [148].

Schwarzer et al. [58] realized highly complex alumina-toughened zirconia (ATZ) ceramics via DLP-stereolithography. The sintered bodies showed a density of up to 5.45 g/cm³ and a homogeneous grain size distribution, no defects or pores, and a biaxial strength of 430 MPa.

Borlaf and al. [71] fabricated ZrO_2 and ATZ ceramics via UV-LCM-DLP. The printed parts with TD of ~99% for both the materials were subjected to 4-point bending test, obtaining for both a flexural strength of ~ 800 MPa.

Fournier at al. [149] produced 11Ce-TZP-based composites containing 8 vol% of alumina and 8 vol% of strontium aluminate through stereolithography. The SLA samples showed an enhanced plastic deformation (failure strain of 0.65%) compared to the samples obtained via cold isostatic pressing (failure strain of 0.35%). Although, the bending strengths (4PB) showed very close values: 560 MPa for the printed samples and 560 for the pressed ones. A TD of 98.8 and 98.9 was obtained for the SLA and the pressed sample respectively.

Osman printed zirconia dental implants with DLP technology. They obtained a high flexure strength value (943 MPa) comparable to the milled one (800–1000 MPa) [150]. According to the literature there are no relevant differences in the mechanical performance between the parts printed by SLA and DLP-stereolithography, due to the high similarity in the printing processing systems used in both technologies [143].

In the last 20 years, conventional forming methods such as pressing and colloidal technologies achieved high levels in terms of the performance of the final parts. High densification combined with geometric complexity is easier to accomplish with colloidal-based than in powder-based technologies, of this reason suspension-based additive manufacturing technologies (i.e robocasting, SLA, DLP, LCM) are promising.

Nowadays AM technologies, suitable for low-volume production but complex-shaped parts, have begun to substitute traditional processing even if conventional processing is still unbeatable in terms of mass production and low costs.

According to the literature, in the AM field, stabilized zirconia is more studied than alumina due to its widespread use in the healthcare market [151].

1.8 Conclusions

In this chapter the state of the art of DLP-stereolithography of zirconia-based ceramics was discussed.

In the first part, an overview of the most relevant zirconia – alumina composites and a brief description of the transformation toughening proper of zirconia materials and its consequences on the mechanical properties can be found.

The second part of the chapter is focused on the DLP-stereolithography printing technique of zirconia-based ceramics. The overview on the DLP-stereolithography of the Ce-TZP composites has revealed a gap in the scientific literature: few papers related to the 3D printing of ceria stablized zirconia have been reported and the main parameters able to affect the mechanical properties of zirconia ceramics fabricatedby DLP-stereolithography have not yet been deeply investigated.

Starting from this background, the aim of this study is the development of dense and homogeneous Ce-ZrO_2/Al_2O_3 composites, through a careful preparation of printable slurries.

References

1. Saridag, S., Tak, O. & Alniacik, G. Basic properties and types of zirconia: An overview. *World J. Stomatol.* **2**, 40 (2013).

2. Helmer, J. D. & Driskell, T. D. Research on bioceramics. *Clemson Univ. South Carolina* Research on bioceramics. In: Symposium on Use of C (1969).

3. Piconi, C. & Maccauro, G. Zirconia as a ceramic biomaterial. *Biomaterials* (1999). doi:10.1016/S0142-9612(98)00010-6

4. Chevalier, J. & Gremillard, L. *Zirconia as a biomaterial*. *Comprehensive Biomaterials* **1**, (Elsevier Ltd., 2011).

5. Shukla, S. & Seal, S. Mechanisms of room temperature metastable tetragonal phase stabilisation in zirconia. *Int. Mater. Rev.* **50**, 45–64 (2005).

6. Jin, X. J. Martensitic transformation in zirconia containing ceramics and its applications. *Curr. Opin. Solid State Mater. Sci.* **9**, 313–318 (2005).

7. Brog, J. P., Chanez, C. L., Crochet, A. & Fromm, K. M. Polymorphism, what it is and how to identify it: A systematic review. *RSC Adv.* **3**, 16905–16931 (2013).

8. Ruff, O. & Ebert, F. Contributions on the Ceramics of Highly Fireproof Material I: The Forms of Zirconium Dioxide. *Z. Anorg.Allg.Chem* 19–41 (1929).

9. Chevalier, J., Gremillard, L., Virkar, A. V. & Clarke, D. R. The tetragonal-monoclinic transformation in zirconia: Lessons learned and future trends. *J. Am. Ceram. Soc.* **92**, 1901–1920 (2009).

10. Daou, E. E. The zirconia ceramic: strengths and weaknesses. *Open Dent J.* 33–42 (2014). doi:10.2174/1874210601408010033

11. Antoniac, I. & Palmero, P. Bioceramics and Biocomposites : From Research to Clinical Practice. in (2019).

12. Ćorić, D., Majić Renjo, M. & Ćurković, L. Vickers indentation fracture

toughness of Y-TZP dental ceramics. *Int. J. Refract. Met. Hard Mater.* **64**, 14–19 (2017).

13.   Bikramjit, B. & Mitjan, K. *Tribology of ceramics and composites*. (Wiley, 2011).

14.   Chevalier, J., Gremillard, L., Virkar, A. V. & Clarke, D. R. The tetragonal-monoclinic transformation in zirconia: Lessons learned and future trends. *J. Am. Ceram. Soc.* (2009). doi:10.1111/j.1551-2916.2009.03278.x

15.   Garvie, R. C. The occurrence of metastable tetragonal zirconia as a crystallite size effect. *J. Phys. Chem.* **69**, 1238–1243 (1965).

16.   Chevalier, J. & Gremillard, L. Zirconia as a biomaterial. In: Comprehensive Biomaterials. in 95–108 (Elsevier, 2011).

17.   Fornabaio, M. *et al.* Zirconia-based composites for biomedical applications: Role of second phases on composition, microstructure and zirconia transformability. *J. Eur. Ceram. Soc.* **35**, 4039–4049 (2015).

18.   Kobayashi, K., Kuwajima, H. & Masaki, T. Phase change and mechanical properties of ZrO2-Y2O3 solid electrolyte after ageing. *Solid State Ionics* **3–4**, 489–493 (1981).

19.   Donat, L., Osswald, B. & Kern, F. 1Yb-2Sm-TZP, a new co-stabilized zirconia material with high toughness and low temperature degradation resistance. *J. Eur. Ceram. Soc.* **43**, 2843–2851 (2022).

20.   Chacun, D. *et al.* Histologic and histomorphometric evaluation of new zirconia-based ceramic dental implants: A preclinical study in dogs. *Dent. Mater.* **37**, 1377–1389 (2021).

21.   Chevalier, J. What future for zirconia as a biomaterial? *Biomaterials* **27**, 535–543 (2006).

22.   Lawson, S. Environmental degradation of zirconia ceramics. *J. Eur. Ceram. Soc.* **15**, 485–502 (1995).

23.   Sato, T. & Shimada, M. Transformation of Ceria-doped tetragonal zirconia polycrystals by annealing in water. *Am. Ceram. Soc. Bull* **64 [10]**, 1382–4 (1985).

24. Palmero, P. *et al.* Towards long lasting zirconia-based composites for dental implants: Part I: Innovative synthesis, microstructural characterization and invitro stability. *Biomaterials* **50**, 38–46 (2015).

25. Tsukuma, K. & Shimada, M. Strength , fracture toughness and Vickers hardness of CeO2-stabilized tetragonal. *J. Mater. Sci. K., Shimada, M. (1985). Strength , Fract. toughness Vickers hardness CeO2-stabilized tetragonal. J. Mater. Sci. 20(1 985), 1178–1184.* **20**, 1178–1184 (1985).

26. Fornabaio, M. Composites in the Alumina-Zirconia system: an engineering approach for an effective tailoring of microstructural features and performances. (Politecnico di Torino, 2014).

27. Masatomo Yashima, Hiroyuki Takashina, Masato Kakihana & Masahiro Yoshimura. Low Temperature Phase Equilibria by the Flux Method and the Metastable-Stable Phase Diagram in the Zr0,-CeO, System. *J. Am. Ceram. Soc.* **77**, 1869–1874 (1954).

28. Hannink, R. H. J., Kelly, P. M. & Muddle, B. C. Transformation toughening in zirconia-containing ceramics. *J. Am. Ceram. Soc.* **83**, 461–487 (2000).

29. Tsai, J. -F, Yu, C. -S & Shetty, D. K. Fatigue Crack Propagation in Ceria-Partially-Stabilized Zirconia (Ce-TZP)-Alumina Composites. *J. Am. Ceram. Soc.* **73**, 2992–3001 (1990).

30. Yu, C.S.; Shetty, D.K.; Marshall, D. B. Transformation Zone Shape Effects on Crack Shielding in Ceria-Partially-Stabilized Zirconia (Ce-TZP)–Alumina Composites. *J. Am. Ceram. Soc.* **75 (11)**, 2991–2994 (1992).

31. Schmid, H. K., Pennefather, R., Meriani, S. & Schmid, C. Redistribution of Ce and La during processing of Ce(La)-TZP/Al2O3 composites. *J. Eur. Ceram. Soc.* **10**, 381–392 (1992).

32. Sato, T., Endo, T. & Shimada, M. Postsintering Hot Isostatic Pressing of Ceria-Doped Tetragonal Zirconia/Alumina Composites in an Argon–Oxygen Gas Atmosphere. *J. Am. Ceram. Soc.* **72**, 761–764 (1989).

33. Nawa, M., Bamba, N., Sekino, T. & Niihara, K. The effect of TiO2 addition on strengthening and toughening in intragranular type of 12Ce-TZP/Al2O3

nanocomposites. *J. Eur. Ceram. Soc.* **18**, 209–219 (1998).

34. Cutler, R. A., Mayhew, R. J., Prettyman, K. M. & Virkar, A. V. High-Toughness Ce-TZP/Al2O3 Ceramics with Improved Hardness and Strength. *J. Am. Ceram. Soc.* **74**, 179–186 (1991).

35. Bain, E. Trans AIME. 70:25 (1924).

36. Deville, S., Guénin, G. & Chevalier, J. Martensitic transformation in zirconia part II. Martensite growth. *Acta Mater.* **52**, 5709–5721 (2004).

37. Deville, S., Guénin, G. & Chevalier, J. Martensitic transformation in zirconia Part I. Nanometer scale prediction and measurement of transformation induced relief. *Acta Mater.* **52**, 5697–5707 (2004).

38. Kelly, P. M. & Rose, L. R. F. The martensitic transformation in ceramics - Its role in transformation toughening. *Prog. Mater. Sci.* **47**, 463–557 (2002).

39. Lange, F. F. Transformation Toughening. 1 Size Effects Associated with the Thermodynamics of Constrained Transformations. *J. Mater. Sci.* 225–34 (1982).

40. Zhang, X., Wu, X. & Shi, J. Additive manufacturing of zirconia ceramics: a state-of-the-art review. *J. Mater. Res. Technol.* **9**, 9029–9048 (2020).

41. Chen, Y. W., Moussi, J., Drury, J. L. & Wataha, J. C. Zirconia in biomedical applications. *Expert Rev. Med. Devices* **13**, 945–963 (2016).

42. Kelly, J. R. & Denry, I. Stabilized zirconia as a structural ceramic: An overview. *Dent. Mater.* **24**, 289–298 (2008).

43. Badwal, S. P. S., Ciacchi, F. T. & Zelizko, V. The effect of alumina addition on the conductivity, microstructure and mechanical strength of zirconia - yttria electrolytes. *Ionics (Kiel).* **4**, 25–32 (1998).

44. Lee, J. H. Review on zirconia air-fuel ratio sensors for automotive applications. *J. Mater. Sci.* **38**, 4247–4257 (2003).

45. Montanaro, L., Coppola, B., Palmero, P. & Tulliani, J. M. A review on aqueous gelcasting: A versatile and low-toxic technique to shape ceramics. *Ceram. Int.* **45**, 9653–9673 (2019).

46. Cramer, C. L. *et al.* Accuracy of stereolithography printed alumina with

digital light processing. *Open Ceram.* **8**, 100194 (2021).

47. Dehurtevent, M. *et al.* Effect of build orientation on the manufacturing process and the properties of stereolithographic dental ceramics for crown frameworks. *J. Prosthet. Dent.* **125**, 453–461 (2021).

48. Zhang, K. *et al.* High solid loading, low viscosity photosensitive Al2O3 slurry for stereolithography based additive manufacturing. *Ceram. Int.* **45**, 203–208 (2019).

49. Hanuhov, T., Asulin, E. & Gvishi, R. Evaluation of opto-mechanical properties of UV-cured and thermally-cured sol-gel hybrids monoliths as a function of organic content and curing process. *J. Non. Cryst. Solids* **471**, 301–311 (2017).

50. Yokota, K. & Takahara, S. Fabrication of three-dimensional dense alumina ceramics by DLP stereolithography. *J. Soc. Powder Technol. Japan* **53**, 492–498 (2016).

51. Li, H. *et al.* Influence of Vacuum Debinding Temperature on Microstructure and Mechanical Properties of Three-Dimensional-Printed Alumina via Stereolithography. *3D Print. Addit. Manuf.* **7**, 8–18 (2020).

52. Wu, H. *et al.* Effect of the particle size and the debinding process on the density of alumina ceramics fabricated by 3D printing based on stereolithography. *Ceram. Int.* **42**, 17290–17294 (2016).

53. Chen, S. *et al.* Effects of particle size distribution and sintering temperature on properties of alumina mold material prepared by stereolithography. *Ceram. Int.* **48**, 6069–6077 (2022).

54. Shuai, X., Zeng, Y., Li, P. & Chen, J. Fabrication of fine and complex lattice structure Al2O3 ceramic by digital light processing 3D printing technology. *J. Mater. Sci.* **55**, 6771–6782 (2020).

55. Johansson, E., Lidström, O., Johansson, J., Lyckfeldt, O. & Adolfsson, E. Influence of resin composition on the defect formation in alumina manufactured by stereolithography. *Materials (Basel).* **10**, (2017).

56. Liu, W. *et al.* Synergy of solid loading and printability of ceramic paste for

optimized properties of alumina via stereolithography-based 3D printing. *J. Mater. Res. Technol.* **9**, 11476–11483 (2020).

57. Xing, H. *et al.* Preparation and characterization of UV curable Al2O3 suspensions applying for stereolithography 3D printing ceramic microcomponent. *Powder Technol.* **338**, 153–161 (2018).

58. Schwarzer, E. *et al.* Process development for additive manufacturing of functionally graded alumina toughened zirconia components intended for medical implant application. *J. Eur. Ceram. Soc.* (2019). doi:10.1016/j.jeurceramsoc.2018.09.003

59. Schwentenwein, M. & Homa, J. Additive manufacturing of dense alumina ceramics. *Int. J. Appl. Ceram. Technol.* **12**, 1–7 (2015).

60. Zhang, K. *et al.* Roles of solid loading in stereolithography additive manufacturing of ZrO2 ceramic. *Int. J. Refract. Met. Hard Mater.* **99**, 105604 (2021).

61. Komissarenko, D. A., Sokolov, P. S., Evstigneeva, A. D., Shmeleva, I. A. & Dosovitsky, A. E. Rheological and curing behavior of acrylate-based suspensions for the DLP 3D printing of complex zirconia parts. *Materials (Basel).* **11**, (2018).

62. Song, S. Y., Park, M. S., Lee, D., Lee, J. W. & Yun, J. S. Optimization and characterization of high-viscosity ZrO2 ceramic nanocomposite resins for supportless stereolithography. *Mater. Des.* **180**, 107960 (2019).

63. Zhang, J. *et al.* Digital light processing-stereolithography three-dimensional printing of yttria-stabilized zirconia. *Ceram. Int.* (2020). doi:10.1016/j.ceramint.2019.12.113

64. Zhang, K. *et al.* Photosensitive ZrO 2 suspensions for stereolithography. *Ceram. Int.* **45**, 12189–12195 (2019).

65. Han, Z. *et al.* A Novel ZrO2 Ceramic Suspension for Ceramic Stereolithography. *IOP Conf. Ser. Mater. Sci. Eng.* **678**, (2019).

66. Borlaf, M., Serra-Capdevila, A., Colominas, C. & Graule, T. Development of UV-curable ZrO2 slurries for additive manufacturing (LCM-DLP)

technology. *J. Eur. Ceram. Soc.* (2019). doi:10.1016/j.jeurceramsoc.2019.05.023

67. Rosa, M., Barou, C. & Esposito, V. Zirconia UV-curable colloids for additive manufacturing via hybrid inkjet printing-stereolithography. *Mater. Lett.* **215**, 214–217 (2018).

68. Li, Y. *et al.* Cure behavior of colorful ZrO2 suspensions during Digital light processing (DLP) based stereolithography process. *J. Eur. Ceram. Soc.* **39**, 4921–4927 (2019).

69. Coppola, B., Lacondemine, T., Tardivat, C., Montanaro, L. & Palmero, P. Designing alumina-zirconia composites by DLP-based stereolithography: Microstructural tailoring and mechanical performances. *Ceram. Int.* **47**, 13457–13468 (2021).

70. Zheng, T., Wang, W., Sun, J., Liu, J. & Bai, J. Development and evaluation of Al2O3–ZrO2 composite processed by digital light 3D printing. *Ceram. Int.* **46**, 8682–8688 (2020).

71. Borlaf, M., Szubra, N., Serra-Capdevila, A., Kubiak, W. W. & Graule, T. Fabrication of ZrO2 and ATZ materials via UV-LCM-DLP additive manufacturing technology. *J. Eur. Ceram. Soc.* **40**, 1574–1581 (2020).

72. Wu, H. *et al.* Fabrication of dense zirconia-toughened alumina ceramics through a stereolithography-based additive manufacturing. *Ceram. Int.* **43**, 968–972 (2017).

73. Xing, H. *et al.* Effect of particle size distribution on the preparation of ZTA ceramic paste applying for stereolithography 3D printing. *Powder Technol.* **359**, 314–322 (2020).

74. Cailliet, S., Roumanie, M., Croutxé-Barghorn, C., Bernard-Granger, G. & Laucournet, R. Y-TZP, Ce-TZP and as-synthesized Ce-TZP/Al2O3 materials in the development of high loading rate digital light processing formulations. *Ceram. Int.* **47**, 3892–3900 (2021).

75. Liau, L. C. K. & Chien, Y. C. Kinetic investigation of ZrO2, Y2O3, and Ni on poly(vinyl butyral) thermal degradation using nonlinear heating

functions. *J. Appl. Polym. Sci.* **102**, 2552–2559 (2006).

76. ISO/ASTM, 17296 Standard on Additive Manufacturing (AM) Technologies.

77. Willems, E. *et al.* Additive manufacturing of zirconia ceramics by material jetting. *J. Eur. Ceram. Soc.* **41**, 5292–5306 (2021).

78. Sun, J. *et al.* A review on additive manufacturing of ceramic matrix composites. *J. Mater. Sci. Technol.* (2022). doi:https://doi.org/10.1016/j.jmst.2022.06.039.

79. Chen, R. *et al.* Stereolithographic additive manufacturing diamond/SiC composites with high thermal conductivity for electronic 3D-packaging applications. *Ceram. Int.* **47**, 14009–14020 (2021).

80. He, R. *et al.* Fabrication of complex-shaped zirconia ceramic parts via a DLP- stereolithography-based 3D printing method. *Ceram. Int.* (2018). doi:10.1016/j.ceramint.2017.11.135

81. Sun, J., Binner, J. & Bai, J. 3D printing of zirconia via digital light processing: optimization of slurry and debinding process. *J. Eur. Ceram. Soc.* **40**, 5837–5844 (2020).

82. Chen, Z. *et al.* 3D printing of ceramics: A review. *J. Eur. Ceram. Soc.* **39**, 661–687 (2019).

83. Zocca, A., Colombo, P., Gomes, C. M. & Günster, J. Additive Manufacturing of Ceramics: Issues, Potentialities, and Opportunities. *J. Am. Ceram. Soc.* **98**, 1983–2001 (2015).

84. Galante, R., Figueiredo-Pina, C. G. & Serro, A. P. Additive manufacturing of ceramics for dental applications: A review. *Dent. Mater.* **35**, 825–846 (2019).

85. Travitzky, B. N. *et al.* Additive Manufacturing of Ceramic-Based Materials **. 1–26 (2014). doi:10.1002/adem.201400097

86. Al Rashid, A., Ahmed, W., Khalid, M. Y. & Koç, M. Vat photopolymerization of polymers and polymer composites: Processes and applications. *Addit. Manuf.* **47**, 102279 (2021).

87. Schmidleithner, C., Kalaskar, D. M., [w] & [red], D. C. Stereolitography, fr. 3D printing; IntechOpen. *IntechOpen* (2018).

88. Mou, Y. A. & Koc, M. Dimensional capability of selected 3DP technologies. *Rapid Prototyp. J.* **25**, 915–924 (2019).

89. Lee, J. M., Sing, S. L., Zhou, M. & Yeong, W. Y. 3D bioprinting processes: A perspective on classification and terminology. *Int. J. Bioprinting* **4**, (2018).

90. Griffith, M. L. & Halloran, J. W. Freeform fabrication of ceramics via stereolithography. *Journal of the American Ceramic Society* **79**, (1997).

91. Griffith, M. L. & Halloran, J. W. Scattering of ultraviolet radiation in turbid suspensions. *J. Appl. Phys.* **81 (47)**, (1997).

92. Tomeckova, V. & Halloran, J. W. Critical energy for photopolymerization of ceramic suspensions in acrylate monomers. *J. Eur. Ceram. Soc.* **30**, 3273–3282 (2010).

93. Tomeckova, V. & Halloran, J. W. Cure depth for photopolymerization of ceramic suspensions. *J. Eur. Ceram. Soc.* **30**, 3023–3033 (2010).

94. Dehurtevent, M. *et al.* Stereolithography: A new method for processing dental ceramics by additive computer-aided manufacturing. *Dent. Mater.* **33**, 477–485 (2017).

95. Alazzawi, M. K. Stereolithography of alumina systems: cure depth and dimensional control. (Rutgers, The State University of New Jersey, 2021).

96. Jia, K. *et al.* A new and simple way to prepare monolithic solid oxide fuel cell stack by stereolithography 3D printing technology using 8 mol% yttria stabilized zirconia photocurable slurry. *J. Eur. Ceram. Soc.* **42**, 4275–4285 (2022).

97. Sun, J., Binner, J. & Bai, J. Effect of surface treatment on the dispersion of nano zirconia particles in non-aqueous suspensions for stereolithography. *J. Eur. Ceram. Soc.* **39**, 1660–1667 (2019).

98. Pfaffinger, M., Mitteramskogler, G., Gmeiner, R. & Stampfl, J. Thermal debinding of ceramic-filled photopolymers. *Mater. Sci. Forum* **825–826**, 75–81 (2015).

99. Lian, Q., Sui, W., Wu, X., Yang, F. & Yang, S. Additive manufacturing of ZrO2 ceramic dental bridges by stereolithography. *Rapid Prototyp. J.* **24**, 114–119 (2018).

100. Jiang, C. P., Hsu, H. J. & Lee, S. Y. Development of mask-less projection slurry stereolithography for the fabrication of zirconia dental coping. *Int. J. Precis. Eng. Manuf.* **15**, 2413–2419 (2014).

101. Chen, F. *et al.* Preparation and biological evaluation of ZrO2 all-ceramic teeth by DLP technology. *Ceram. Int.* **46**, 11268–11274 (2020).

102. Wang, K. *et al.* Study on defect-free debinding green body of ceramic formed by DLP technology. *Ceram. Int.* **46**, 2438–2446 (2020).

103. Li, K. & Zhao, Z. The effect of the surfactants on the formulation of UV-curable SLA alumina suspension. *Ceram. Int.* **43**, 4761–4767 (2017).

104. Wu, Z. *et al.* Research into the mechanical properties, sintering mechanism and microstructure evolution of Al2O3-ZrO2 composites fabricated by a stereolithography-based 3D printing method. *Mater. Chem. Phys.* **207**, 1–10 (2018).

105. Bae, C. J. & Halloran, J. W. Concentrated suspension-based additive manufacturing – viscosity, packing density, and segregation. *J. Eur. Ceram. Soc.* (2019). doi:10.1016/j.jeurceramsoc.2019.05.034

106. Kim, I., Kim, S., Andreu, A., Kim, J. & Yoon, Y. Influence of dispersant concentration toward enhancing printing precision and surface quality of vat photopolymerization 3D printed ceramics. *Addit. Manuf.* **52**, 102659 (2022).

107. Hinczewski, C., Corbel, S. & Chartier, T. Ceramic suspensions suitable for stereolithography. *J. Eur. Ceram. Soc.* **18**, 583–590 (1998).

108. Cai, P. *et al.* Effects of slurry mixing methods and solid loading on 3D printed silica glass parts based on DLP stereolithography. *Ceram. Int.* **46**, 16833–16841 (2020).

109. Li, X. *et al.* Dispersion and properties of zirconia suspensions for stereolithography. *Int. J. Appl. Ceram. Technol.* **17**, 239–247 (2020).

110. Zakeri, S., Vippola, M. & Levänen, E. A comprehensive review of the

photopolymerization of ceramic resins used in stereolithography. *Addit. Manuf.* **35**, 101177 (2020).

111. Zhang, K. *et al.* Roles of solid loading in stereolithography additive manufacturing of ZrO2 ceramic. *Int. J. Refract. Met. Hard Mater.* **99**, 105604 (2021).

112. Badev, A. *et al.* Photopolymerization kinetics of a polyether acrylate in the presence of ceramic fillers used in stereolithography. *J. Photochem. Photobiol. A Chem.* **222**, 117–122 (2011).

113. Pereira, F.R.; Bàrtolo, P. Photocrosslinkable Materials for the Fabrication of Tissue-Engineered Constructs by Stereolithography. in *Computational methods in applied sciences* 149–178 (Springe, Dordrecht, 2014). doi:10.1007/978-94-007-7073-7_8

114. *Stereolithography. Materials, Processes and Applications.* (Springer International Publishing, 2011). doi:10.1007/978-0-387-92904-0

115. Bagheri, A. & Jin, J. Photopolymerization in 3D Printing. *ACS Appl. Polym. Mater.* **1**, 593–611 (2019).

116. Chaudhary, R. *et al.* Additive manufacturing by digital light processing: a review. *Prog. Addit. Manuf.* (2022). doi:10.1007/s40964-022-00336-0

117. Courtois, N. Développement de nouveaux matéeriaux céramiques à base de zircone pour application dentaire. (Institute National des Sciences Appliquées de Lyon, 2011).

118. Adake, C. V., Bhargava, P. & Gandhi, P. Effect of surfactant on dispersion of alumina in photopolymerizable monomers and their UV curing behavior for microstereolithography. *Ceram. Int.* **41**, 5301–5308 (2015).

119. Halloran, J. W. *et al.* Photopolymerization of powder suspensions for shaping ceramics. **31**, 2613–2619 (2011).

120. Gentry, S. P. & Halloran, J. W. Light scattering in absorbing ceramic suspensions: Effect on the width and depth of photopolymerized features. *J. Eur. Ceram. Soc.* **35**, 1895–1904 (2015).

121. Lian, Q. *et al.* Accurate printing of a zirconia molar crown bridge using three-

part auxiliary supports and ceramic mask projection stereolithography. *Ceram. Int.* (2019). doi:10.1016/j.ceramint.2019.06.111

122. French, R. H., Müllejans, H. & Jones, D. J. Optical properties of aluminum oxide: Determined from vacuum ultraviolet and electron energy-loss spectroscopies. *J. Am. Ceram. Soc.* **81**, 2549–2557 (1998).

123. Shiraishi, T. & Watanabe, I. Thickness dependence of light transmittance, translucency and opalescence of a ceria-stabilized zirconia/alumina nanocomposite for dental applications. *Dent. Mater.* **32**, 660–667 (2016).

124. Sun, C. & Zhang, X. The influences of the material properties on ceramic micro-stereolithography. *ASME Int. Mech. Eng. Congr. Expo. Proc.* **2000-AB**, 679–685 (2000).

125. Zhang, C., Jiang, Z., Zhao, L., Guo, W. & Gao, X. Stability, rheological behaviors, and curing properties of 3Y–ZrO2 and 3Y–ZrO2/GO ceramic suspensions in stereolithography applied for dental implants. *Ceram. Int.* **47**, 13344–13350 (2021).

126. Qian, C., Hu, K., Li, J., Li, P. & Lu, Z. The effect of light scattering in stereolithography ceramic manufacturing. *J. Eur. Ceram. Soc.* **41**, 7141–7154 (2021).

127. Wu, K. C., Seefeldt, K. F., Solomon, M. J. & Halloran, J. W. Prediction of ceramic stereolithography resin sensitivity from theory and measurement of diffusive photon transport. *J. Appl. Phys.* **98**, (2005).

128. Zheng, J., Zhang, H. & Li, X. Effect of ternary particles size distribution on rheology of slurry and microstructure of DLP printed ZTA ceramic. *Mater. Chem. Phys.* **269**, 124656 (2021).

129. Bail, R., Hong, J. Y. & Chin, B. D. Effect of a red-shifted benzotriazole UV absorber on curing depth and kinetics in visible light initiated photopolymer resins for 3D printing. *J. Ind. Eng. Chem.* **38**, 141–145 (2016).

130. Goswami, A., Ankit, K., Balashanmugam, N., Umarji, A. M. & Madras, G. Optimization of rheological properties of photopolymerizable alumina suspensions for ceramic microstereolithography. *Ceram. Int.* **40**, 3655–3665

(2014).

131. Huo, W. *et al.* Effect of zeta potential on properties of foamed colloidal suspension. *J. Eur. Ceram. Soc.* **39**, 574–583 (2019).

132. Leo, S., Tallon, C. & Franks, G. V. Aqueous and nonaqueous colloidal processing of difficult-to-densify ceramics: Suspension rheology and particle packing. *J. Am. Ceram. Soc.* **97**, 3807–3817 (2014).

133. Xu, X., Zhou, S., Wu, J., Zhang, C. & Liu, X. Inter-particle interactions of alumina powders in UV-curable suspensions for DLP stereolithography and its effect on rheology, solid loading, and self-leveling behavior. *J. Eur. Ceram. Soc.* **41**, 2763–2774 (2021).

134. Smith, P. A. Particle Packing in Alumina Suspensions-rheology and Filtration Behavior. (Rutgers University, 1992).

135. Keller, J. M. Rheology and Slip Casting of Fine Alumina Systems. (Rutgers University, 1995).

136. Tharwat. F; Tadros. *Rheology of dispersions*. (Wiley, 2011).

137. Salamon, D., Sokola, P., Kalina, M. & Krousk, J. Kinetic stability and rheological properties of photosensitive zirconia suspensions for DLP printing Tom a. 31–34 (2023). doi:10.1016/j.ceramint.2023.02.223

138. Yang, W. W., Yang, K. Y., Wang, M. C. & Hon, M. H. Solvent debinding mechanism for alumina injection molded compacts with water-soluble binders. *Ceram. Int.* **29**, 745–756 (2003).

139. Liu, C., Qian, B., Liu, X., Tong, L. & Qiu, J. Additive manufacturing of silica glass using laser stereolithography with a top-down approach and fast debinding. *RSC Adv.* **8**, 16344–16348 (2018).

140. Zhou, M. *et al.* Preparation of a defect-free alumina cutting tool via additive manufacturing based on stereolithography – Optimization of the drying and debinding processes. *Ceram. Int.* **42**, 11598–11602 (2016).

141. Li, H. *et al.* Effect of debinding temperature under an argon atmosphere on the microstructure and properties of 3D-printed alumina ceramics. *Mater. Charact.* **168**, (2020).

142. Wu, H. *et al.* Sintering kinetics involving densification and grain growth of 3D printed Ce–ZrO2/Al2O3. *Mater. Chem. Phys.* **239**, 1–6 (2020).

143. Olhero, S. M. *et al.* Conventional versus additive manufacturing in the structural performance of dense alumina-zirconia ceramics: 20 years of research, challenges and future perspectives. *J. Manuf. Process.* **77**, 838–879 (2022).

144. Chen, F. *et al.* Preparation and characterization of ZrO2-Al2O3 bioceramics by stereolithography technology for dental restorations. *Addit. Manuf.* **44**, 1–8 (2021).

145. Abbas, M. K. G. *et al.* Effects of sintering additives on the densification and properties of alumina-toughened zirconia ceramic composites. *Ceram. Int.* **46**, 27539–27549 (2020).

146. Grabowy, M., Wilk, A., Lach, R. & Pędzich, Z. Hydrothermal aging of atz composites based on zirconia made of powders with different yttria content. *Materials (Basel).* **14**, 1–14 (2021).

147. Lima, E. de S. *et al.* Development and characterization of alumina-toughened zirconia (ATZ) ceramic composites doped with a beneficiated rare-earth oxide extracted from natural ore. *J. Mater. Res. Technol.* **16**, 451–460 (2022).

148. Zhang, F., Li, L. feng & Wang, E. ze. Effect of micro-alumina content on mechanical properties of Al2O3/3Y-TZP composites. *Ceram. Int.* **41**, 12417–12425 (2015).

149. Fournier, S. *et al.* Ceria-stabilized zirconia-based composites printed by stereolithography: Impact of the processing method on the ductile behaviour and its transformation features. *J. Eur. Ceram. Soc.* (2022). doi:10.1016/j.jeurceramsoc.2022.11.006

150. Osman, R. B., van der Veen, A. J., Huiberts, D., Wismeijer, D. & Alharbi, N. 3D-printing zirconia implants; a dream or a reality? An in-vitro study evaluating the dimensional accuracy, surface topography and mechanical properties of printed zirconia implant and discs. *J. Mech. Behav. Biomed.*

Mater. **75**, 521–528 (2017).

151. Olhero, S. M. *et al.* Conventional versus additive manufacturing in the structural performance of dense alumina-zirconia ceramics: 20 years of research, challenges and future perspectives. *J. Manuf. Process.* **77**, 838–879 (2022).

Chapter 2

Elaboration and characterization of *ZA$_{16}$Ce$_{11}$* powder

In this chapter, the procedure to prepare Ceria (CeO$_2$) stabilized zirconia (ZrO$_2$)-based composite powder, which will be used as powder in photocurable slurries printable with the digital light processing technique, is described.

The studied ceramic composite composition is 84 vol% ZrO$_2$ (11 mol% CeO$_2$) and 16 vol% Al$_2$O$_3$ (denoted *ZA$_{16}$Ce$_{11}$*).

The adopted process for the elaboration of the bi-phasic powder is described in section 2.1. In section 2.2, the dispersion method and the study on the choice of the appropriate dispersant are depicted. The last paragraph, 2.3, is dedicated to the characterization of *ZA$_{16}$Ce$_{11}$* from the microstructural and crystallographic point of view.

2.1 Elaboration of *ZA₁₆Ce₁₁* bi-phasic powder

To obtain the bi-phasic composition 84 vol% ZrO_2 (11 mol% CeO_2) and 16 vol% Al_2O_3 (denoted *ZA₁₆Ce₁₁* hereafter), selected commercial powders (α-Al_2O_3, 10Ce-ZrO_2 and 12Ce-ZrO_2, more details in section 2.1.1) were dispersed in ethanol. Ethanol was selected as the liquid medium for the dispersion to limit the formation of "hard" agglomerates that arise in aqueous systems during the drying of the powders. When agglomerates are easily crushed, and the constituents have the capability of being distributed uniformly, they are referred to as "soft", and those without this capability are referred to as "hard" [1]. For this reason, a nonaqueous liquid medium, such as ethanol, was chosen to form easily crushable "soft" agglomerates. The dispersibility of the as-received powders were investigated by using the ball milling technique. Zirconia spheres (2.0 mm in diameter, supplied by Tosoh Corporation) were employed and a laser-granulometer was used to check the particle size distribution in function of the milling time. The study of the dispersibility was carried out by using a solid loading of 10 wt% and a powder-to-spheres weight ratio of 1:10. A good dispersion with a monomodal narrow particle size distribution was reached after 18 hours of ball-milling. The suspension was dried on a hot plate magnetic stirrer at 60 °C until the evaporation of the liquid medium and then was left in an oven overnight at 60 °C to complete the drying. The dried Ce-ZA_{16} composite powder was sieved by means of a sieve with apertures of 125 μm. Figure 2.1 shows the flow chart of the adopted procedure.
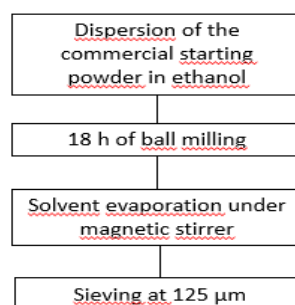
Figure 2.1 Flow chart of the composite powder elaboration procedure

2.1.1 Characterization of the starting powders

ZA$_{16}$Ce$_{11}$ bi-phasic powder was prepared with the ceria-stabilized zirconia (Ce-ZrO$_2$) supplied by Daiichi Kigenso (Kagaku Kogyo Co. ltd, Japan). Two typologies of Ce-ZrO$_2$ powders were employed, containing 10 mol% (10Ce-ZrO$_2$) and 12 mol% (12Ce-ZrO$_2$) of ceria in order to obtain the final amount of 11 mol% of ceria in the zirconia lattice. Other information supplied by the producer [2] are collected in Table 2.1.

10Ce-TZP powder		12Ce-TZP powder	
Item	Analysis results	Item	Analysis results
ZrO$_2$ (+HfO$_2$)	86.39 wt%	ZrO$_2$ (+HfO$_2$)	83.4 wt%
CeO$_2$	13.37 wt%	CeO$_2$	15.6 – 16.4 wt%
Al$_2$O$_3$	0.23 wt%	Al$_2$O$_3$	0.25 wt%
Specific surface area	14.3 m^2/g	Specific surface area	10-15 m^2/g
Particle size (D50)	0.5-1.0 μm	Particle size (D50)	0.5-1.0 μm
Green density	2.91 g/cm^3	Green density	2.91 g/cm^3

Table 2.1 Technical data sheet of Daiichi 10Ce-TZP (sx) and 12Ce-TZP (dx) powders

In order to have α-alumina as a second phase, alumina powder TM-DAR TAIMICRON supplied by *Taimei Chemicals Co., Japan* was selected. The main features of the powder provided by the supplier [3] are reported in Table 2.2.

α-alumina powder	
Crystalline phase	Alpha
Specific surface area	14.5 (m^2/g)
Particle size (D50)	0.10 μm
Purity (by ICP-AES)	99.99%
Impurities (ppm) (by ICP-AES)	Si (10) Fe (8) Na (8)

Table 2.2 Technical data of TM-DAR TAIMICRON alumina powder

The XRD pattern of the as-received 10Ce-ZrO_2, 12Ce-ZrO_2 and α-alumina powders are reported in Figure 2.2. For 10Ce-ZrO_2 and 12Ce-ZrO_2, the peaks of both monoclinic and tetragonal zirconia phases have been indexed. A monoclinic volume fraction, V_m, of 76 % and 37% was determined respectively for 10Ce-ZrO_2 and 12Ce-ZrO_2 by applying the Toraya [4] equation (as detailed in the Appendix).
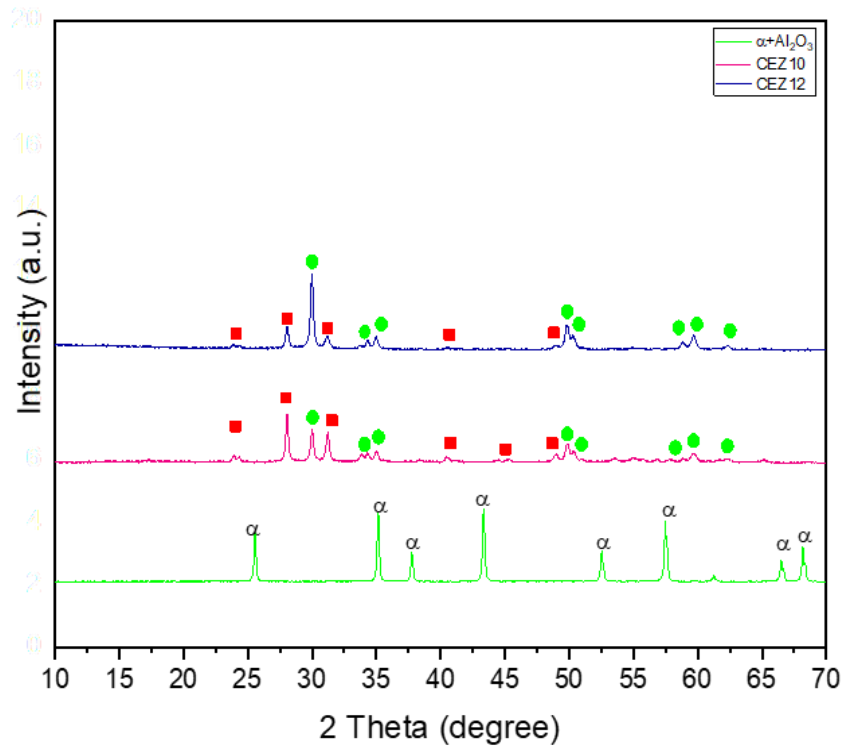
Figure 2.2 XRD patterns of as-received Al_2O_3, 10Ce-ZrO_2, 12Ce-ZrO_2. α=α-Al_2O_3;

● =t-ZrO_2; ■ = m-ZrO_2

(Monoclinic zirconia phase JCPDS n° 74-0815, tetragonal zirconia phase JCPDS n° 82-1398 and α-Al_2O_3 phase JCPDS n° 10-0173)

2.2 Dispersion of the zirconia-alumina powders through wet ball-milling technique

Slurries with high dispersibility and stability are challenging to obtain. The preparation of a slurry with suitable parameters such as solid loading and dispersant amount is critical. The rheology of the slurry is affected by the ball-milling time, as it can provide refined particle and homogeneous composition, in order to prevent interparticle agglomeration and allow the slurry to achieve uniform adsorption of

the dispersant. Because of that, the powder preparation process is a crucial step that will affect first of all the slurry behavior, and then the sintering and the mechanical properties of the printed parts. FESEM micrographs were collected (Figure 2.3) in order to observe the primary particle size, useful to be used as a reference in the process of deagglomeration.
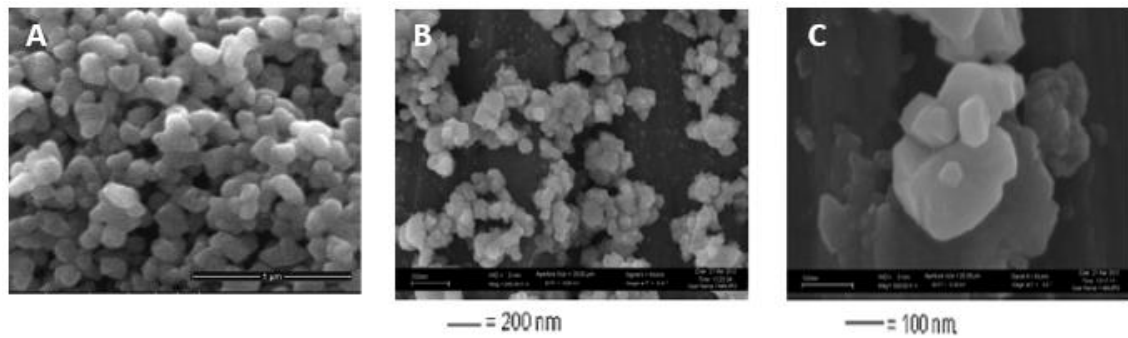
Figure 2.3 FESEM images of the as-received Al_2O_3 (a) and $10Ce-ZrO_2$ (b,c)

The grade of agglomeration was measured by laser granulometry (Mastersizer 3000, Malvern Panalytical, Worcestershire, UK). A significant difference in the raw powder's agglomeration can be appreciated. $10Ce-ZrO_2$ and $12Ce-ZrO_2$ powders are both characterized by a bimodal distribution, instead α-Al_2O_3 powder shows, at larger values, an almost monomodal distribution. Table 2.3 displays the particle size distribution of the as-received powders.
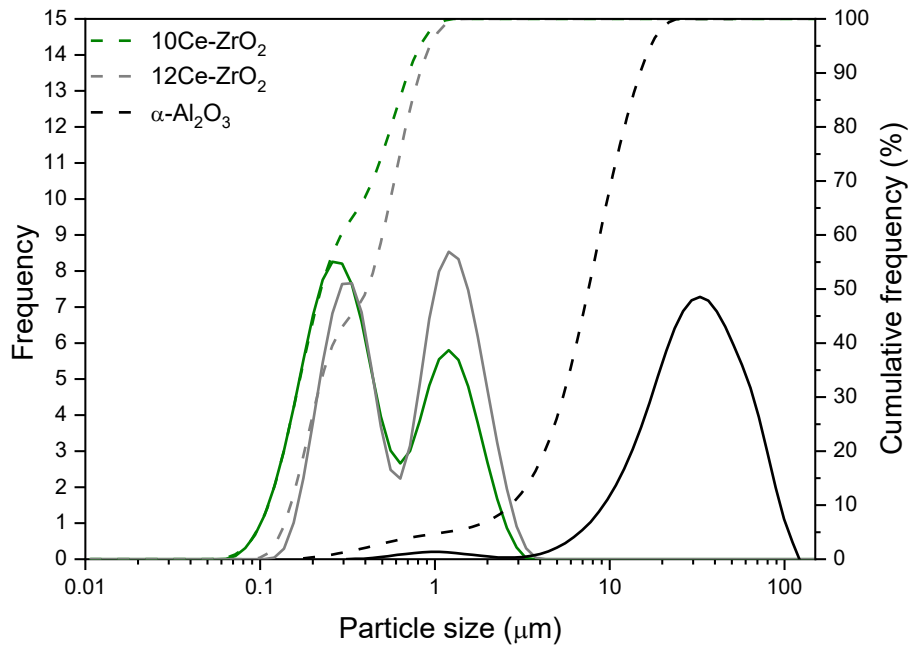
Figure 2.4: Particle size distribution of the as received raw powders: **(a)** $10Ce-ZrO_2$, $12Ce-ZrO_2$ and $\alpha-Al_2O_3$.

		D_{10} (µm)	D_{50} (µm)	D_{90} (µm)
As received	$10Ce-ZrO_2$	0.2	0.4	1.6
	$12Ce-ZrO_2$	0.3	0.8	1.9
	$\alpha-Al_2O_3$	8.2	28.3	62.1

Table 2.3: Particle size distribution of as-received $10Ce-ZrO_2$, $12Ce-ZrO_2$, $\alpha-Al_2O_3$ powders

2.2.1 Study of the appropriate dispersant

The dispersant added to the bi-phasic suspension was selected on the basis of several previous dispersion tests, checking the particle size distribution over time. Based on [5–7] data, the effect of four dispersants, namely Darvan C, Duramax D-3005, Disperbyk 103 and Disperbyk 180 were investigated. Technical information, given by the suppliers, are reported in tables 2.4, 2.5, 2.6 and 2.7, respectively.

- Darvan C is supplied by R.T. Vanderbilt Company, Inc., Norwalk, CT (USA) and it is an ammonium polymetacrylate. Its role is to improve particles dispersion by increasing the strength of the anionic charge on the particles surface, thus involving reciprocal repulsion.

ITEM	ANALYSIS RESULTS
Molecular weight	10000-16000 Da
Physical form	Liquid
Appearance	Clear to slightly opalescent amber fluid
Density at 25 °C	1.11 mg/mL
Percent solid	25
pH	7.5 to 9
Viscosity	75 cps
Solubility	Completely soluble in water system

Table 2.4: Technical data sheet of Vanderbilt Darvan C [8]

- Duramax D-3005 is supplied by Rohm and Haas Company, Philadelphia, PA (USA); it is an ammonium salt of a polyelectrolyte. The recommended amount of Duramax D-3005 to be added is a function of the powder specific surface area: for zirconia powders, the supplier suggests about 2.2 mg/m^2.

ITEM	ANALYSIS RESULTS
Molecular weight	2400 Da
Physical form	Liquid
Appearance	Pale yellow
Density at 25 °C	1.16 mg/mL
Percent solid	35
pH	6.0 to 7.0
Viscosity	<100 cps
Solubility	Completely soluble in water system

Table 2.5: Technical data sheet of Rohm and Haas Duramax D-3005 [9]

- DISPERBYK 103 is supplied by BYK Chemie Company, Wesel (Deutschland). It is a solution of a copolymer with filler affinic groups.

ITEM	ANALYSIS RESULTS
Physical form	Liquid
Appearance	Pale yellow
Density at 20 °C	1.06 g/mL
pH	6.0
Solubility	Completely soluble in water system

Table 2.6: Technical data sheet of DISPERBYK 103

- DISPERBYK 180 is supplied by BYK Chemie Company, Wesel (Deutschland). It is an alkylolammonium salt of a copolymer with acidic groups.

ITEM	ANALYSIS RESULTS
Physical form	Liquid

Appearance	Transparent
Density at 20 °C	1.07 g/mL
pH	5.0 to 7.0
Solubility	Completely soluble in water system

Table 2.7: Technical data sheet of DISPERBYK 180

The study of the dispersibility of the 10Ce-TZP, 12Ce-TZP, and α-Al_2O_3 powders, to obtain the final composition $ZA_{16}Ce_{11}$, was carried out with a solid loading of 10 wt%, by using absolute ethanol as the liquid medium, and a powder-to-spheres weight ratio of 1:10.

In order to identify the appropriate quantity of dispersant to add, different batches, with 1, 1.5, 2, 2.5, and 3 wt% of dispersant were prepared. Already with the addition of the lower amount of dispersant, a clear increase in the suspension flowability was visually observed. The granulometry was checked each two hours until when a monomodal and fine distribution was reached.

As depicted in figure 2.5, orange and light blue line, Darvan C and Disperbyk 180 were eliminated among the candidates because after 30 hours of ball milling, and with different amounts of dispersant, a good powder dispersion was not reached and a bimodal distribution of the particle was still observed. With Duramax D-3500 a good powder dispersion was reached with 1.5 wt% amount and after 18 hours of ball milling, a monomodal distribution was reached (figure 2.5, blue line).
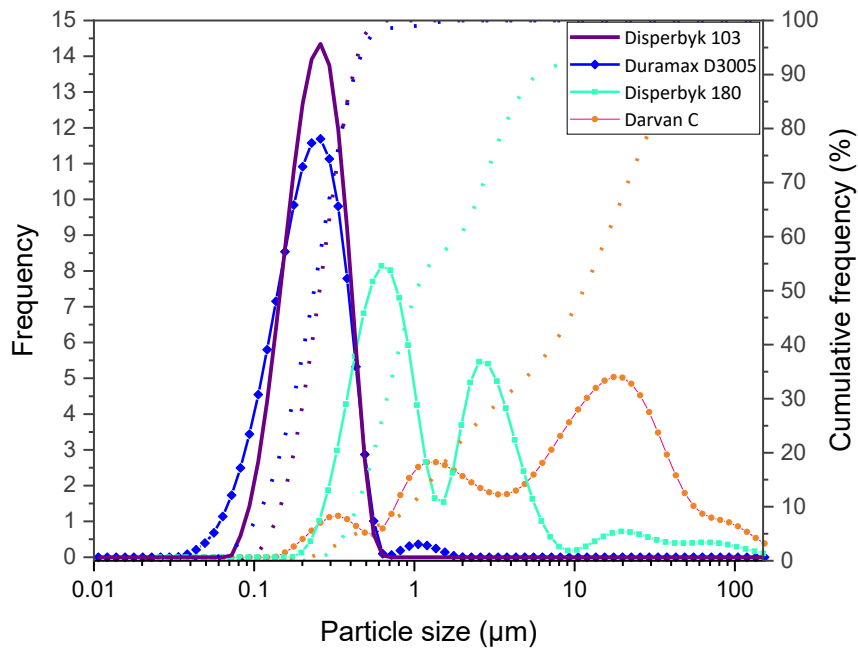
Figure 2.5 Particle size distribution of the $ZA_{16}Ce_{11}$ as a function of different dispersants. Cumulative frequency (dotted lines) and frequency (solid lines) are shown.

When Disperbyk 103 was added, the desirable conditions were reached with 2.5 wt% of dispersant and again after 18 hours of ball milling. Dispersants contain different anchoring head groups and carbon chain lengths; thus they can provide different degrees of steric stabilization. Of the four screened dispersants, DISPERBYK-103 is very effective in terms of dispersibility reached, probably due to the anchoring functional groups that can easily bind to the ZrO_2 particle surface and the end chains good affinity into polar media

As depicted in the time monitoring in figure 2.6, despite the agglomeration of the raw powders, after 18 hours of ball-milling, a monomodal and narrow distribution was achieved, with a mean particle size of 0.3 µm. In addition, as explained in detail in chapter 4 dedicated to the slurry preparation, the dispersant added in the mixture powder-acrylic resin was again Disperbyk 103. As a matter of compatibility, and

for the best results obtained, Disperbyk 103 was chosen as the definitive dispersant for the dispersion of powder. After drying, the composite powder was re-dispersed into ethanol, and the degree of agglomeration was again evaluated via laser granulometry. The particle size distribution of the dried powder was close to that of the dispersed alcoholic suspension, suggesting that during drying, no agglomerates or easy-to-redisperse agglomerates formed, and confirming the effectiveness of the adopted procedure.
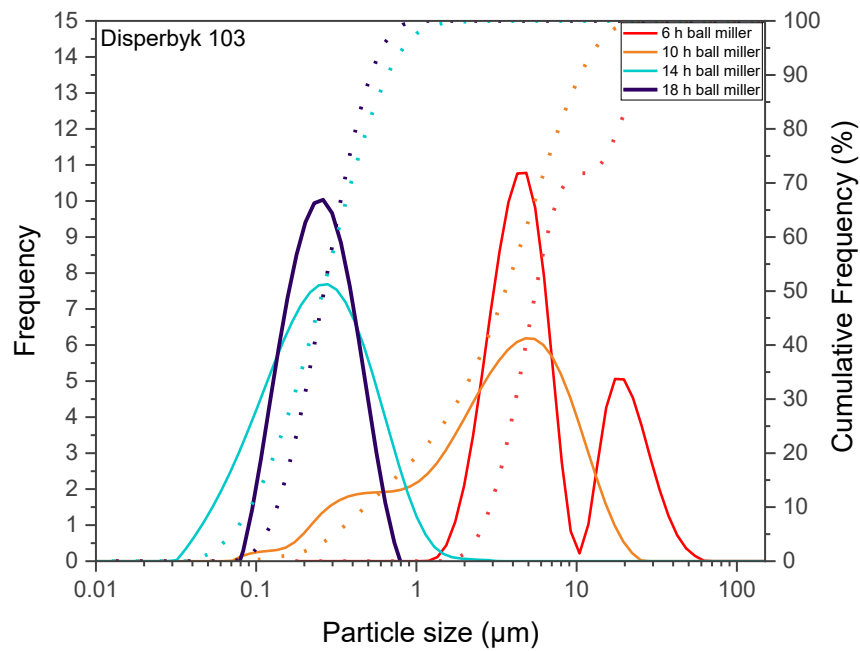
Figure 2.6 Particle size distribution of the *ZA$_{16}$Ce$_{11}$* dispersed with 2.5 wt% of Disperbyk 103 as a function of milling time. Cumulative frequency (dotted lines) and frequency (solid lines) are shown.

2.3 Characterization of *ZA₁₆Ce₁₁*

The XRD pattern of the *ZA₁₆Ce₁₁* powder is reported in figure 2.7 in which the peaks of α-Al$_2$O$_3$, monoclinic and tetragonal zirconia have been highlighted. Using the Toraya equation, a monoclinic volume fraction (Vm) of 82% was calculated, which is significantly a higher value than the single zirconia powders alone. Wang et al. [10] assessed that the t-m phase transition occurred due to stress induction.

The wet ball milling process provokes powder modifications; increases the activation energy inducing chemical reactions, thus, at the end of the process the powder shows excellent physical, chemical, and mechanical properties. By reducing the particle size the surface area increases, and the lattice strain too [11].
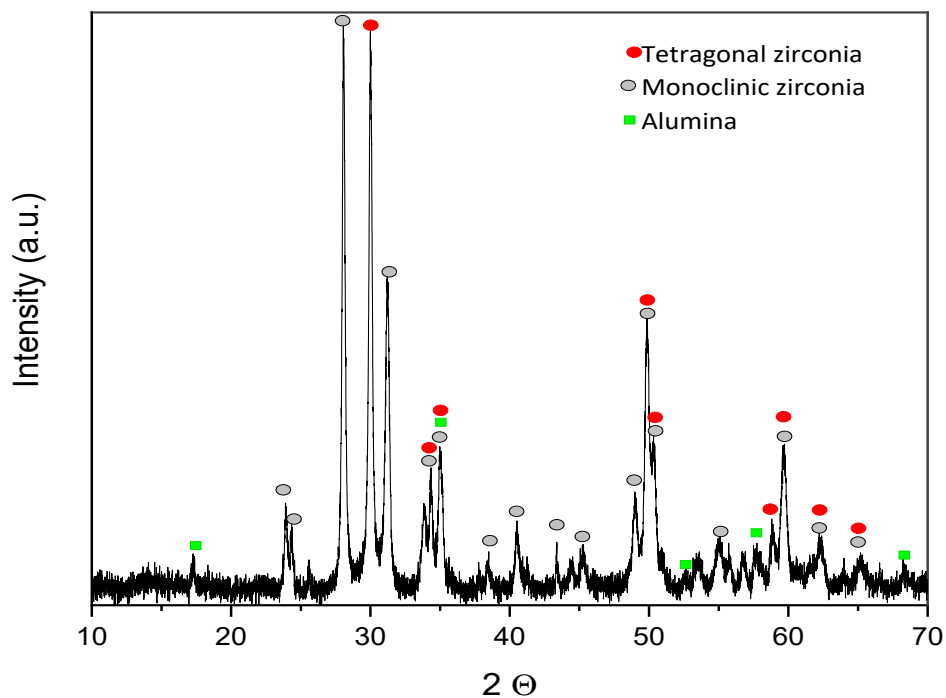
Figure 2.7 XRD pattern of the *ZA₁₆Ce₁₁* powder
(Monoclinic zirconia phase JCPDS n° 74-0815, tetragonal zirconia phase JCPDS n° 82-1398 and α-Al$_2$O$_3$ phase JCPDS n° 10-0173)

The composite powder was used to prepare, by conventional uniaxial pressing, reference samples to compare with printed samples (figure 2.8). The microstructure of the $ZA_{16}Ce_{11}$ was investigated with a Field Emission Electron Microscope (FESEM). The samples were sintered at 1500° C/1 h. The Al_2O_3 and Ce-ZrO_2 grains were determined with image analysis software (Java-based ImageJ software) through the linear intercept method according to the ASTM E112-13. An average of 200 grains of each phase were analyzed, mean values of 0.9 ± 0.3 μm and 0.3 ± 0.2 μm were found respectively for zirconia and alumina in the biphasic material.
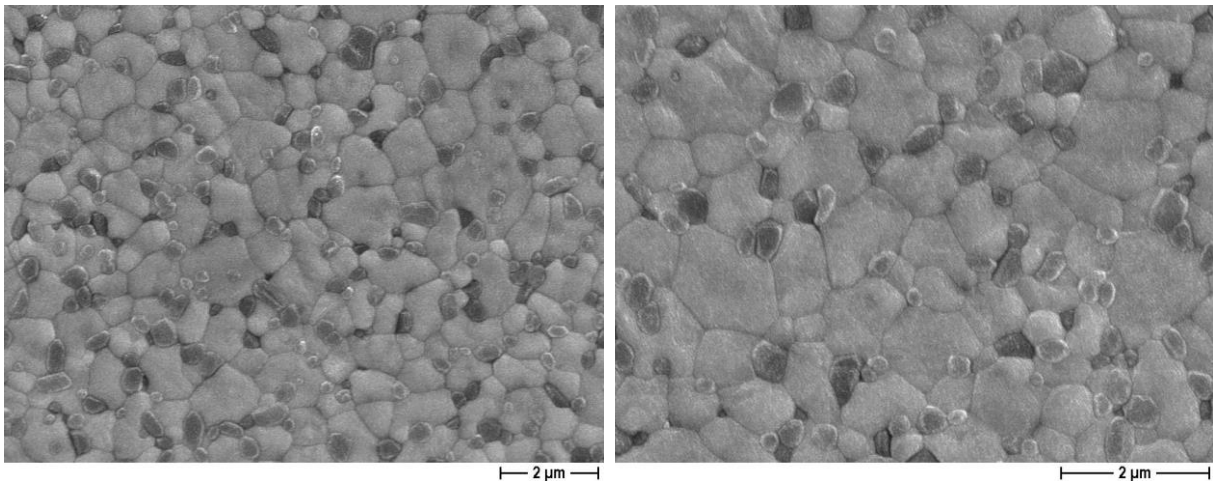
Figure 2.8 FESEM micrography of ZA16Ce11 powder pressed via uniaxial pressing
1500°C −1 h

2.4 Conclusions

In this chapter, the procedure to prepare $ZA_{16}Ce_{11}$ bi-phasic powder to add to the dispersant-acrylic resin mixture for the preparation of photocurable slurries was described. The material was successfully prepared.

The crucial elaboration steps, such as the raw powder dispersion and the effect of the dispersant were investigated and set up.

The addition of the commercial dispersant (Disperbyk-103) to the dispersed powder, allows to obtain good dispersibility and avoids particles' agglomeration.

Full control of the powder features is essential in order to tailor the final microstructures and obtain stable slurries as well as defects-free green and sintered parts, as will be shown in the following chapters.

References

1. Kitayama, M. & Pask, J. A. Formation and control of agglomerates in alumina powder. *Journal of the American Ceramic Society* **79**, 2003–2011 (1996).

2. https://www.dkkk.co.jp.

3. http://www.taimei-chem.co.jp.

4. Toraya, H., Yoshimura, M. & Somiya, S. Calibration Curve for Quantitative Analysis of the Monoclinic-Tetragonal ZrO2 System by X-Ray Diffraction. *J. Am. Ceram. Soc.* **67**, C-119-C-121 (1984).

5. Tang, F., Huang, X., Zhang, Y. & Guo, J. Effect of dispersants on surface chemical properties of nano-zirconia suspensions. *Ceram. Int.* **26**, **issue**, 93–97 (2000).

6. Fornabaio, M. Composites in the Alumina-Zirconia system: an engineering approach for an effective tailoring of microstructural features and performances. (Politecnico di Torino, 2014).

7. Hassanin, H. & Jiang, K. Optimized process for the fabrication of zirconia micro parts. *Microelectron. Eng.* **87**, 1617–1619 (2010).

8. http:/www.rtvanderbilt.com/TDS_DARVAN_C-N.

9. http://www.dow.com/products.

10. Wang, Z., Zhou, Z., Li, Y., Niu, W. & Ren, L. Effect of Grain-Boundary Segregation on Low-Temperature Degradation of Oral 3Y-Tzp Ceramics Co-Doped With Geo2 and Tio2. *J. Mech. Med. Biol.* **22**, 1–10 (2022).

11. Zhang, Y. *et al.* Ball milling assisted preparation of nano La–Y/ZrO2 powder ternary oxide system: Influence of doping amounts. *Ceram. Int.* **49**, 10375–10383 (2023).

Chapter 3

Elaboration and characterization of *ZA₈Sr₈Ce₁₁* powder

The third chapter is dedicated to the production of a tri-phasic composite powder. The second phases are formed through a surface modification of the matrix powder by inorganic precursors. The materials is designed, in fact, with secondary phases, in the shape of particles and platelets, able to enhance toughness and fracture strength. This composition was developed in the frame of a past European Project (*Advanced multifunctional zirconia ceramics for long-lasting implants – Longlife*, grant agreement n. 280741) in which the research group was involved and was used for the production of dental and spine implants via slip casting and uniaxial pressing methods [1-4]. Aim of this research is to demonstrate the feasibility to obtain printed parts, starting from the same composite powder. Therefore, in this chapter, the triphasic powder was added to a photocurable slurry, to be printed via digital light processing. The tri-phasic formulation consists in the 84 vol% ZrO_2 (11 mol% Ceria)/ 8 vol% Al_2O_3 / 8 vol% $SrAl_{12}O_{19}$ composition, hereafter referred as *ZA₈Sr₈Ce₁₁*. The adopted process for the elaboration of the tri-phasic powder is described in section 3.1. In section 3.2 the dispersion method is depicted. The last paragraph, 3.3, is dedicated to the characterization of *ZA₈Sr₈Ce₁₁* from the microstructural, crystallographic, and thermal point of view.

3.1 Elaboration of *ZA₈Sr₈Ce₁₁* tri-phasic powder

The main goal of this part of the thesis is to develop a DLP paste with $ZA_8Sr_8Ce_{11}$ powder in order to study the feasibility of an additive manufacturing process of such type of composite.

Because of its outstanding resistance to low-temperature degradation, high toughness, and biocompatibility, $ZA_8Sr_8Ce_{11}$ is a particularly promising candidate for the development of patient-specific biomedical implants [1].

In this material, in order to increase the mechanical properties of the ceramic matrix, $SrAl_{12}O_{19}$ was introduced. A characteristic feature of $SrAl_{12}O_{19}$ is an anisotropic growth, which generates elongated platelets and grains.

Vishista and Gnanam [2] proposed a model of microstructural development were $SrAl_{12}O_{19}$ nucleates at the interfaces between alumina and $SrO-Al_2O_3$ particles. The reaction proceeds by solid-state diffusion through the reactant phase [3].

The formation mechanism and growth of strontium hexaaluminate platelets during sintering was also studied by Kuzmin *et al.*[4].

In this work, the final tri-phasic composite $ZA_8Sr_8Ce_{11}$ contains:

-84 vol% ZrO_2 (11.0 mol% CeO_2) as matrix

-8 vol% Al_2O_3

-8 vol% $SrAl_{12}O_{19}$

It was obtained with the procedure described as follows.

ZrO_2 (10 mol% CeO_2), was selected as matrix material. In order to deagglomerate the starting powder and obtain a suitable grain size, the powder was dispersed in distilled water and ball-milled for 18 hours at pH 3 by adding few drops of hydrochloric acid. Zirconia spheres (2.0 mm in diameter, provided by Tosoh Corporation) were used as milling media with a powder to spheres weight ratio of 1:10 due to their excellent crushing strength and wear resistance. A laser-granulometer was used to check the degree of dispersion as a function of the milling time.

The precursor of cerium, ammonium cerium (IV) nitrate, was added to the zirconia slurry with the aim to increase the cerium content of the starting zirconia powders from 10 mol% (already present in the raw zirconia powder) to 11 mol%. To obtain α-Al_2O_3 and $SrAl_{12}O_{19}$ second and third phases, the inorganic precursors (namely, aluminium nitrate nonahydrate and strontium nitrate) were first dissolved in distilled water and then dropwise added into the ball-milled ceramic slurry.

ZrO_2 (10 mol% CeO_2) to aluminum nitrate weight ratio of 1:0.449 was employed to obtain in the final composite 8 vol% of Al_2O_3. A ZrO_2 (10 mol% CeO_2) to aluminum and strontium nitrate weight ratio of 1:0.389 and 1:0.018 respectively, were employed to obtain in the final composite 8 vol% of $SrAl_{12}O_{19}$. A ZrO_2 (10 mol% CeO_2) to cerium nitrate weight ratio 1:0.04 were employed to obtain 11 mol% CeO_2.

A dilution of the final mixture of 10 wt%, with respect to the solid content, was obtained by adding distilled water. In order to avoid hydroxide precipitation, few drops of diluted HCl were added to bring the pH of the suspension down to 3. Moreover, this final doped mixture was stirred for 2 hours to ensure high homogeneity.

To achieve a uniform distribution of the second and third phase, a rapid drying is preferred. Because of that, the suspension was spray dried, the high surface area and the small volume of the droplets allowed the atomized suspension's water to evaporate rapidly.

The inlet temperature of the spray drier was set at 160 °C, to induce the precipitation of the precursors onto the matrix powder surface (more details about the spray drying conditions are reported in the Appendix). After drying, the obtained product was submitted to a thermal treatment at 600° C first and then, 900° C to promote the second and third phase crystallization. The thermal treatment plays a role in the development of the final phase as well as in their distribution and size.

The powder was then re-dispersed with 3 wt%, with respect to the powder weight, of Duramax D-3005 [5] for 40 hours. The mixture was finally dried under magnetic stirring until when the water completely evaporated. To conclude, the dried powder

was ground and sieved by means of a sieve with apertures of 125 µm. The obtained powder was added to the acrylic resin for the preparation of the photocurable slurry. Figure 3.1 shows the typical flow chart of the adopted procedure.
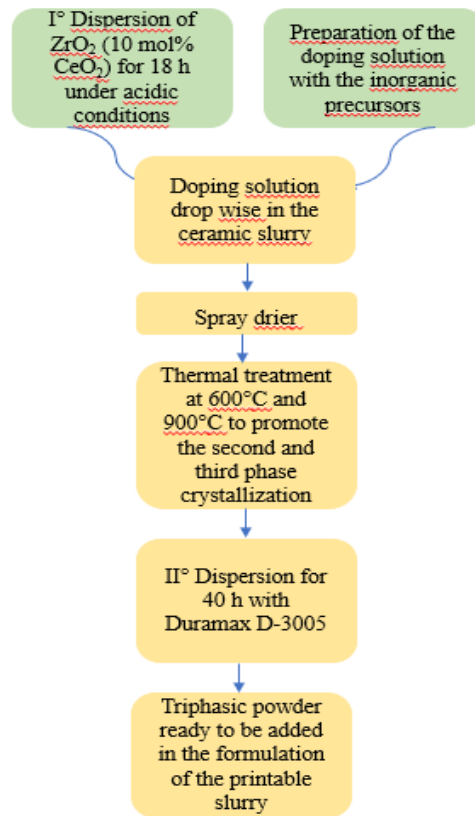
Figure 3.1 Flow chart of the adopted procedure for the tri-phasic composite powder elaboration

3.1.1 Characterization of the raw materials

$ZA_8Sr_8Ce_{11}$ tri-phasic powder was prepared with the ceria-stabilized zirconia (Ce-ZrO_2), containing 10 mol% of ceria, and supplied by Daiichi Kigenso (Kagaku Kogyo Co. ltd, Japan). Other information supplied by the producer [6] are collected in Table 3.1.

ZrO$_2$ (10 mol% Ceria) powder	
Item	Analysis results
ZrO$_2$ (+HfO$_2$)	86.39 wt%
CeO$_2$	13.37 wt%
Al$_2$O$_3$	0.23 wt%
Specific surface area	14.3 m^2/g
Particle size (D50)	0.5-1.0 μm
Green density	2.91 g/cm^3

Table 3.1 Technical data of Daiichi ZrO$_2$ (10 mol% CeO$_2$) powder

In order to obtain α-alumina as second phase aluminium nitrate nonahydrate supplied by *Sigma-Aldrich* was selected. The main features of the nitrate provided by the supplier [7] are reported in Table 3.2.

Aluminum nitrate nonahydrate	
Formula	Al (NO$_3$)$_3$·9H$_2$O
Molecular weight	375.13 g/mol
pH	2.5 – 3.5 at 50 g/L at 25 °C
Water solubility	41.9 g/L at 20 °C
Density	1.72 g/cm^3 at 20 °C
Purity	≥99.0%

Table 3.2 Technical data of aluminium nitrate nonahydrate

In order to increase the cerium content of the starting zirconia powders from 10 mol% (already present in the raw zirconia powder) to 11 mol%, ammonium cerium

(IV) nitrate supplied by *Sigma-Aldrich* was selected. The main features of the nitrate provided by the supplier [7] are reported in Table 3.3.

Ammonium cerium (IV) nitrate	
Formula	$(NH_4)_2[Ce(NO_3)_6]$
Molecular weight	548.22 g/mol
pH	0.61 at 111.11 g/L at 20 °C
Water solubility	919 g/L at 20 °C
Density	//
Color	orange
Purity	≥98.5%

Table 3.3 Technical data of ammonium cerium (IV) nitrate

In order to obtain $SrAl_{12}O_{19}$ as third phase, strontium nitrate supplied by *Sigma-Aldrich* was selected. The main features of the nitrate provided by the supplier [7] are reported in Table 3.4.

Strontium nitrate	
Formula	$Sr(NO_3)_2$
Molecular weight	211.63 g/mol
pH	6.7 at 10 g/L at 20 °C
Water solubility	660 g/L at 20 °C
Density	//
Color	white
Purity	≥99.0%

Table 3.4 Technical data of strontium nitrate

3.2 Dispersion of the powder through wet ball-milling technique

The $ZA_8Sr_8Ce_{11}$ was successfully developed by INSA Lyon and Politecnico di Torino in the frame of the European project Longlife and led to patenting of the material and the process of obtaining it. The final goal of this research was to obtain the powder in the same condition and print it by DLP-stereolithography.

The concentration and the ionic strength influence the stability of the ceramic powder slurry. The pH of the suspension should be also carefully controlled to obtain a stable suspension and to avoid flocculation, heterogeneity and precipitation of secondary phases. For the elaboration process of $ZA_8Sr_8Ce_{11}$, it was chosen to work under acidic conditions (pH = 3) for two reasons. First of all, under these conditions the hydroxide precipitation can be avoided, and then the elaboration process of the powder involves the use of acidic salts (nitrates). The acidic conditions were reached by adding diluted hydrochloric acid to the ZrO_2 (10 mol% CeO_2 dispersed powder). The natural pH of the aqueous suspension was decreased from 6.5 to 3. As soon as the hydrochloric acid was added, a relevant increase of the suspension flowability was visually observed. A good dispersion of the powder was reached after 18 hours of ball-milling under acidic conditions. In Table 3.5, the D10, D50, and D90 values of the particle size distribution are collected.

In order to induce the decomposition of the by-products, the doped powders were treated at 600 °C / 1 hour at the heating rate of 10 °C/min. A second pre-treatment was carried out at 900 °C/ 1 hour at the heating rate of 10 °C/min to induce the crystallization of the second phases on the zirconia particle surface [8,9].

The calcinated powder was re-dispersed in distilled water with 3 wt% (as respect to the powder weight) of Duramax D-3005. The suspension was then ball-milled for 40 h.

As depicted in figure 3.2, the particle size distribution of ZrO_2 (10% mol% CeO_2) after 18 h of ball milling is close to that of the $ZA_8Sr_8Ce_{11}$ after the two thermal treatments at 600° C and 900° C and the second dispersion for 40 hours, showing the effectiveness of the adopted procedure.
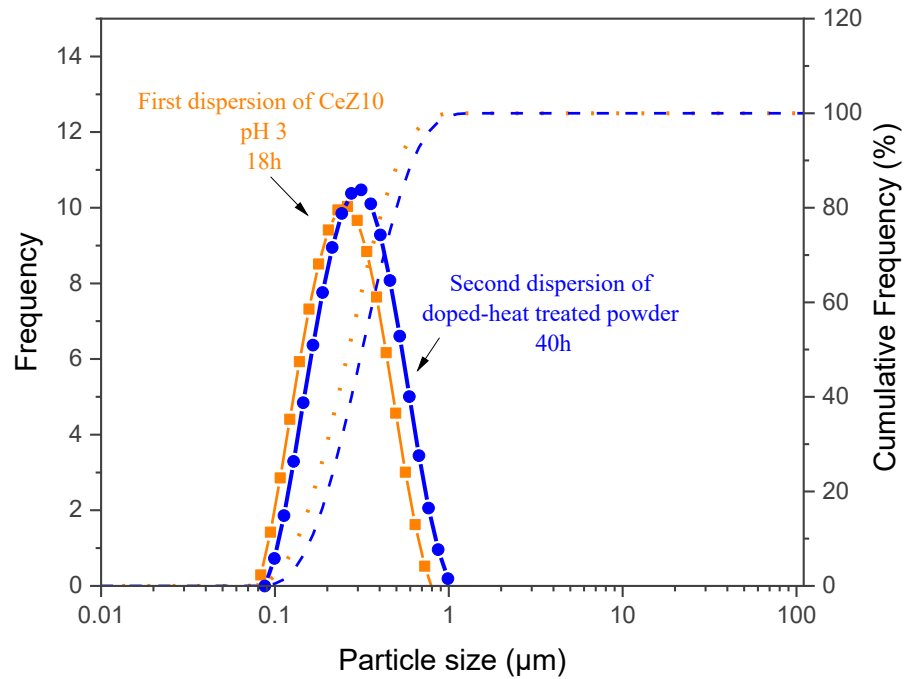
Figure 3.2 Particle size distribution of ZrO_2 (10 mol% CeO_2) after 18 h of ball milling under acidic condition (solid orange line) and of $ZA_8Sr_8Ce_{11}$ after the thermal treatments and 40 h of dispersion with Duramax D-3005 (solid blue line)

	D_{10} (µm)	D_{50} (µm)	D_{90} (µm)
ZrO_2 (10 mol% CeO_2) **18 h ball milled**	0.19	0.42	0.85
$ZA_8Sr_8Ce_{11}$ **40 h ball milled**	0.22	0.49	0.89

Table 3.5: Particle size (μm) corresponding to 10% (D10), 50% (D50) and 90% (D90) of the cumulative distribution of ZrO_2 (10 mol% CeO_2) after 18 h of ball miller under acidic condition, as well as of the dispersed *ZA8Sr8Ce11* composite powder.

3.3 Characterization of *ZA8Sr8Ce11* tri-phasic powder

The thermal behaviour of the as-spray dried powder was investigated by Thermogravimetric-Differential Thermal Analysis (TG-DTA) in a previous study [10]. A 30% of mass loss was recorded due to the precursors' decomposition which was totally accomplished at ~ 500 °C. A broad peak at 1200 °C, imputable to α-alumina or aluminates crystallization, can be observed in figure 3.3. On the basis of the TGA, in order to induce the decomposition of the by-products, the doped powders were treated at 600 °C / 1 hour at the heating rate of 10 °C/min.
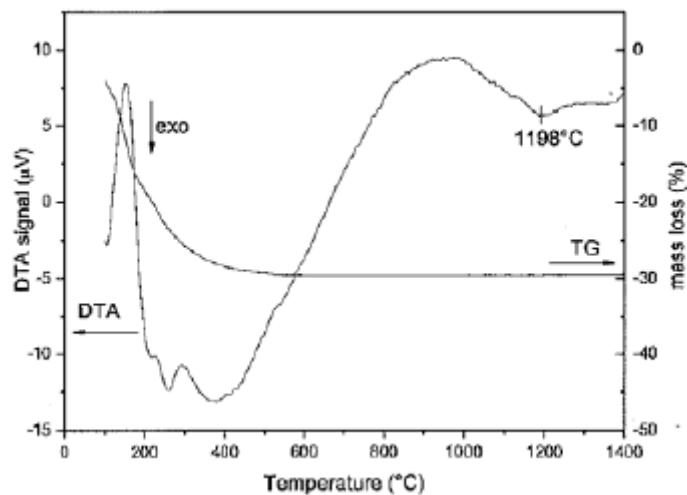
Figure 3.3 TGA-DTA curves of the *ZA8Sr8Ce11* powder after spray-drier [10]

The $ZA_8Sr_8Ce_{11}$ powder was characterized from a compositional point of view. In figure 3.4 the XRD patterns of $ZA_8Sr_8Ce_{11}$ pressed powder via uniaxial pressing sintered at 1500° C/1 hour (solid blue line), the $ZA_8Sr_8Ce_{11}$ powder at the end of the doping procedure, ground and sieved < 125 µm (solid orange line) and the XRD pattern of CeZ10 as received, the parent powder (solid red line) are reported.

Tetragonal and monoclinic zirconia phase-related peaks were found in the XRD investigations of the material. The intensity of the peaks corresponding to the Al_2O_3 and $SrAl_{12}O_{19}$ phases is very low but still observable in comparison to the zirconia peaks because of the difference in the absorption coefficients and the low second/third phase volume concentration (8 vol%).

A monoclinic volume fraction, Vm, of 76%, 34% and 2% was determined respectively for ZrO_2 (10 mol% CeO_2), $ZA_8Sr_8Ce_{11}$ powder and $ZA_8Sr_8Ce_{11}$ pressed and sintered by applying the Toraya [11] equation (as detailed in the Appendix).
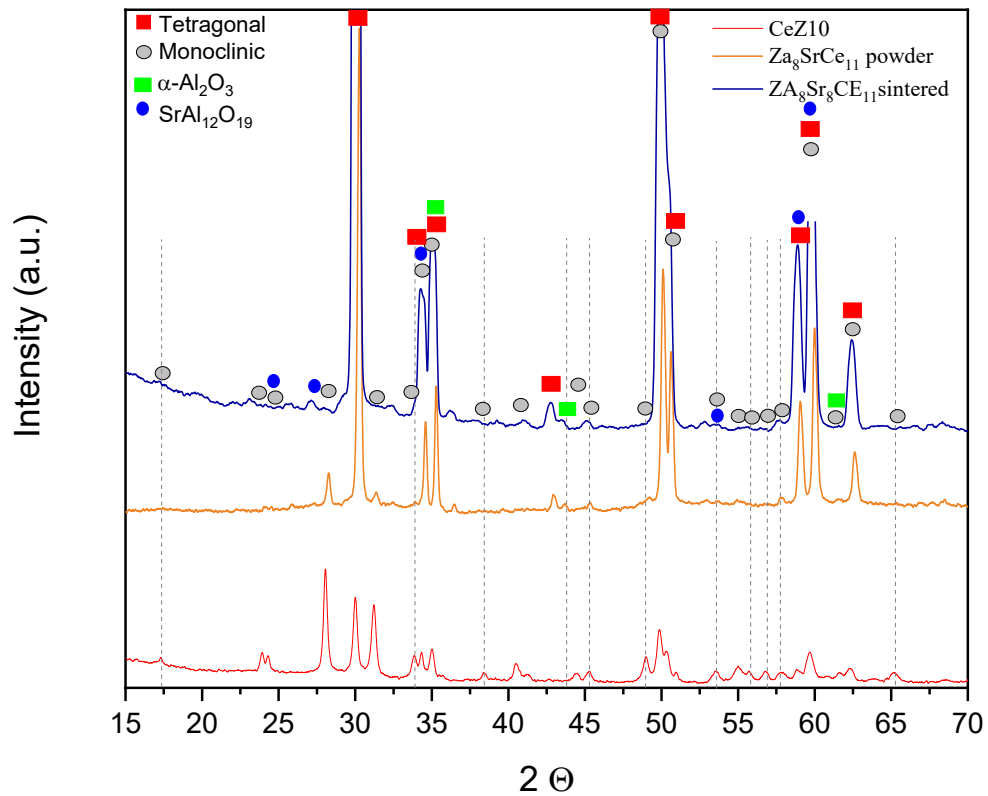
Figure 3.4 XRD pattern of the *ZA$_8$Sr$_8$Ce$_{11}$* powder
(Monoclinic zirconia phase JCPDS n° 74-0815, tetragonal zirconia phase JCPDS n° 82-1398, α-Al$_2$O$_3$ phase JCPDS n° 10-0173, SrAl$_{12}$O$_{19}$ phase JCPDS n°80-1195)

The composite powder was used to prepare, by conventional CIP, reference samples to compare with printed samples. The microstructure of the *ZA8Sr8Ce11* was investigated with a FESEM. The samples were sintered at 1500° C/1 h. The ImageJ software was used to study the grains' size through the linear intercept method according to the ASTM E112-13. An average of 200 grains of each phase were analyzed and mean values 0.8±0.3 μm and 0.3±0.1 μm were found, respectively for zirconia and alumina in the triphasic material. The mean length of the aluminates calculated was 0.86 ± 0.2 with an aspect ratio of 6 ± 2.

As can be observed in figure 3.5, the final microstructure contains strontium aluminate elongated grains surrounded by zirconia and alumina equiaxed grains.
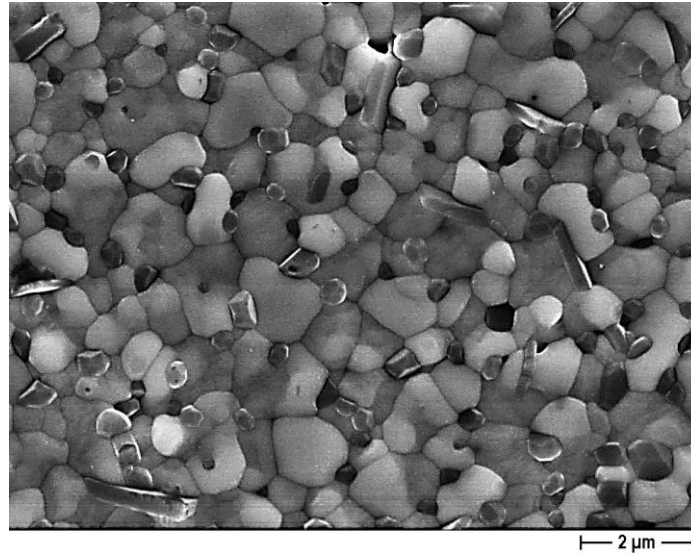
Figure 3.5 FESEM micrograph of *ZA₈Sr₈Ce₁₁* powder produced via uniaxial pressing and sintered at 1500°C/1h

In order to highlight the different phases, in previous studies [10] the STEM technique High-angle annular dark-field imaging (HAADF) was performed on the *ZA₈Sr₈Ce₁₁* sintered samples. In figure 3.6, brighter regular-shaped zirconia grains, the darker elongated strontium, and the dark rounded alumina grains can be immediately identified.
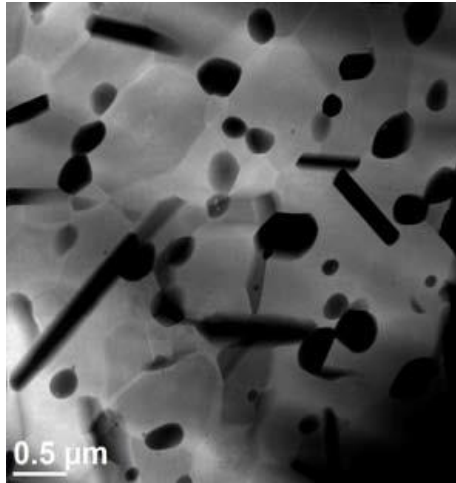
Figure 3.6 High-angle annular dark-field imager of *ZA₈Sr₈Ce₁₁* sintered samples [10]

3.4 Conclusions

In this chapter the tri-phasic *ZA$_8$Sr$_8$Ce$_{11}$* was successfully prepared. The preparation process of the zirconia-based material is described. Composite powders were developed through a surface coating route.

Equiaxial α-Al$_2$O$_3$ and elongated particles of SrAl$_{12}$O$_{19}$, were selected as second phases. The use of elongated morphologies allows increasing the toughness by additional bridging/crack-deflection mechanisms. The essential elaboration processes, including the dispersion of the raw powders and the thermal behaviour of the powder, were examined.

As will be detailed in the following chapter, complete control over the powder's characteristics is necessary to customize the final microstructures of the printed bodies.

References

1. Fournier, S. *et al.* Ceria-stabilized zirconia-based composites printed by stereolithography: Impact of the processing method on the ductile behaviour and its transformation features. *J. Eur. Ceram. Soc.* (2022). doi:10.1016/j.jeurceramsoc.2022.11.006

2. Vishista, K. & Gnanam, F. D. Microstructural development of SrAl12O19 in alumina-strontia composites. *J. Eur. Ceram. Soc.* **29**, 77–83 (2009).

3. Vishista, K. & Gnanam, F. D. Effect of strontia on the densification and mechanical properties of sol-gel alumina. *Ceram. Int.* **32**, 917–922 (2006).

4. Kuzmin, R. *et al.* Strontium hexaaluminate formation in alumina and alumina–zirconia matrixes. *Ceram. Int.* **47**, 6854–6859 (2021).

5. Fornabaio, M. *et al.* Zirconia-based composites for biomedical applications: Role of second phases on composition, microstructure and zirconia transformability. *J. Eur. Ceram. Soc.* **35**, 4039–4049 (2015).

6. https://www.dkkk.co.jp.

7. https:www.sigmaaldrich.com/.

8. Palmero, P. *et al.* Towards long lasting zirconia-based composites for dental implants: Part I: Innovative synthesis, microstructural characterization and invitro stability. *Biomaterials* **50**, 38–46 (2015).

9. Palmero, P., Naglieri, V., Chevalier, J., Fantozzi, G. & Montanaro, L. Alumina-based nanocomposites obtained by doping with inorganic salt solutions: Application to immiscible and reactive systems. *J. Eur. Ceram. Soc.* **29**, 59–66 (2009).

10. Fornabaio, M. Composites in the Alumina-Zirconia system: an engineering approach for an effective tailoring of microstructural features and performances. (Politecnico di Torino, 2014).

11. Toraya, H., Yoshimura, M. & Somiya, S. Calibration Curve for Quantitative

Analysis of the Monoclinic-Tetragonal ZrO2 System by X-Ray Diffraction.
J. Am. Ceram. Soc. **67**, C-119-C-121 (1984).

Chapter 4

Elaboration and characterization of photocurable slurries

Digital Light Processing (DLP) stereolithography has been used to fabricate ceramic components. The slurry containing ceramic particles dispersed in a photocurable resin is exposed to UV light of a certain wavelength so that it solidifies to form a ceramic green body. To produce dense ceramic pieces, additional heat debinding and sintering processes are necessary. This chapter is dedicated to the development and characterization of slurries printable with DLP-stereolithography. In the first section, 4.1, the elaboration of $ZA_{16}Ce_{11}$ slurries is described. In sections 4.2 and 4.3, the slurries, without and after the addition of the dispersant, are characterized from the point of view of the rheology: the influence of the solid

loading and of the amount of dispersant on the slurry behaviour and the characteristics of the printed parts is studied. In section 4.4 the printing process parameters, and their correlations, were studied through the Principal Components Analysis (PCA). In the last section, 4.5, as a further development of the work, the $Ce_{11}ZA_8Sr_8$ ceramic was printed and sintered parts characterized too.

4.1 Process to produce the photocurable ceramic suspension

In this paragraph, the elaboration of $ZA_{16}Ce_{11}$ (powder preparation details in chapter 2) and $ZA_8Sr_8Ce_{11}$ (powder preparation details in chapter 3) polymer-ceramic slurries is described. As previously discussed, the bi- and tri-phasic powders are elaborated through two different procedures. Once the powders are obtained, the slurries are then developed by following the same preparation method. Since the triphasic powder is developed through a long and quite complex preparation procedure, the preliminary study was carried out on the biphasic material.

The commercial resin supplied by Admatec (Admatec Europe BV, The Netherlands) was used in combination with a commercial dispersant (Disperbyk-103, BYK Chemie, Germany), used over the years to produce zirconia parts [1–3], added to improve the stability and to enhance slurries solid loading.

For the preparation of the slurries, the ceramic powder was sieved under 125 μm and added to the acrylic photocurable resin. First, mechanical stirring was performed for 15 minutes to mix the dispersant within the resin. Then, for another 30 minutes, while constantly mixing to prevent the formation of agglomerates, the powder was gradually added to this mixture. In the end, the produced slurry was ground in a planetary mill for three hours at 350 rpm using agate jars containing agate spheres (d = 10 mm) (Fritsch Pulverisette, Fritsch GmbH, Germany). The slurry was then de-aired under vacuum for an hour. The flow chart of the process is

reported in Figure 4.1. As previously explained in chapter 1, the slurry, for an evenly distribution on the tape, should be less viscous than 3000 mPa.s at the operative shear rate (5000 mPa.s according to other researchers [4]) and have high solid loading which commonly increases the viscosity. In our system, the operative shear rate, which corresponds to the shear rate applied by the doctor blade during the spreading of the slurry, was equal to 160 s^{-1}. A dispersant should be employed to manage particle–particle interactions and maintain a low viscosity if the solid loading of the ceramic powder is more than 35 vol%, to stabilize and prevent sedimentation of the slurry. The paste must have a shear thinning behaviour to prevent its spontaneous flow and to achieve a uniform layer under the action of the doctor blade [5–7]. As a preliminary study, dispersant-free slurries were prepared at 50.0 to 62.5 wt% solid loadings. A second set of slurries was prepared with the addition of 1.0–4.0 wt% dispersant (respect to the dry powder) that allowed to achieve solid loadings in the range of 65 to 80 wt%. Finally, the slurries were printed, and the as-obtained samples were submitted to the debinding and sintering treatments. Bars suitable for mechanical characterization were then produced. More details about the operative conditions of the most important steps are supplied in the following.
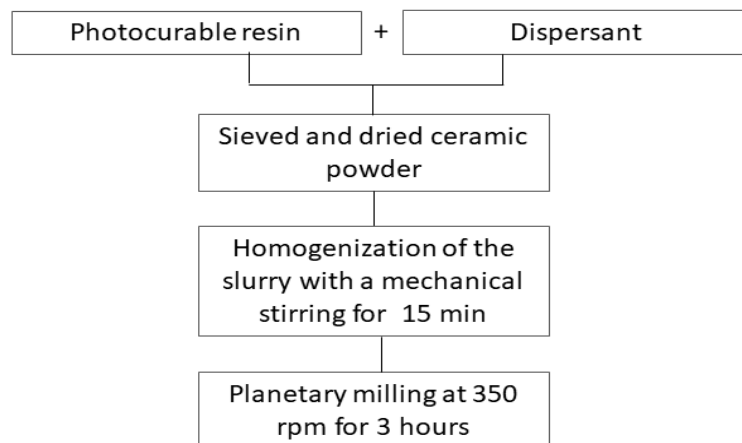
Fig 4.1 Flow chart of the slurry preparation process to develop *ZA$_{16}$Ce$_{11}$* and *ZA$_8$Sr$_8$Ce$_{11}$* printable slurries

4.1.1 The acrylic resin

A commercially available photocurable resin (Admatec Europe BV, The Netherlands) constituted by a photoinitiator, diphenyl (2,4,6,trimethylbenzoyl) phosphine oxide, and acrylates was chosen as the organic binder to connect ceramic particles.

The resin used is a mixture of one or more acrylate-based oligomers and monomers, and a photoinitiator that can form radicals to initiate the photopolymerization reaction of acrylates at a radiation wavelength of 405 nm [8]. Detailed information about the formulation of the resin has not been revealed to the public yet but, since the manufacturer suggested the water debinding of the printed parts, it was assumed the presence of a water-soluble polymer inside the resin that, according to the following TGA-DTA analysis, might be identified with a certain confidence as PEG. The PEG's dissolution is a gradual process in two stages. Firstly, water molecules slowly diffuse into the binder producing a swollen gel. Afterward, the gel slowly disintegrates into a solution if the room temperature is above the melting point of PEG. The melting point varies with the density of the polymer, from 5.8 °C for the PEG400 to 62.1 °C for the PEG 6000 [9] [10].

The addition of ceramic powders reduces the resin flowability and resolution during printing owing to light scattering. The 2D layers of a resin are exposed to UV irradiation and solidify on top of each other to create a 3D object. UV irradiation supplies the energy needed to induce the photopolymerization process, and creates a strongly cross-linked polymer [11].

4.1.2 Characterization of the acrylic resin

In order to study the thermal decomposition of solely the acrylic resin (no ceramic powder charge), few drops of the resin were exposed to the UV light and polymerized. One part was submitted to the water debinding step while the other directly underwent the TG-DTA analyses up to 1050 °C (heating rate 10 °C/min, static air) as shown in Figure 4.2.
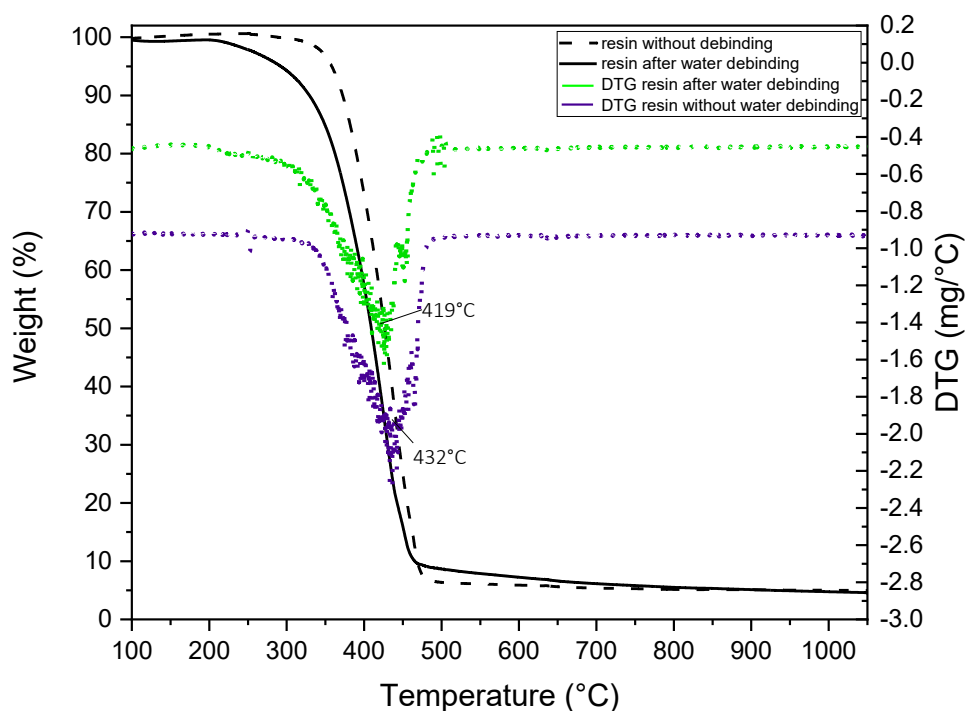
Figure 4.2 TGA curves and its derivative of the polymerized acrylic resin without water debinding and after water debinding

In figure 4.2, the thermogravimetric curves (TG and DTG) show a single mass loss stage for both resins (with/without water debinding) related to acrylic group degradation [12]. The complete polymer degradation was recorded at temperatures above 505 °C. The weight of the resin after water debinding started decreasing at

221 °C. Instead, for the polymerized resin, the weight loss started at 300 °C. For the resin after water debinding the decomposition rate was higher between 221 °C and 470 °C, with a maximum peak at 419 °C. For the polymerized resin the decomposition rate was higher between 300 °C and 490 °C, with a maximum peak at 432 °C. The shift of the decomposition starting temperature of the two resins could be attributed to the presence of the water-soluble components (in the resin without water debinding) that in the polymerized resin are still present and lead to an advance of ~ 80 °C of the decomposition temperature.

According to the TGA-DTG curves, the decomposition of organic matter was vigorous, at this stage the printed parts are highly exposed to the formation of defects attributable to the gas released during the burnout of the binder, as well as excessive thermal stress. If the thermal removal process of porogens and binders is not slow enough the outgassing pressure will cause the bursting or cracking of the parts. The corresponding solid residue can be attributed to ash and inorganic additives [12].
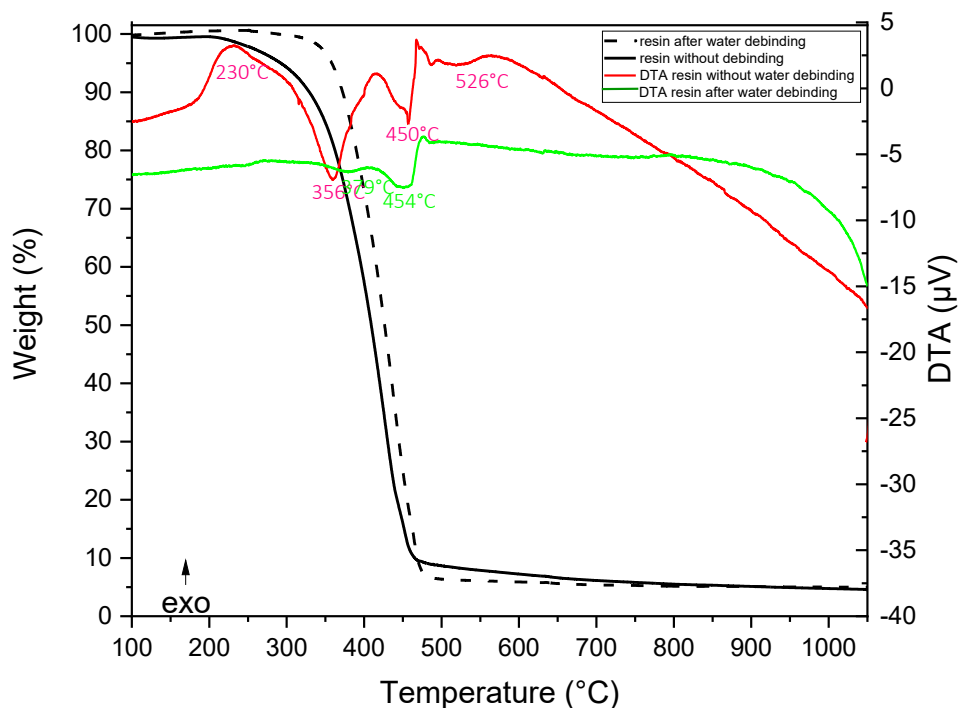
Figure 4.3 TGA and DTA curves of the polymerized resin without water debiding and after water debinding

As shown in figure 4.3, the DTA curve of the resin without water debinding shows one exothermic peak at 230 °C, at this temperature the unpolymerized resin starts to decompose. There are also three other endothermic peaks at 356 °C, 450, and 526 °C. The resin after water debinding shows two endothermic peaks at 379 °C and 454 °C. The measurements were done with a heating rate of 10 °C/ min under static air.

Consequently, in order to decompose the organic matter avoiding the generation of critical internal stresses, the failure and cracking of the green structure, a controlled and slow thermal debinding must be performed before sintering the ceramic skeleton.

In figure 4.4 ATR (attenuated total reflection) Fourier transformed-infrared (FT-IR) spectra were recorded between 4000 and 525 cm^{-1} with a resolution of 4 cm^{-1} and 32 scans per sample using a Thermo Scientific Nicolet iS50 FTIR Spectrometer (Milano, Italy) coupled with the ATR accessory (Smart iTX).

Only in the liquid resin spectrum, the broad band at 3486 cm^{-1} corresponds to the hydroxyl stretching vibration. The bands at 2962-2964 cm^{-1} are probably due O-CH$_3$ and C-H stretching and their intensity decreases from liquid resin to the cured ones. Strong bands at about 2871 cm^{-1}, due to the CH$_2$ stretching vibrations, respectively, are visible in all spectra. The bands at about 1730 cm^{-1} correspond to the C=O stretching of the ester group, and the bands at 1635 cm^{-1} to the C=C of the acrylate group. These bands have a decreasing intensity moving from liquid resin to the cured one before and after the water debinding treatment. The bands at 1273-1257 cm^{-1} belong to the -C-O-C- stretching mode of the ether group and its intensity increased after curing. The bands at 1186 and 1104 cm^{-1} correspond to the C–O group. All these bands are characteristic of acrylate groups. In the cured resin spectrum and in the cured resin after water debonding the band at 1635 cm^{-1}, corresponding to the C=C double bond of the acrylate group, showed also a reduction of the intensity, due to the reticulation process [12].
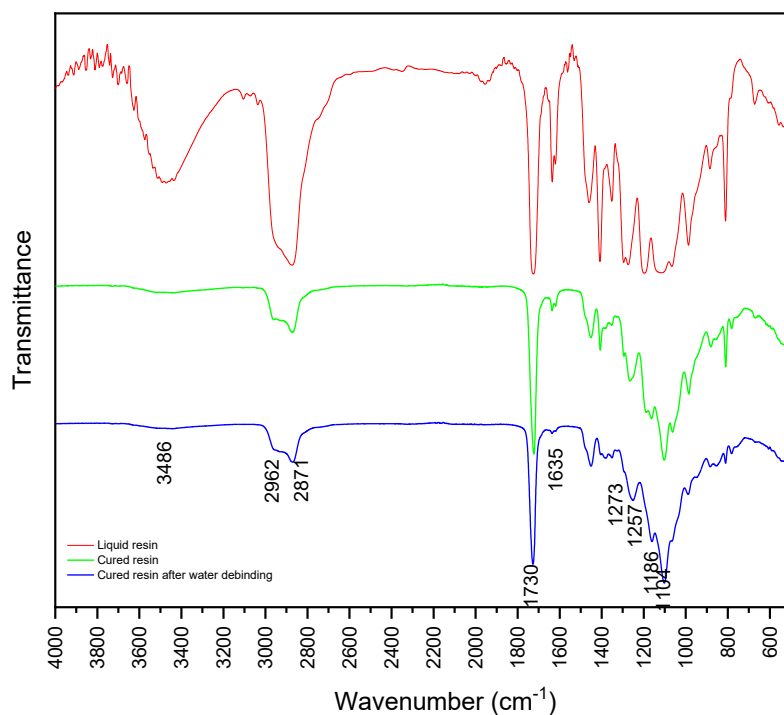
Fig. 4.4 ATR-FTIR spectra of the liquid resin (red spectrum), the cured resin (green spectrum), and the cured resin after water debinding (blue spectrum)

4.2 Preliminary set-up of the slurries

The optimization of the solid loading is a crucial point of the stereolithographic process. High viscosity and poor flowability lead to the formation of agglomerates and bubbles that evolve, during the sintering, into severe defects as pores and intralayer delamination thus acting as crack-initiating agents, lowering the flexural strength [13].

This preliminary experimental trial was carried out to analyse the potentialities of slurries to be printable and to understand how the dispersant (explained in deep in the next section) can affect the slurry's behaviour.

Dispersant-free slurries, composed only by sieved and dried ceramic powder and by the commercial acrylic resin, were prepared in a range of solid loadings from 50.0 wt% to 62.5 wt%. The rheological behaviour of the slurries can be observed in figure 4.5. As shown in the graph, as the solid loading increases the shear viscosity also increases, attributable to an ever-greater fraction of ceramic particles that causes higher friction.

All the investigated slurries presented a shear-thinning behaviour, with a decrease of the viscosity as the shear rate increases due to the alignment of the structural units in the flow direction under an applied stress improving the system's flow [14]. At the operative shear rate of 160 s^{-1} a shear viscosity of 0.6, 0.7, 1.3 and 2.2 Pa·s, was recorded for the slurries at 50, 55, 60 and 62.5 wt% solid loadings, respectively.
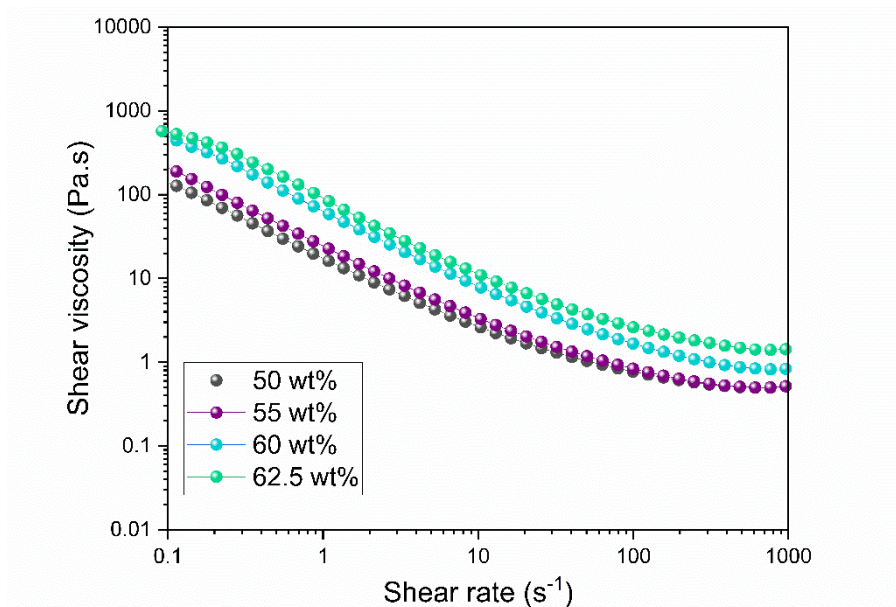
Figure 4.5 Rheological measurements of $ZA_{16}Ce_{11}$ slurries from 50 to 62.5 wt% of solid loading

The curing depth behaviour of the photosensitive slurries under different exposure times and a fixed exposure intensity of 31.96 mW/cm^2 was measured using a caliper (figure 4.6).

The increase of the solid loading led to a decrease of the curing depth for a fixed period of exposure time. Furthermore, a reasonable increase of the curing depth with a longer exposure duration can be observed even if this happens at an increasingly lower rate with the increase of solid loading. There are two potential causes for the reduced UV penetration with higher solid loadings. The higher amounts of ceramic particles generate a higher light scattering, due to a refractive index mismatch between the acrylic resin and the ceramic fraction [15,16].

The curing depth is also affected by the presence of ceria since the zirconia is doped with ceria, because it is a strong UV-absorbing material. Powders doped with 11 mol% of ceria strongly absorb in UV-C (100–280 nm) and UV-B (280–315 nm) light regions. The absorption of particles decreases in the UV-A (315–400 nm) region [15].
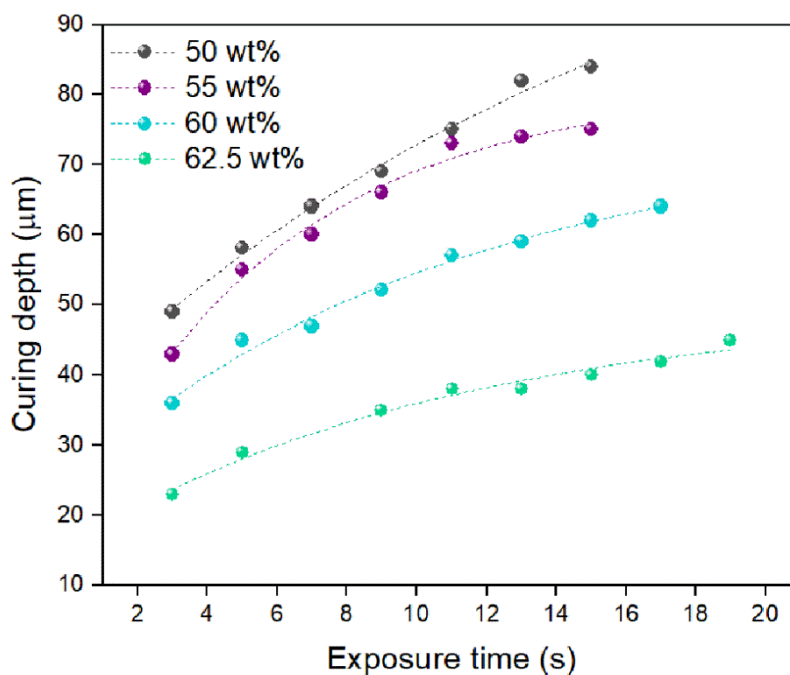
Figure 4.6 Curing depths of the slurries at 50.0–62.5 wt% solid loading as a function of the exposure time.

In order to obtain a high accuracy of the printed parts, a compromise between parameters such as exposure time, exposure power and solid loading must be found. Too much long-time exposure or a too high led power may cause over exposure and, as a consequence, overgrowth and poor sample precision.

The light scattering effect and overgrowth were described by Gerald [17]; in figure 4.7 the dark yellow square represents the exposed region, whilst the light-yellow area shows the unwanted exposed zone due to the scattering. Such overgrowth can be minimized or eliminated by adjusting the exposure strategy.
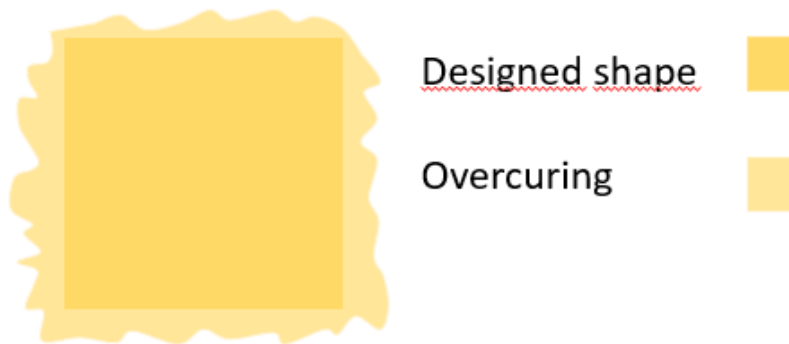
Figure 4.7 Illustration of the overexposure effect in a cured sample due to the UV light scattering, after Gerald [17]

In Fig. 4.8, the printed patterns results of the overgrowth study are depicted. As expected, the overgrowth decreases markedly with decreasing exposure dose since there is less energy to induce scattering. This led to a significant increase in printing precision [18]. In figure 4.8 A and C, the overgrowth produces the polymerization of the slurry out of the original square provoking inaccurate edges. In contrast, in figure 4.8 B and D, the optimal printing parameters, such as exposure time and led

power, led to the polymerization only of the wanted shape with net and regular edges.
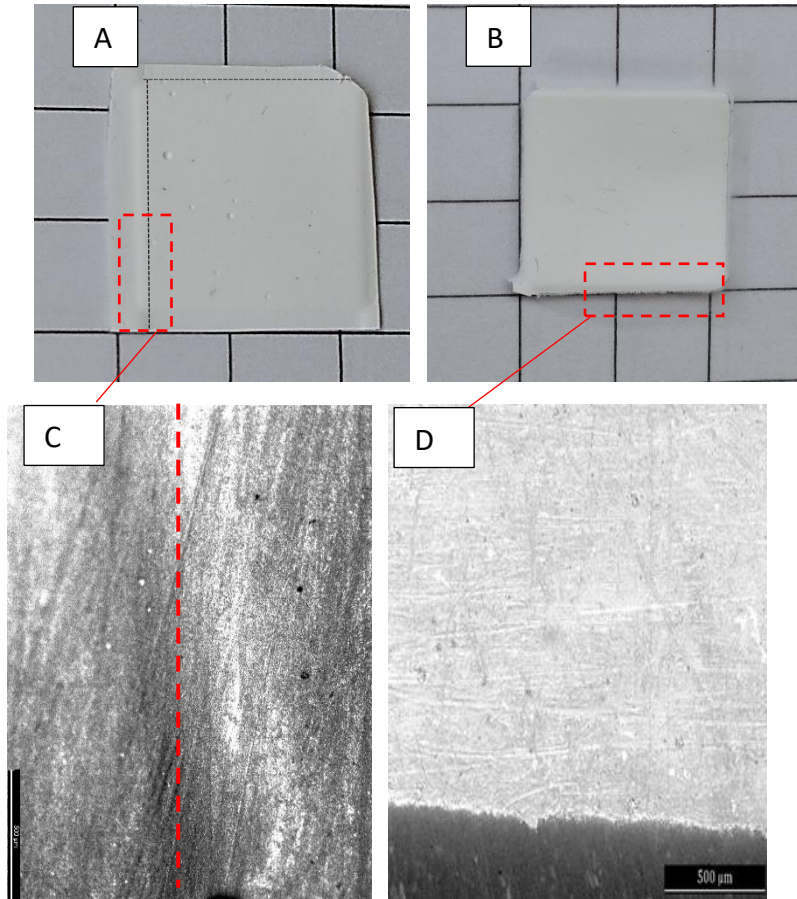
Figure 4.8 Single layers printed with decreasing exposure times

Low solid loading slurries are favourable due to the low viscosity and the contained scattering phenomenon, while a high solid loading allows to reach higher green densities, to reduce the shrinkage during drying and the thermal debinding step and allows to obtain a higher fired density of the sintered parts. The printed parts from 50.0 wt% to 62.5 wt% were sintered in air atmosphere at 1500 °C and 1550 °C (figure 4.9). The increment of the sintering temperature from 1500 °C to 1550 °C allows the increase of the fired density of 2–3%. The same trend can be observed

at both sintering temperatures, a progressive increase of the density up to 60 wt%, followed by a drop at 62.5 wt%. Maximum density values for the 60 wt% slurry were 95.1 ± 1.1 % and 97.6 ± 0.9% at 1500 ◦C/ 1 h and 1550 ◦C/1 h, respectively. The density was calculated by the buoyancy method (Archimedes' density) and all the values are related to the material's theoretical density.
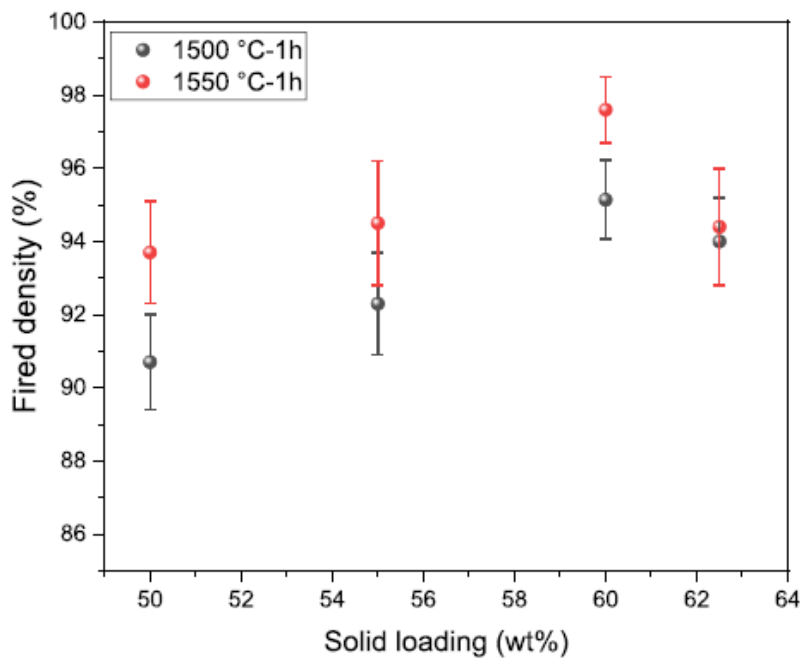
Fig. 4.9 Fired density of the sintered parts at different solid loadings

FESEM micrographs of the 60 wt% solid loading, sintered at 1500 °C/1 h (a) and 1550 °C (b), are shown in figure 4.10. At 1500 °C, at lower magnification (figure 4.10 A) several flaws are present, probably due to the not optimal flowability of the slurry, to the resin burn-out, and to the insufficient necking between ceramic particles [13].

With the increasing of sintering temperature up to 1550 °C/1 h (figure 4.10 C), the density also increases. Concerning the microstructures, they were very homogeneous for both temperatures, and at higher magnification, an even

distribution of alumina and zirconia grains can be appreciated. Due to the printing flaws and the not complete densification, the recipes were further optimized by the addition of the commercial dispersant (Disperbyk-103), which permitted a substantial increase of the solid loading, as described in chapter 4.4
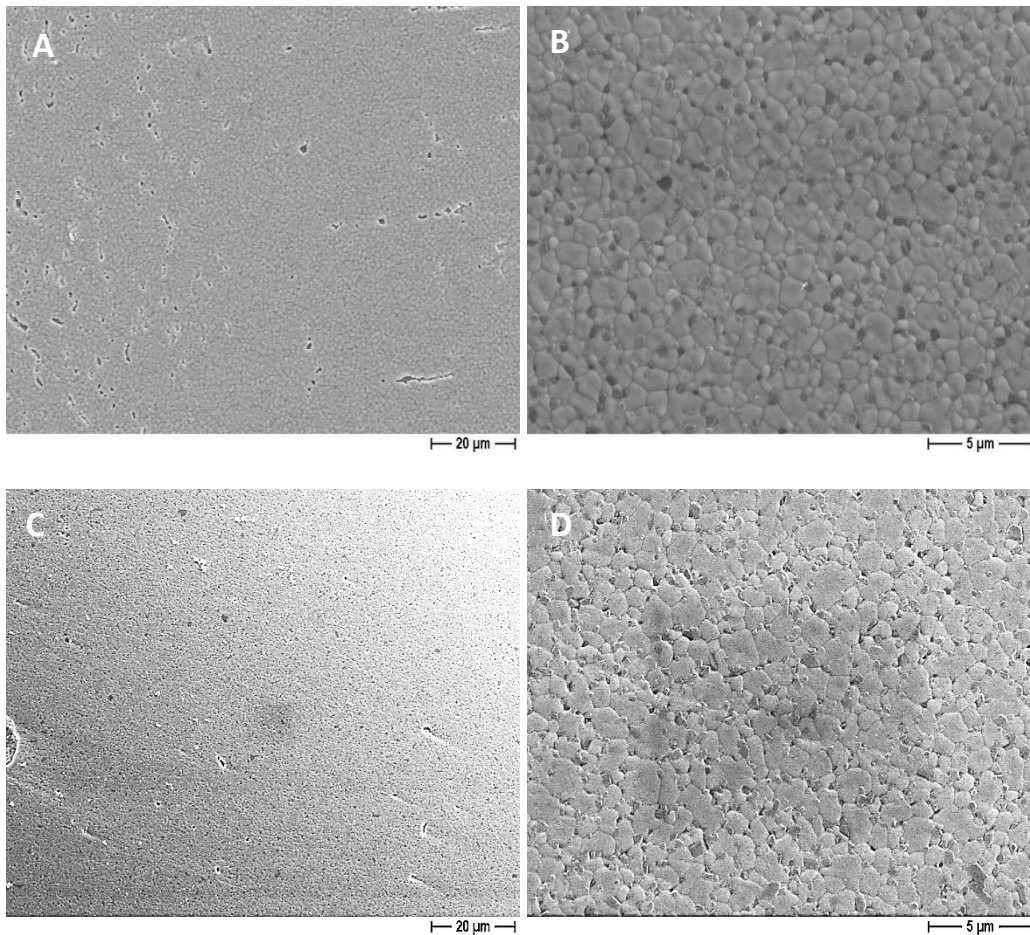
Figure 4.10 FESEM micrographs of the sample at 60 wt% of solid loading sintered at 1500 °C (a-b) and 1550 °C (c-d)

4.3 Optimization of the slurry by the addition of the dispersant

The dispersant has a great influence on the rheological behaviour of the slurry. Low solid loading slurries show ideal flowability and printability, characteristics that tend to decrease as the solid load increases. Consequently, the bubbles in suspension cannot escape easily from suspension with a high solid loading and lead to the formation of pores. For this reason, it is extremely important to increase the solid loading by keeping favourable fluidity and printability; this can be realized by the addition of a dispersant. Generally, the dispersant has a hydrophilic polar group that can interact with the surface of the ceramic particle and a hydrophobic end chain to provide steric stabilization in the nonpolar media [19].

The UV-curable slurry was prepared by mixing the acrylic monomers and the dispersant first, followed by incremental addition of the ceramic powder into the organic media until the desired solid loading level was reached.

In order to select the more suited dispersant, three commercial products presenting good miscibility with the photosensitive resin were tested: Disperbyk-103, Disperbyk-111, and Disperbyk-180. In table 4.1, the main features of the three dispersants are reported.

Dispersant	Chemical Description	Density (g/cm^3)
Disperbyk-103	solution of a copolymer with filler affinic groups	1.06 (20 °C)
Disperbyk-111	copolymer with acidic groups	1.16 (20 °C)
Disperbyk-180	alkylolammonium salt of a copolymer with acidic groups	1.075 (20 °C)

Table 4.1 Data of the selected dispersants

To study the dispersion behaviour of the ceramic particles in highly loaded slurries, zeta potential measurements are generally utilized. However, the zeta potential value of zirconia powder in photocurable resin is generally low, which makes it difficult to evaluate the dispersion effect of low polar resin-based suspensions [20]. For this reason, the effect of the dispersant was studied from the rheological point of view. A rotational rheometer (Kinexus Pro+, Netzsch Gerätebau GmbH, Selb, Germany) equipped with stainless steel parallel plates (20 mm diameter) with a 1 mm gap between plates by applying shear rates of $0.1–1000$ s^{-1} at 25 ∘C was used. All dispersants were added to suspensions at the concentration of 73 wt% (with respect to powder mass). Not all the dispersants can successfully decrease the viscosity because of different anchoring headgroups and carbon chain lengths [19].

As can be observed in Figure 4.11, Disperbyk-103 is the most effective in reducing viscosity. The slurry with Disperbyk-180 and Disperbyk-111 exhibit a lower dispersibility, thus they were eliminated among the candidates also for this reason. It is probably related to the anchoring functional groups of the dispersant that efficiently bond to the surface of the ceramic particles and to their end chains which shows affinity to low-polar media. All the slurries, tested from 0.1 to 1000 s^{-1} of shear rate, showed the typical shear-thinning behaviour, necessary in the stereolithography process because it allows the efficient spread of slurry and thus a homogeneous green microstructure can be obtained.
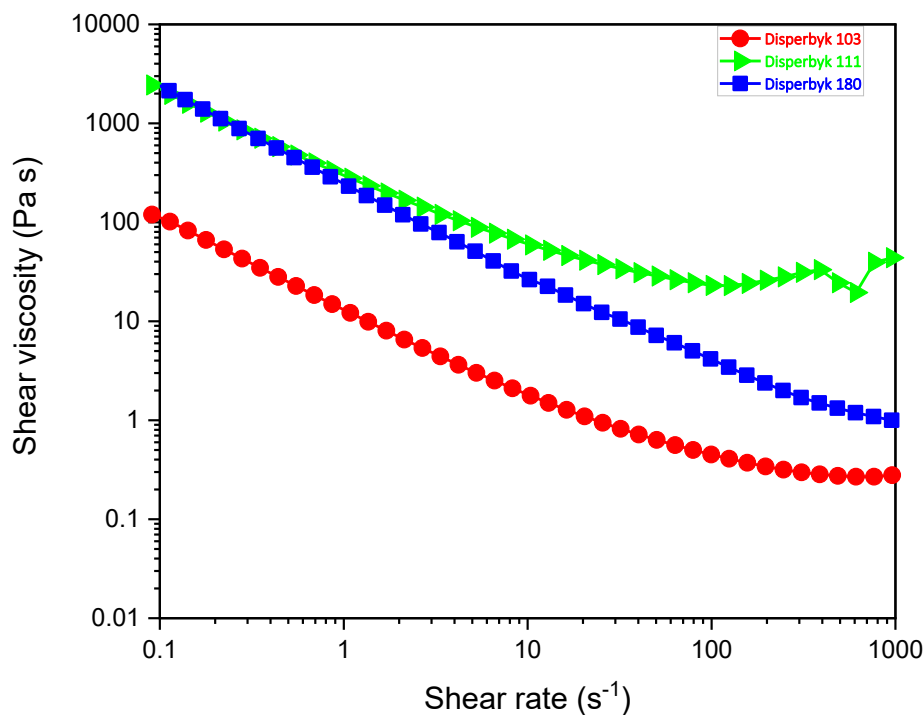
Figure 4.11 Shear viscosity versus shear rate on a log-log scale for the 73 wt% slurries with different dispersants (2.5 wt% with regard to the mass of the powder)

4.3.1 Optimization of the dispersant concentration

Once assessed that Disperbyk-103 was the most suitable dispersant for the slurries' preparation, it was possible to increase the solid loading from 62.5 wt% (maximum obtainable with only powder and resin) up to 80 wt%. Precisely, the solid loadings 65, 68, 70, 73, 78 and 80 wt% were investigated. The quantity of dispersant was optimized for each slurry on the base of rheological studies. The amount of dispersant was added in the range of 1.0 - 4.0 wt% with respect to the weight of the dry powder.

As it can be noticed in figure 4.13, for the 73 and 78 wt% formulations, when the amount of dispersant increased, the viscosity of the slurry progressively decreased until a minimum and then the viscosity rose again.

If the dispersant concentration is too low, the beneficial effect to the powder is too weak to counterbalance the van der Waals attractive forces and to avoid the collision of particles due to Brownian motion, as a result an unstable slurry is obtained [21]. On the contrary, when the optimum dose exceeds, a free fraction of dispersant, that cannot anchor to the ceramic particles surfaces, is available and starts to form tangles between the particles, known as bridging flocculation, causing an unwanted increase of the viscosity [19,22]. Figure 4.13 displays the rheological behaviours of the slurries at the highest solid loading (73-80 wt%), where the phenomena are more evident, with different concentrations of dispersant. As can be seen, all the slurries showed a shear-thinning behaviour, as already observed for the slurries without the dispersant (section 4.3). For each formulation, the fraction of Disperbyk-103 that led to the lowest viscosity, corresponding to the ideal condition of dispersion below Griffith's [6] recommended upper limit of 3000 mPa·s at the working shear rate of the 3D printer, 160 s^{-1} for the Admaflex 130, was determined (table 4.2).

As can be seen in the table the amount of dispersant necessary to obtain the suitable flowability of the slurry was 3.5% for the 73 wt% and 2.5% for the 78 wt%. This is a rather unexpected outcome and somewhat counterintuitive. The main difference between these two formulations was the change in the resin's lot. The supplier has stated that he has provided the same resin but actually, in the changement from a lot to a new another, a slight difference in the viscosity results was registered. A TGA analysis was performed on the two polymerized resins, but no significant differences were obtained. Another parameter that may have affected could be the humidity or the temperature of the laboratory.
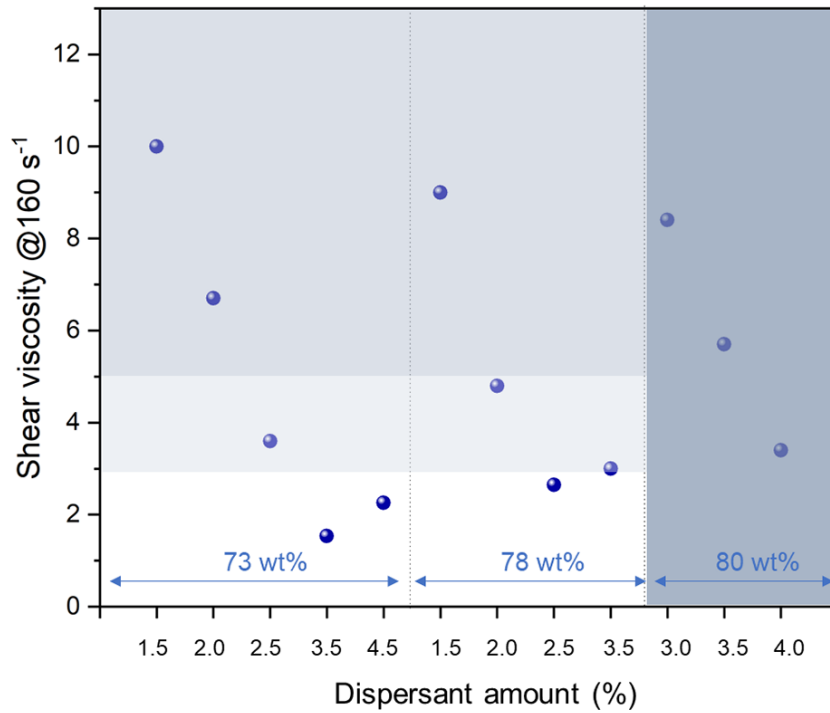
Figure 4.12: Shear viscosity variation as a function of the quantity of dispersant for the 73 to 80 wt% slurries. Light and medium grey areas indicate the limit of printability of 3 [6] and 5 Pa·s [4] according to the literature, while the dark grey area denotes the non-printability range due to a too low curing depth

Solid loading (wt%)	Solid loading (vol%)	Dispersant (wt%)
65	28.5	1.0
68	28.9	1.0
70	30.1	1.0
73	33.4	3.5
78	39.6	2.5
80	45.5	4.0

Table 4.2 Composition of the slurries with the lowest viscosity at 160 s^{-1}

4.3.2 Relation between solid loading and curing depth

The cure depth of slurries from 68 wt% to 80 wt% were measured at a fixed energy dose of 31.96 mW/cm^2 to determine the curing depth dependence on ceramic volume fraction. The polymerization is affected by the kinetics of the monomer polymerization and by the UV scattering due to the refraction index difference between the ceramic particles and the monomer [23].

In figure 4.13 the curing depth behaviour of the slurries added with Disperbyk-103 in function of the exposure time is depicted.

It can be seen that, as previously observed in the slurries without dispersant in figure 4.6, the curing depth increases as the exposure time increases and decreases as the solid loading increases. Because of the difference in refractive indices between the resin and the ceramic particles, the higher solid load causes more light scattering and less UV penetration. In addition, it is necessary to take into account also the slurries' considerable UV-absorbance due to the 11 mol% ceria content [15].

The presence of ceria in the $Ce_{11}ZA_{16}$ composite doesn't allow the achievement of thick single layers. However, with the increase of the exposure time and the led power, it is possible to slightly increase the thickness, but to the detriment of the resolution. Furthermore, in order to avoid delamination, an important issue of the stereolithographic technique, the UV light must penetrate the exposed layer and reach the layer above to permit the sealing and bonding between the layers. For this reason, the penetration capability of the UV must be 1.5 times deeper than the set thickness of each layer as recommended by the Admatec specialized technicians. As can be observed in figure 4.13, the red lines indicate the suitable thickness of the layer that might be set based on the UV penetration capability. For example, with a UV penetration ability of 37.5 µm, a single layer thickness of 25 µm could be set, thicker sizes must be avoided because they would lead to the formation of defects that would jeopardise the integrity of the sintered parts. The formulation 80 wt%+4% Disperbyk-103, due to the high solid loading, makes the deep

photopolymerization above 30 µm difficult, thus it was not printed and was considered as the upper limit (see Fig. 4.12). For the formulations at lower solid loadings (from 68 wt% to 78 wt%), even if the curing depth and resolution were at acceptable values, the slurries were evaluated also with respect to the density and the microstructure.
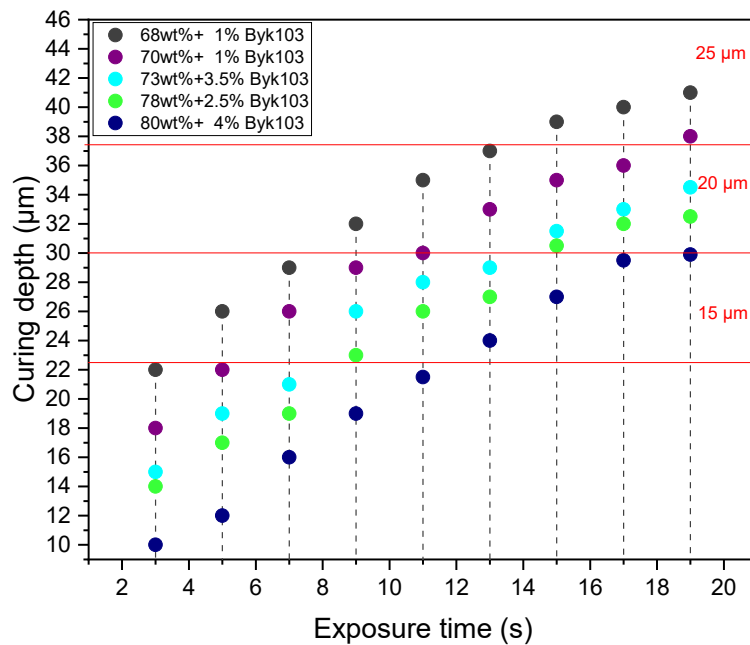
Figure 4.13 Curing depths (at 31.96 mW/cm^2) at increasing exposure time for the 68.0 - 80.0 wt% slurries

As shown in figure 4.14 (A) the density of the green parts increases as the solid loading increases. After sintering, in figure 4.14 (B) the Archimedes' density (%TD), measured by the buoyancy method, raises significantly from 65 to 70 wt%. From 70 wt% to 78 wt% the density continues to increase until almost complete densification.

The sintering was performed at 1500 °C and 1550 °C for 1 h.

The density of the samples printed with the slurries at 65 wt% and 70 wt% showed a noticeable increase when the sintering temperature increased from 1500 °C to 1550 °C. On the contrary, the density of the samples made with the 73–78 wt% slurries raised of only 1–2%. The highest densification was achieved with the slurry with a solid loading of 78 wt%, with values of 98.3% and 99.4% after firing at 1500 °C/1 h and 1550 °C/1 h, respectively. For some samples the standar deviation is not negligable, this is a criticity of the work, the printing job must be further refined in order to reduce this gap
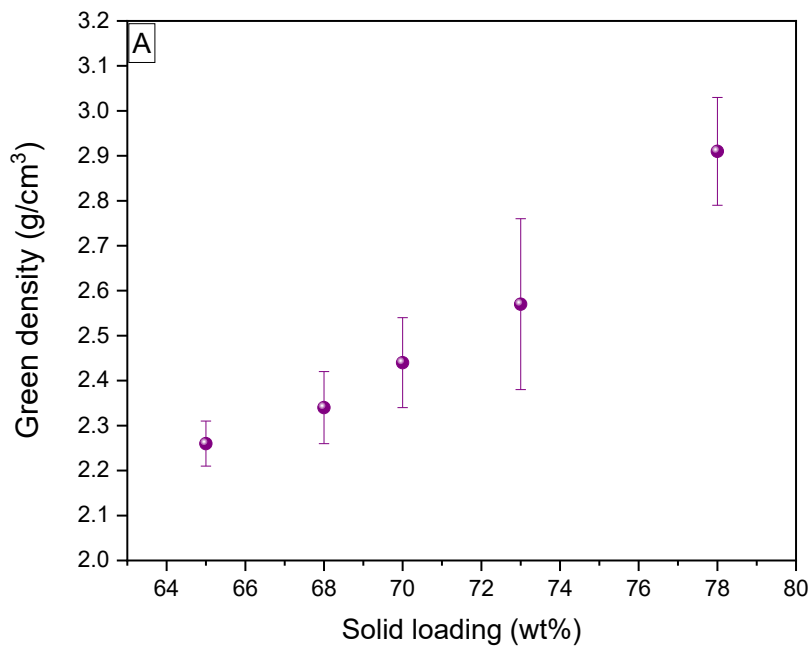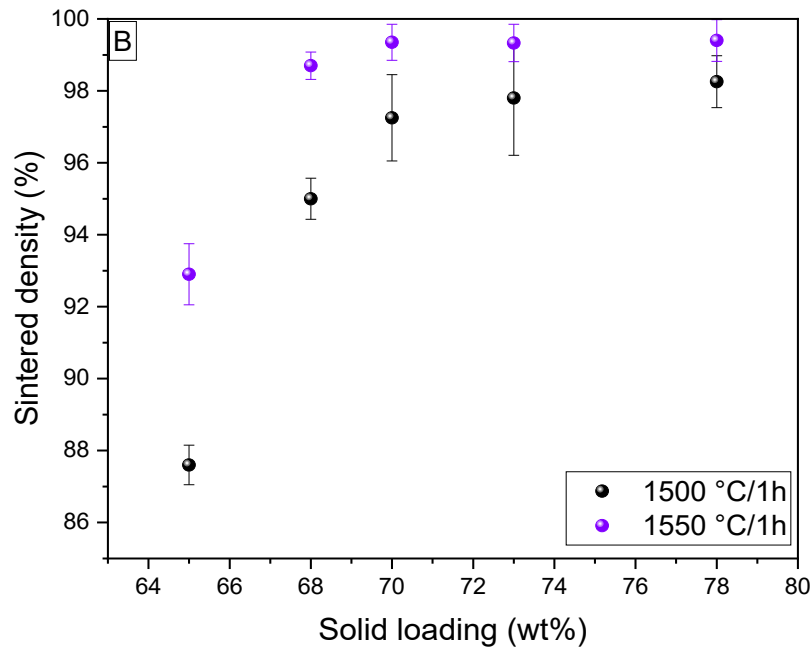
Figure 4.14 Green density (A) and sintered density (B) of the 65 wt% - 80 wt% slurries. 1500 ∘C/1 h (black) and 1550 ∘C/1 h (purple).

As already indicated by the density values, the FESEM micrographs polished and thermally etched surfaces exhibit a homogeneous microstructure, free of printing flaws with an excellent distribution of the two phases, zirconia and alumina. In figure 4.15, the microstructures of the printed samples from the slurries at 70, 73, and 78 wt%, namely those representing the samples with the higher final densities after sintering at 1500 °C/1 h are shown. Therefore, the addition of the dispersant Disperbyk-103 in the slurries' formulation gave excellent results for the enhancement of the microstructure with an evident decrease of the flaws. Some pores are still present due to bubbles entrapped in the slurry that cannot be totally removed. Inevitable pores in the inner area of the sample are more difficult to eliminate than those along the edges [13].
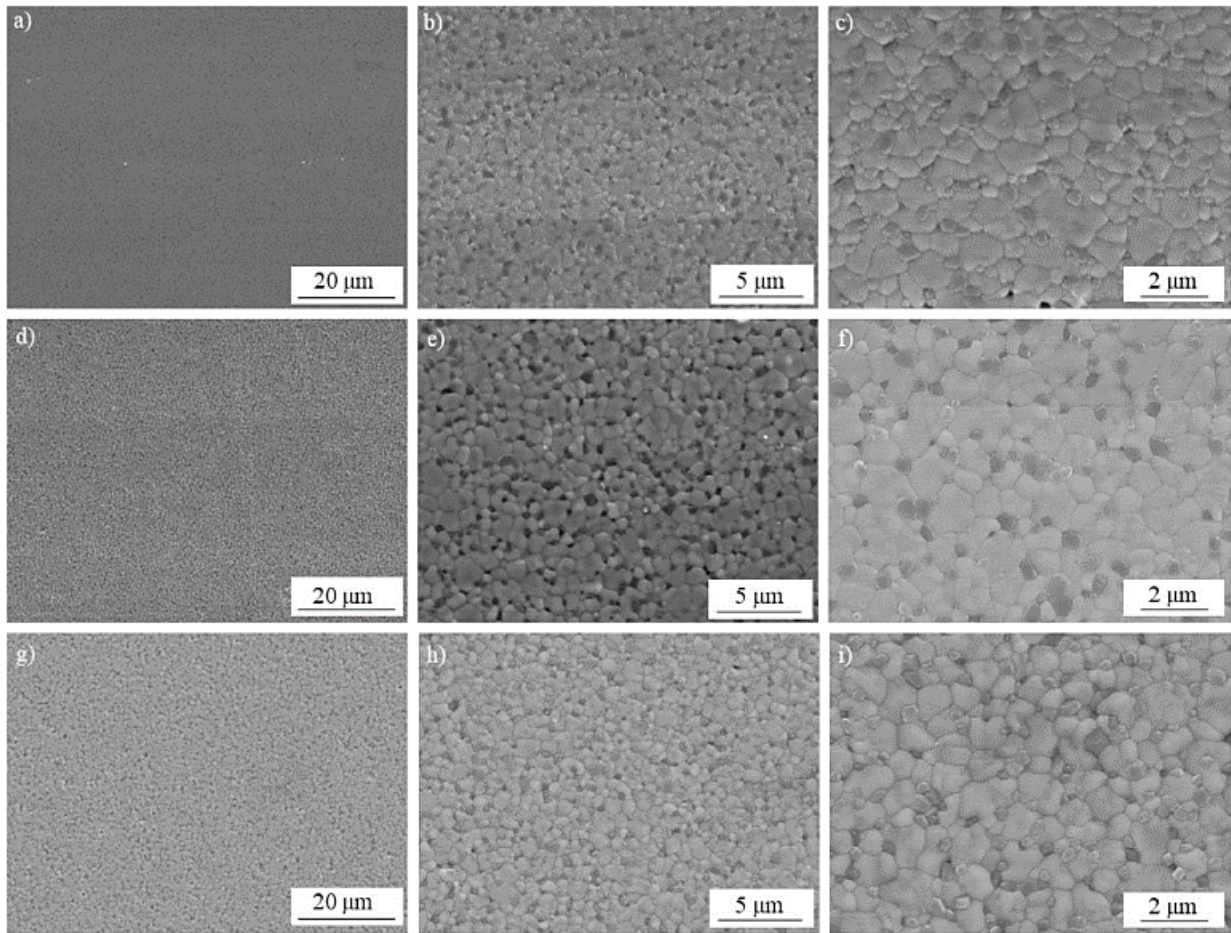
Figure 4.15 FESEM micrographs of printed samples of the slurries at 70 wt%+1% Disperbyk-103 (a–c), 73 wt%+3.5 Disperbyk-103 (d–e) and 78 wt%+2.5 Disperbyk-103 (g–h) sintered at 1500 ∘C/1 h.

After the addition of the dispersant and the optimization of the solid loading the microstructures are satisfying, the phenomenon of delamination was less serious but still present.

The delamination occurs due to the stress between the new cured layer and the portion of the sample already printed, preventing a strong bonding and the fusion between the new layer and the former one. The cause of the delamination is not

only one but is due to a combination of contributing factors. In the next chapter will be explained how the delamination was further reduced and maintained under control during the post-printing treatments.

4.4 Statistical analysis through Principal Component Analysis (PCA)

Principal Component Analysis [24,25] is a multivariate tool for exploratory data analysis. It is a decomposition technique that projects the data from the starting high-dimensional domain to a lower dimensionality one, which is represented by a set of new variables, called Principal Components (PCs).

The PCs are a linear combination of the initial variables and describe the largest sources of variability in terms of captured variance. The components of PCA are *nested*, which means that, given the first PC characterizing the direction of maximum variance in the data, each following component will have the highest possible variance, under the limitation of orthogonality in relation with all the previous components.

Each principal component is constituted by two vectors, one of the scores indicated with t and a second of the loadings indicated with p. Equation 4.1 represents the PCA decomposition equation, where X indicates the original data modelled utilizing F PCs, thus the $\hat{X}$ matrix refers to the modelled part of the original data, while the E matrix depicts to the unmodeled part, also called the "residuals".

$$\mathbf{X} = \Sigma^{\mathrm{F}}_{f=1}\, \mathbf{t}_f \cdot \mathbf{p}^{\mathrm{T}}_f + \mathbf{E} = \mathbf{T}\mathbf{P}^{\mathrm{T}} + \mathbf{E} = \hat{\mathbf{X}} + \mathbf{E}$$

Given that set of PCs corresponds to the axes of the low-dimensional space the data are projected onto, the values of the score vector $\mathbf{t}_f$ represent the samples'

coordinates on the fth PC or axis, and the loadings values of vector $\mathbf{p}_f$ indicate the contribution of the original variables to that PC. A graphical representation of the PCA model is shown in Figure 4.16. The model highlights how the product $\mathbf{TP}^T$ constitutes the modelled part of the original data, in contrast to $\mathbf{E,}$ the residual matrix [26].
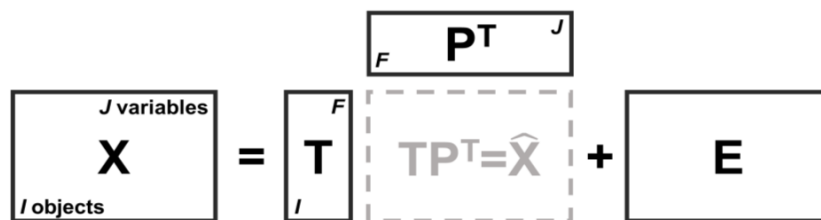
Figure 4.16 Representation of the PCA model.

In an ideal PCA model $\hat{X}$, the modelled part includes all the structured variability, and the uninformative variability of the starting data is left in $\mathbf{E,}$ the residuals matrix. The information content of the X input matrix as modelled by PCA can be inspected by looking at the scores, loadings and residuals plots. The score plots are 2D or 3D representations of the modelled data and are obtained by plotting one score vector t against another (i.e., two different components plotted against each other).

The loadings plots provide information about the relations among the original variables, whose values on the different PCs (the values contained in the loading vectors p) also describe how the original variables influence each PC. For the same pair of inspected PCs, directions on the scores and loadings plots are coincident (i.e., they describe the same multivariate space).

According to Jaadi [27], "the loading plot represents the directions of the data that indicate the maximal degree of variance. The lines' direction and length represent the variance and the information' relationship. The larger the variance of a line, the larger the dispersion of the data points along it; and the larger the dispersion along

128

a line, the more information it has. Therefore, PCs can be interpreted as new axes that provide the best angle from which to view and evaluate the data, so that the differences between the observations are more visible."

The fact that the original variables are combined into few new "summary" ones makes PCA also a good "compression" or features extraction method, which is extensively used for handling large datasets and reducing the computational time needed for modelling.

PCA was performed using the PLS_Toolbox (version 8.6, Eigenvector Research Inc. WA, USA) under MATLAB (2022b, Mathworks, MA, USA) environment.

4.4.1 Application of PCA to the stereolithography process

Principal Component Analysis (PCA) is an exploratory data analysis method useful for extracting relevant information from a sample of vectors in order to ascertain which are the fundamental values with the greatest influence on the printing process [28,29]. PCA is often used to effectively remove redundancy and reduce the dimensionality of a huge set of data by compressing its size while retaining the majority of the information and enabling a speedy evaluation of any correlations between variables [29]. In this work PCA was applied to identify the major sources of variability in the datasets, to better understand how the variables of the printing process (since the dispersion of the raw ceramic powders until the mechanical testing of the sintered parts) affect one another, and to identify the most promising slurry formulation. It is not easy to accurately explain how the printing parameters affect each other. There are many influencing factors that sometimes lead to contradictory conclusions. PCA helps to overcome these issues and to better understand the 3D printing stereolithographic process [30].

Before performing PCA, the original datasets were standardised, and their suitability for PCA was determined. PCA was performed on a dataset related to

different job printings. The acquired data consist of seven variables that could be divided in two groups: input parameters (the set conditions) and the output properties that means the response of the material to that specific condition. The input parameters are: the solid loading (SL), the dispersant concentration (DC), the led power (LP), the exposure time to the UV light (ET) and the layer thickness (LT). The output properties are the bending strength (BS) and the theoretical density (TD%). The basic rationale in PCA is that the informative rank of the data is compressed in comparison to the original variables yielding statistical benefits or rather, the number of principal components is equivalent to the original variables while the number of significant PCs might be lower, depending on the correlations between the original variables [29]. The general visualization is aided by the presence of much fewer variables than the starting data and by the minimization of the noise as the original variables are replaced with weighted averages [24]. In accordance with the literature [31], the eigenvalues should be higher than 1 and the cumulative variance (%) should be more than 80%.

In figure 4.17, the bar plot of the variance explained by the PC is depicted. This graph is useful to estimate the number of components by looking at the point where a plateau is reached after which the model would be overfitted (noise contribution).
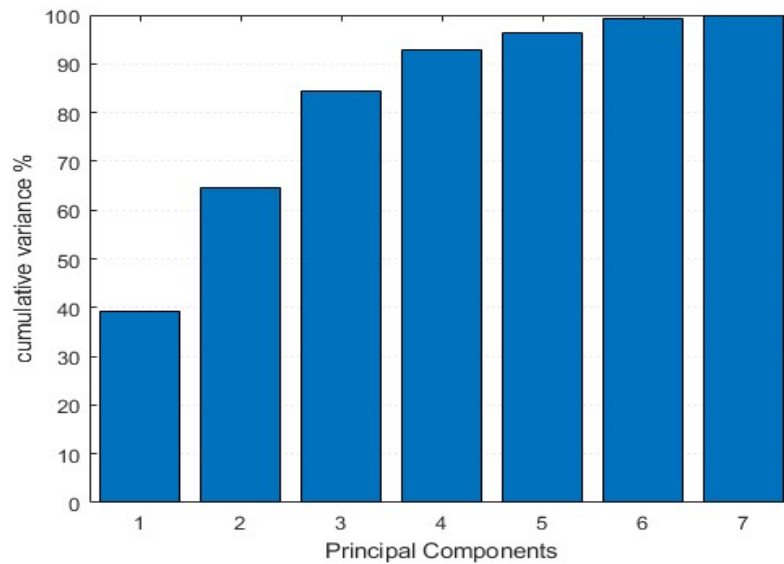
Figure 4.17 Cumulative variance bar plot

The characteristic values of the PC1, PC2, and PC3 are higher, that is, contribute the most to the explanatory variables. Therefore, the extraction of the first three PC is the most suitable and the cumulative variance contribution rate is 87.94%.

The model was designed with three principal components (PCs) also to minimize the root mean square error of cross-validation (RMSECV). The other PCs would not be expected to have significant leverage if kept in the model and were unconsidered (figure 4.18) [32].
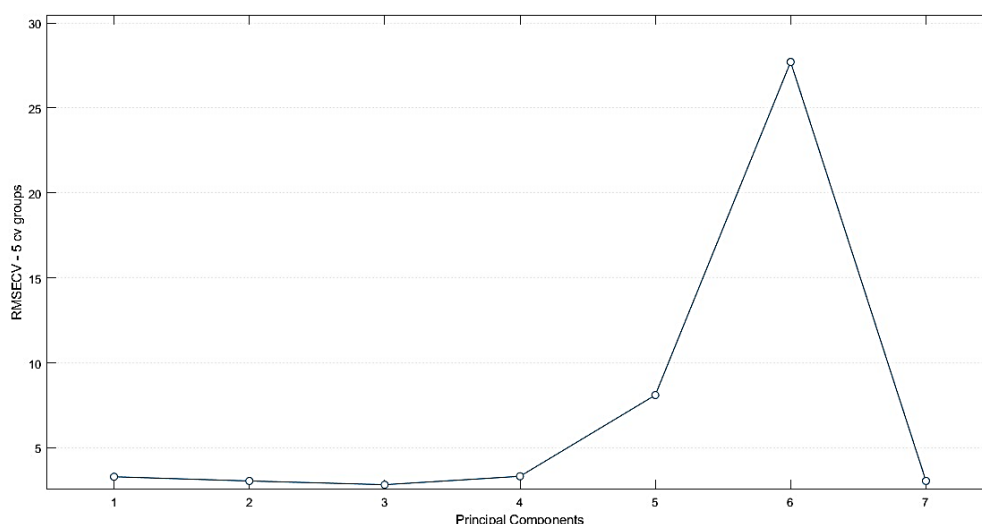
Figure 4.18 Root mean square error of cross-validation (RMSECV) vs principal components

In figure 4.19A the variables of the printing process are plotted as a function of the PC1 loadings. Next to it, the PC1 scores graph was inserted. In the PC1 scores each label corresponds to one printing job in which, by the way, the seven printing process variables vary. Their comparison helps to better understand which printings show similar characteristics, and which ones are more influenced by one parameter. For example, the print 73 wt % + 3.5% Disperbyk-103, according to the bar plots of the loadings, presents a high dispersant concentration, a high exposure time and thickness of the layer. In contrast, this formulation shows a low theoretical density. By checking the data, this information is correct but, with the help of the PCA, the interpretation happens in a more immediate mode.

As depicted in figure 4.19 (A) three indexes such as theoretical density (TD%), exposure time (ET), and dispersant concentration (DC) have large load factors in the PC1. The other three indexes are relatively weak. Three indexes such as solid loading (SL), led power (LP), and thickness of the layer (TH) have large load factors in the PC2 (B). In PC3 the bending strength (BS) shows the highest load factor (C).
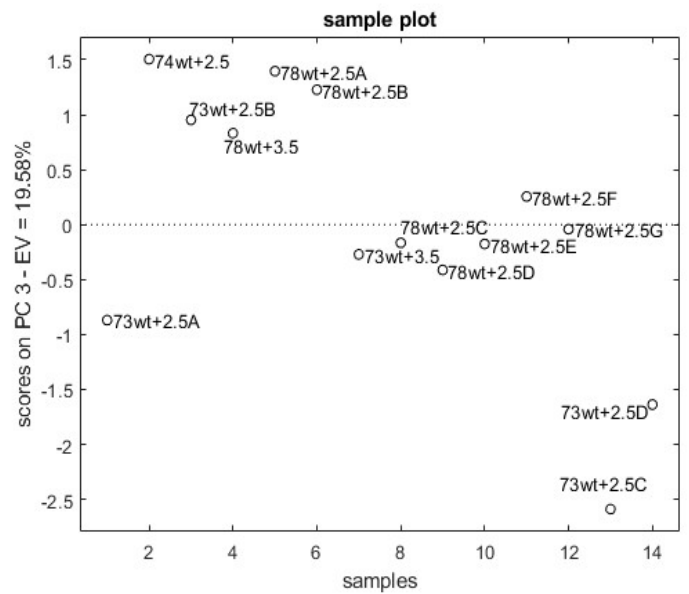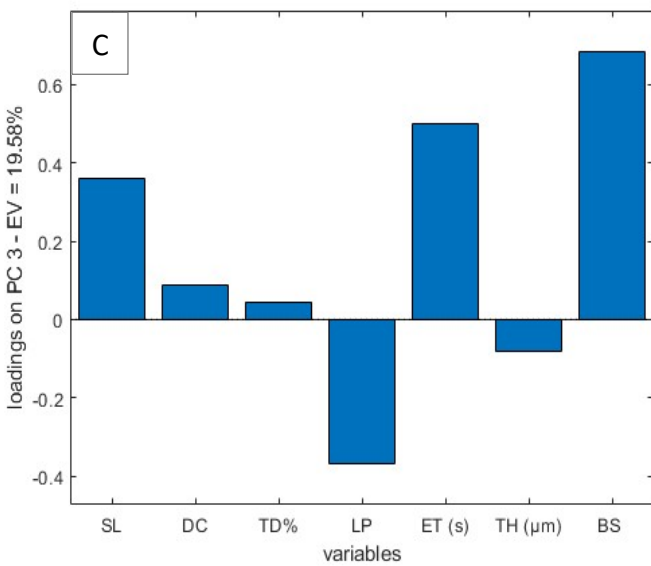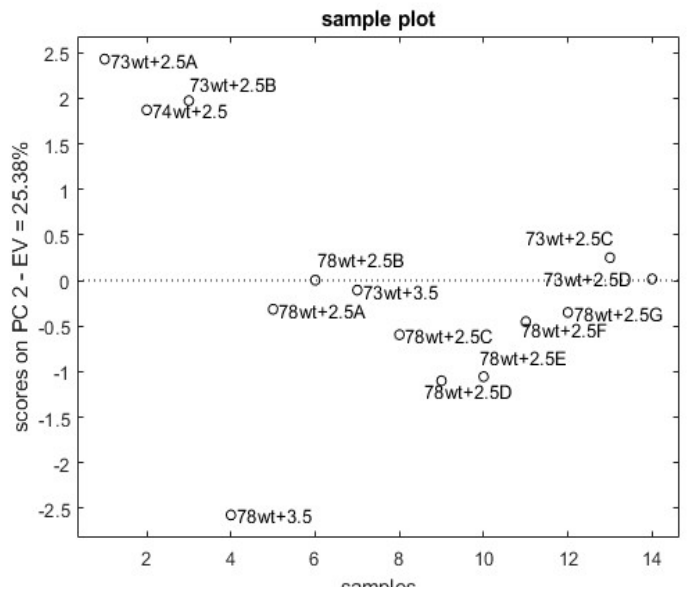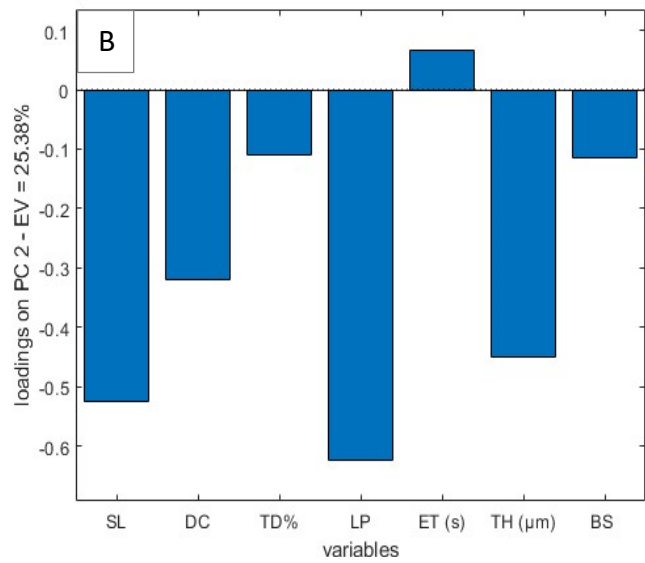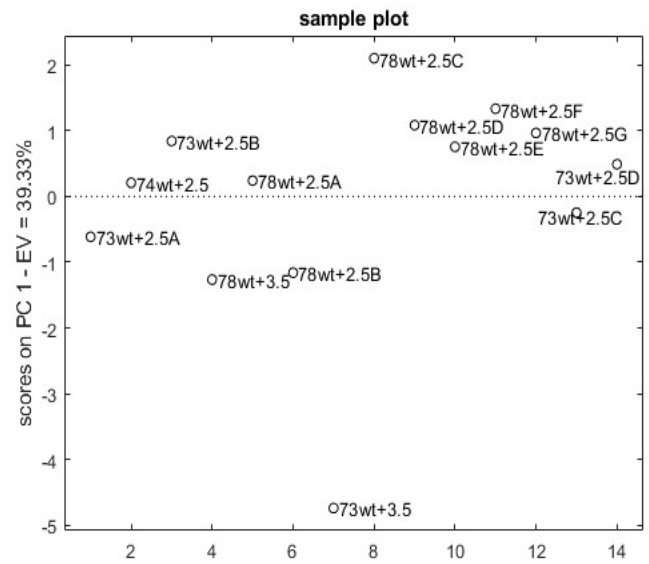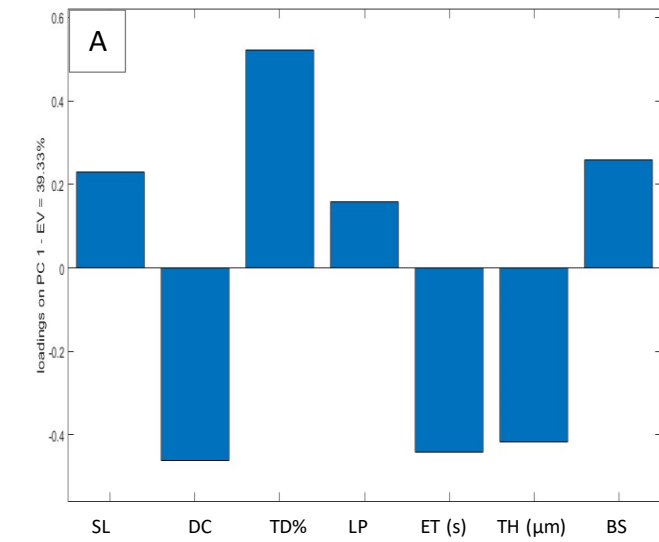
Figure 4.19 PC1 (A), PC2 (B), and PC3 (C) loadings plotted, as a function of the printing process parameters variables, compared to the corresponding score plots

All information explored one PC at a time in figure 4.19 can also be inspected in a more global manner, by plotting one PC against another, for both the loadings and scores. The pairs of loadings and scores plots of figures 4.20-22 can be therefore obtained and interpreted. In figure 4.20, for instance, PC1 vs PC2 loadings plots are depicted on the left. Based on the position of each parameter on the graph, the reciprocal interaction can be understood also from a statistical point of view. The angles between the vectors tell us how the characteristics correlate with one another. When two vectors are close, forming a small angle, the two variables they represent are positively correlated. If they meet each other at 90°, they are uncorrelated. When they diverge and form a large angle (close to 180°), they are negatively correlated, at least for the information described by the two PCs under examination (i.e., the axes of the plot). Thus, the mechanical properties, such as the bending strength are positively correlated with the theoretical density (TD%), as well known, a fully densified material will present less defects and porosity which negatively affect the mechanical behavior exponentially. Also, the led power and the solid load affect each other positively. The increased amount of ceramic particles in the photocurable slurry reduces the resolution owing to light scattering thus, an increase of the led power is necessary for obtaining a well-polymerized single layer [11].

The dispersant concentration is positively correlated with the layer thickness. If from one side the dispersant, Disperbyk-103 in our case, strongly contributes to increase the dispersion of ceramic particles in the resin, on the other side it also affects the cure-width behavior and integrity of the green parts, as explained in deep in chapter 1. If the dispersant concentration increases, probably a higher layer thickness could be set because the dispersant decreases the viscosity, making light penetration easier because of homogeneous particle distribution [3,33].

According to PCA the exposure time, which means how long (in seconds) each layer is exposed to the UV light, is negatively correlated with the bending strength and the theoretical density. To improve the bending strength of the final parts and to enhance the theoretical density (TD%), it is reasonable to setup a lower exposure time. This result can be easily connected with the issue of the over curing effect. The properties of the printed samples strongly depend on the exposure mode, an increase in curing depth does not ensure better mechanical properties but each layer must be exposed for a sufficient time to ensure a strong adhesion between the layers and, at the same time, the polymerization shrinkage stress should be decreased (figure 4.20)[34].
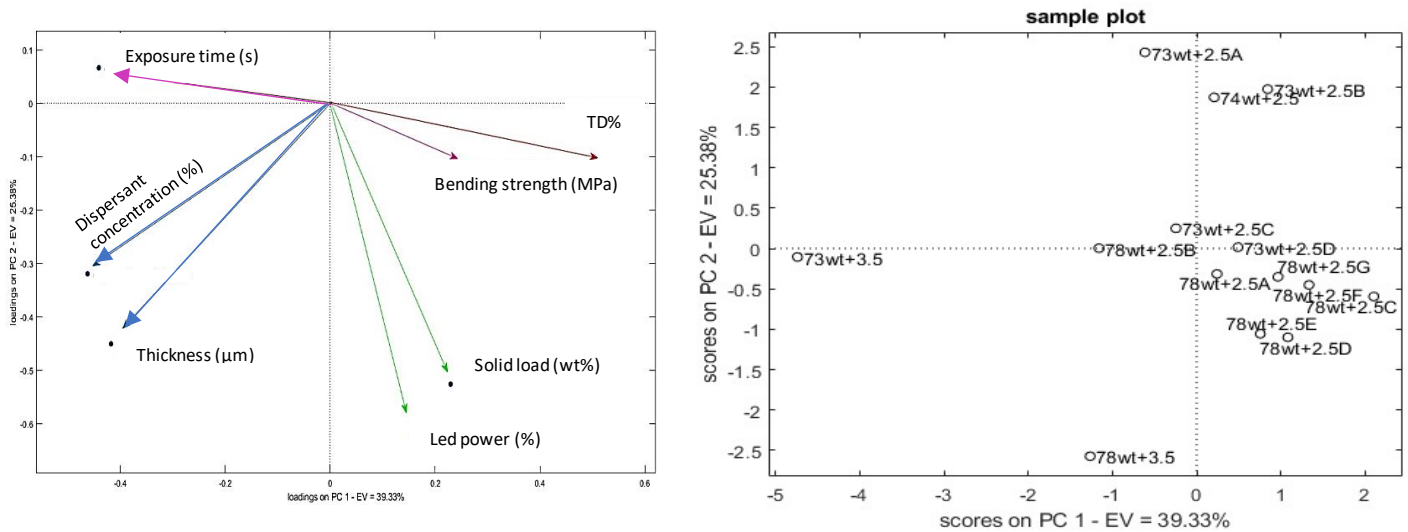
Figure 4.20 PC1 vs PC2 loadings and scores plots

In the PC1-PC3 loading it is interesting to notice that the solid loading is positively correlated with the bending strength. As well-known from the literature, the solid loading of the ceramic suspension shows obvious influences on the viscosity of the slurries, as well as the density and strength of the final printed parts. Ceramic suspensions with a high solid loading are required to reduce the shrinkage, avoid the cracks and increase the strength of the green and final printed body [35] (Figure 4.21).
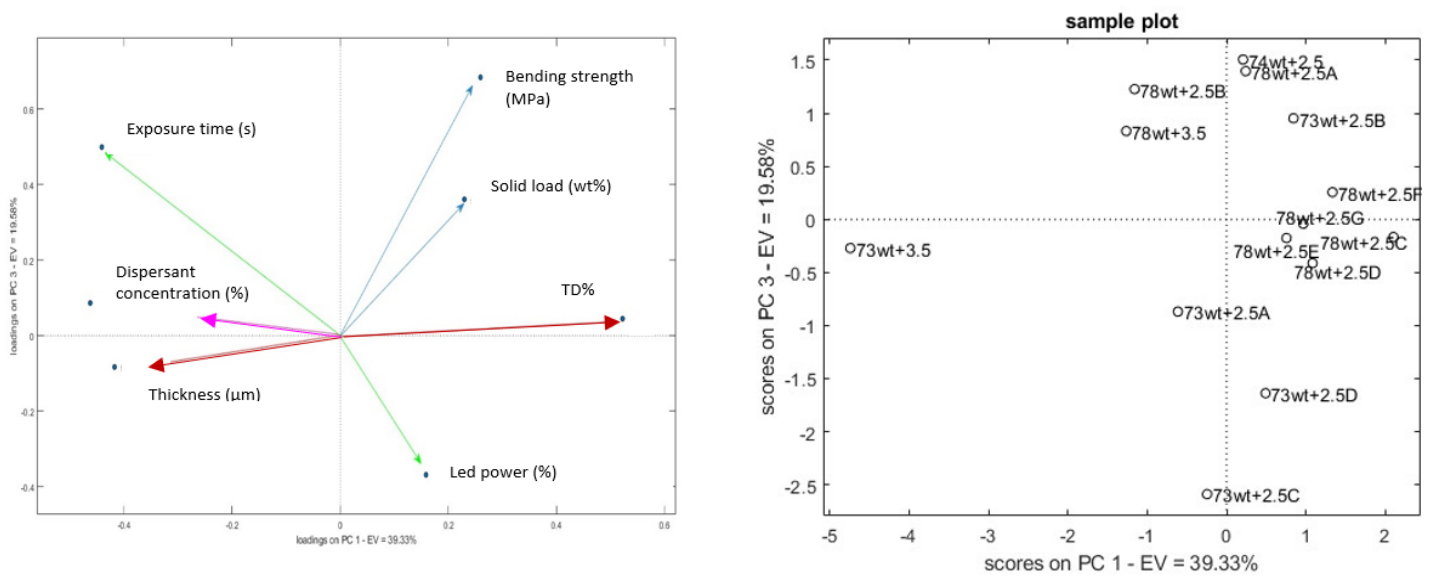
Figure 4.21 PC1 vs PC3 loadings and scores plots

In figure 4.22, The PC2-PC3 loadings are plotted. The most noticeable correlations between the printing process parameters are the positive correlation between the led power and the thickness of the layer. In this work, it was chosen to work from a minimum light output of 26.23 mW/cm^2 to a maximum light output of 31.96 mW/cm^2. Furthermore, the bending strength seems not to be linked with the led power. All the information obtained from the PCA analysis is in agreement with the literature, suggesting that the correlations are robust.
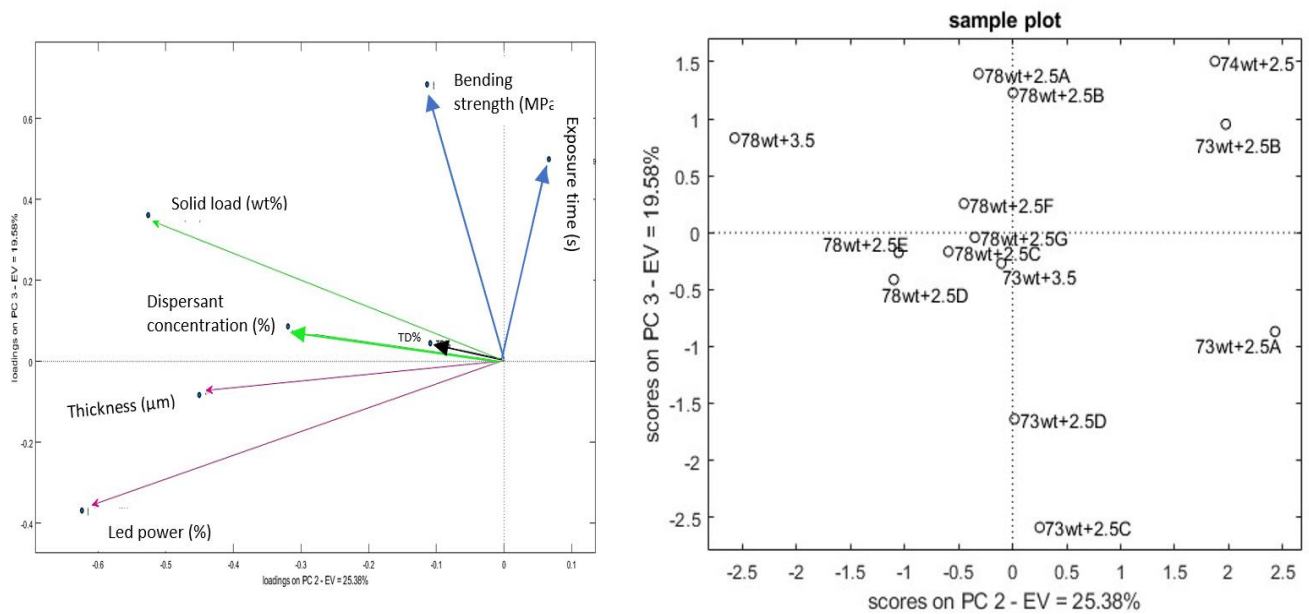
Figure 4.22 PC2 vs PC3 loadings and scores plots

In table 4.3 the correlations of the different printing parameters obtained by the PCA analysis are depicted. A positive correlation is referred when a parameter increased the correlated one also increases or of negative correlation when the behaviours of the two parameters is opposite, as one increases the other decreases. The two parameters are not correlated if one no affect in no way the other.

Parameters	TD%	Solid load (%)	Layer thickness (μm)	Bending strength (MPa)	Exposure time (s)	Led power (%)	Dispersant concentration (%)
TD%		Positively correlated	Not correlated	Positively correlated	Negatively correlated	Negatively correlated	Not correlated
Solid load (%)	Positively correlated		Not correlated	Positively correlated	Not correlated	Positively correlated	Positively correlated
Layer thickness (μm)	Not correlated	Not correlated		Not correlated	Not correlated	Positively correlated	Positively correlated
Bending strength (MPa)	Positively correlated	Positively correlated	Not correlated		Negatively correlated	Not correlated	Not correlated
Exposure time (s)	Negatively correlated	Not correlated	Not correlated	Negatively correlated		Negatively correlated	Not correlated
Led power (%)	Not correlated	Positively correlated	Positively correlated	Not correlated	Negatively correlated		Not correlated
Dispersant concentration (%)	Not correlated	Positively correlated	Positively correlated	Not correlated	Not correlated	Not correlated	

Table 4.3 Resume of the correlations of the different printing parameters obtained by the PCA analysis

The robustness of the model was confirmed also by Hotelling's T^2 versus the Q residuals plot (figure 4.23). It is a statistical summary that explains how well a model is built. All samples fall inside both limits defined by Q and T^2 values, but, if one had stayed out of the plot it could have been considered for further investigations and possibly to be removed from the dataset [36]. This plot helps in highlighting samples with strange behaviours, which generally corresponds to information that is unique for such samples: if this unexpected piece of information can be related to experimental or measurement errors, the sample can be identified as an outlier, and removed from the dataset. In our case all samples resulted well-modelled, and they also appear rather homogeneous.
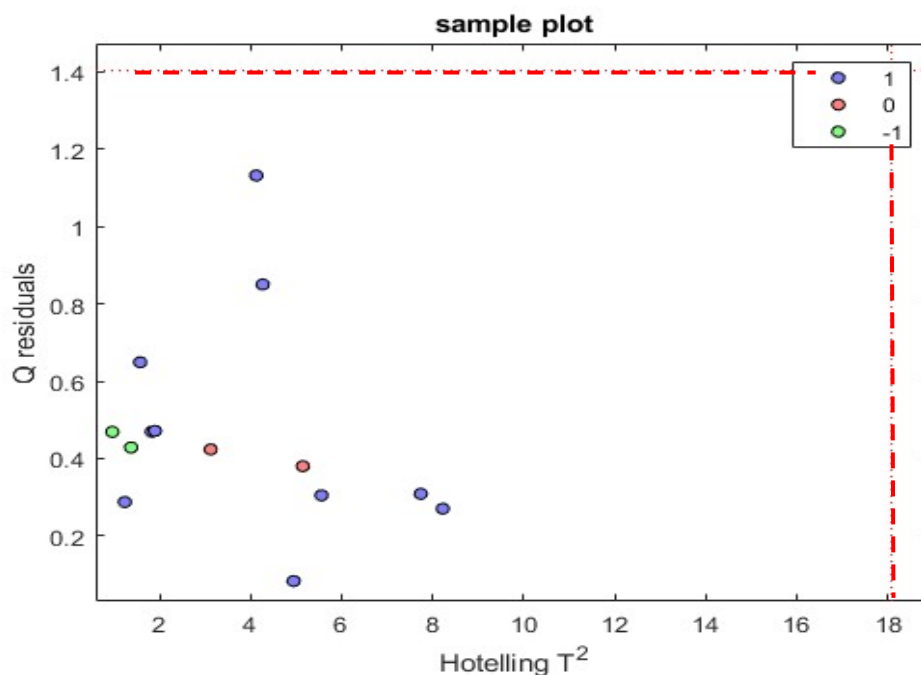
Figure 4.23 Hotelling's T^2 vs. the Q residuals (influence plot) of the PCA model

A statistical approach based on cross-analysis of the data was performed. The scores plots were compared with the loading's plots. To get the complete image of the information content it is necessary to see scores and loadings together, as they are complementary each other: the loadings tell us why there is a particular arrangement of samples in the scores. Due to the substantial number of graphs, and due to space constraints, they are not shown. Since the PCA was done on a dataset of printings with a slurries' solid loading ranging from 73 wt% to 78 wt%, it was necessary to identify which was the most favourable composition in terms of process parameters in order to obtain an outstanding microstructure, and a fully densified material with optimal mechanical performances. Each graph gives an indication of the process parameters and finally, a slurry with a 78 wt% of solid loading with 2.5% of Disperbyk-103 was selected as our best formulation regarding the microstructure, density and mechanical properties, as explained in chapter 5.

For this formulation, the most appropriate power of the led was 26.23 mW/cm^2. This yields to a curing depth of ~30 μm (1.5 times larger than the build layer thickness), sufficient to ensure the bonding between the interlayers.

All the curing depth studies were investigated with a led power between 26.23 mW/cm^2 and 31.96 mW/cm^2. According to the PCs, the debinding of the printed parts with distilled water was the best choice, this was confirmed by the tests carried out and discussed in detail in chapter 5.

Finally, regarding the exposure time, PCs suggested a "shorter" time of exposure that could be interpreted as avoiding E.T. higher than 20 seconds. It is not possible to fix a precise value but after 20 s, for the slurry with 78 wt% + 2.5% Disperbyk-103, the scattering occurs, as discussed formerly.

In table 4.4 the features of the 78 wt% + 2.5 Disperbyk-103 slurry formulation are depicted.

Starting materials	$ZA_{16}Ce_{11}$ powder	Disperbyk-103	Acrylic resin
Main usage	Filler	Dispersant	Medium
Density (g/cm^3)	5.87	1.06	1.10
Mass fraction (wt%)	78	1.95	20.05
Volume fraction (vol%)	39.84	5.52	54.65

Table 4.4 Features of the 78wt% + 2.5 Disperbyk-103 slurry

4.5 Development and printing of the *ZA₈Sr₈Ce₁₁*

$Ce_{11}ZA_8Sr_8$ slurries were produced as further development of the PhD thesis. It was chosen to analyse previously the $Ce_{11}ZA_{16}$ because, as discussed in detail in chapter 3, the production of this triphasic powder needs a long time.

On the basis of the previously exposed accurate and deep study of the $Ce_{11}ZA_{16}$, it was possible to optimize the printing process.

4.5.1 Characterization of *Ce₁₁ZA₈Sr₈*

First of all, likewise the biphasic slurries, dispersant-free slurries, composed only by sieved and dried ceramic powder and by Admatec acrylic resin, were prepared at 60.0 wt%, 62.5 wt%, and 65 wt%. The rheological behavior of the slurries can be observed in figure 4.24.

As shown in the graph, as the solid loading increased, the shear viscosity also increases attributable to an ever-greater fraction of ceramic particles that cause higher friction.

All the investigated slurries presented a shear-thinning behavior, with a decrease of the viscosity as the shear rate increases due to the alignment of the structural units in the flow direction under an applied stress, improving the system's flow [14]. At the operative shear rate of 160 s^{-1} a shear viscosity of 2.5, 3.1 and 3.9 Pa·s, was recorded for the slurries at 60, 62.5, and 65 wt% solid loadings, respectively.

The formulations without the dispersant Disperbyk-103 showed a microstructure with printing and debinding flaws and inhomogeneity. The less promising formulation was the 60 wt% but, as the solid load increases the microstructure becomes more homogeneous, and the density increases. The theoretical density of the samples fired at 1500 °C/ 1 h was 86.5%, 87.2, and 96.7 for the 60 wt%, 62.5 wt%, and 65 wt% slurries respectively. The theoretical density of the samples fired

at 1550 °C/ 1 h (FESEM micrograph not shown) was 91.5%, 88.9, and 97.1 for the 60 wt%, 62.5 wt%, and 65 wt% slurries respectively (figure 4.25).
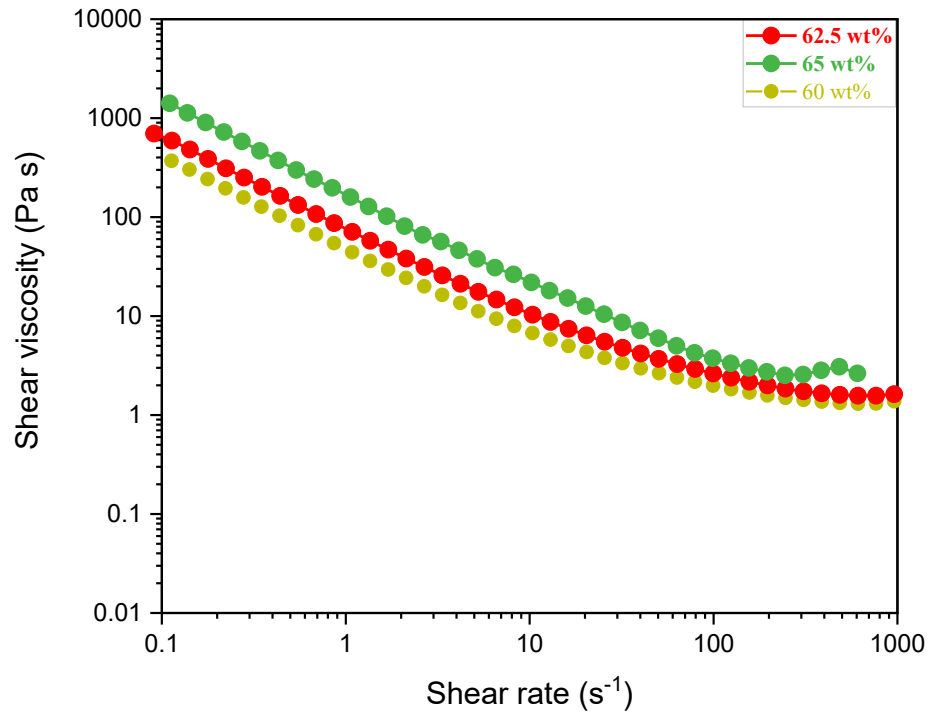
Figure 4.24 Shear viscosity of the 60 wt%, 62.5 wt%, and 65 wt% slurries
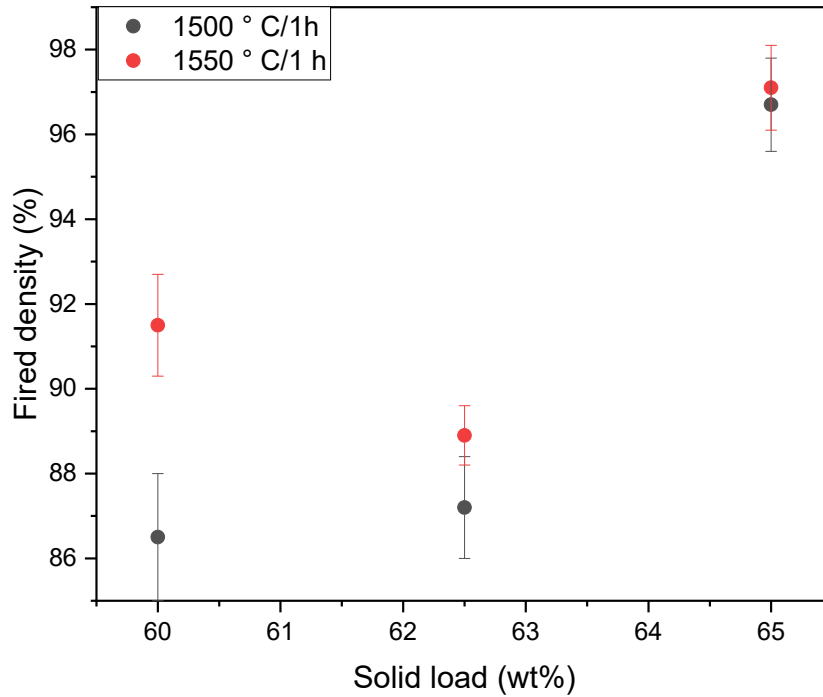
Figure 4.25 Fired density of the sintered parts at from 60 wt% to 65 wt% of solid loadings without dispersant

Due to the printing flaws and the not complete densification, the recipes were further optimized by the addition of the commercial dispersant (Disperbyk-103), which permitted a substantial increase of the solid loading from 65 wt% (maximum obtainable with only powder and resin) up to 78 wt%, precisely, at 70, 73, 75, and 78 wt%. The quantity of dispersant was optimized for each slurry on the base of rheological studies. The amount of dispersant was added in the range of 2.0 - 2.5 wt% with respect to the weight of the dry powder.

Figure 4.26 displays the rheological behaviours of the slurries with different concentrations of dispersant. As can be seen, all the slurries showed a shear-thinning behaviour, as already observed for the slurries without the dispersant.
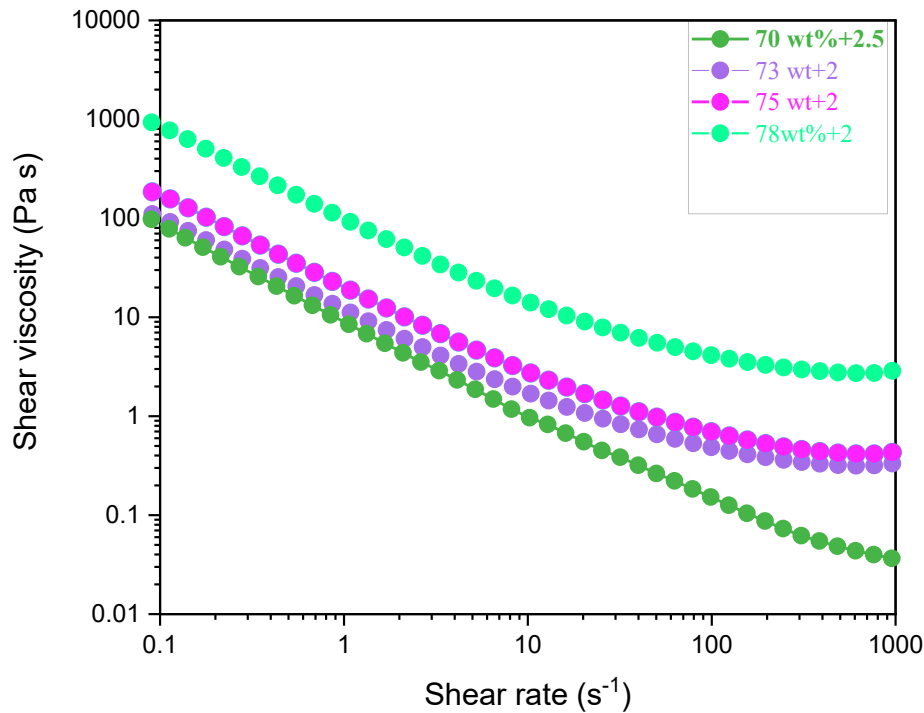
Figure 4.26 Shear viscosity of the 70 wt % to the 78 wt % slurries

After sintering, the fired Archimedes' densities (%TD) were measured by the buoyancy method.

As shown in figure 4.27 the density of the sintered parts increases as the solid loading also increases.

From 70 wt% to 78 wt% the density continues to increase until almost complete densification. The 75 wt%+2 Disperbyk-103 showed an opposite behaviour probably due to the not perfectly homogeneous slurry.

The density of all the samples showed a moderate increase from 1500 °C to 1550 °C. The density of the samples produced with the 70–73 wt% slurries rose of ~3 %. The higher densification was achieved in the samples made with the 78 wt% slurry, with values of 96 % and 96.6 % at 1500 ◦C/1 h and 1550 °C/1 h, respectively. In figure 4.26 6C and 7C, is it also possible to observe that the strontium hexaluminate platelets were successfully developed in the Ce-TZP matrix.
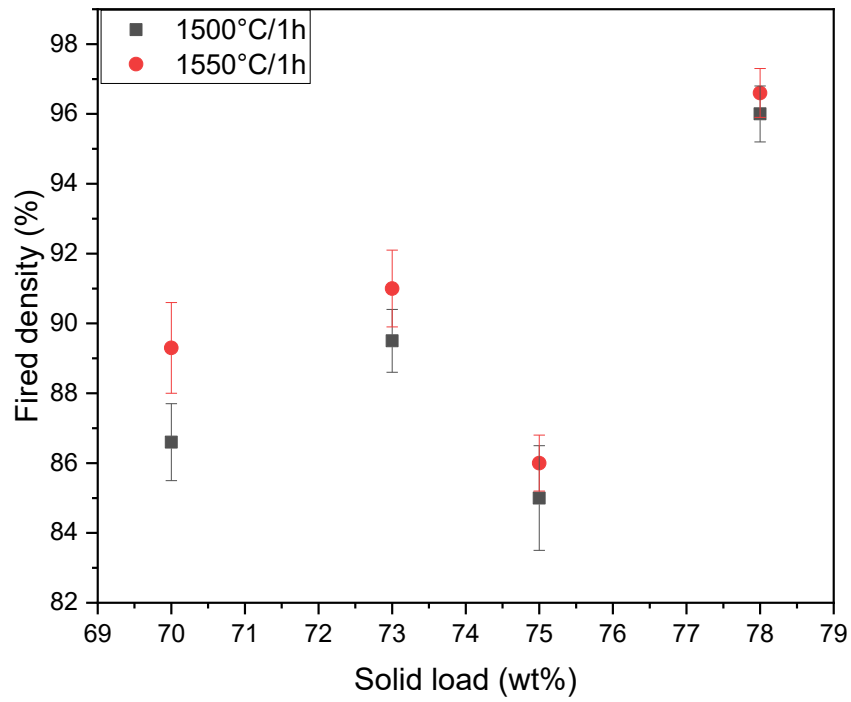
Figure 4.25 Fired density of the sintered parts from 70 wt% to 78 et% of solid loading
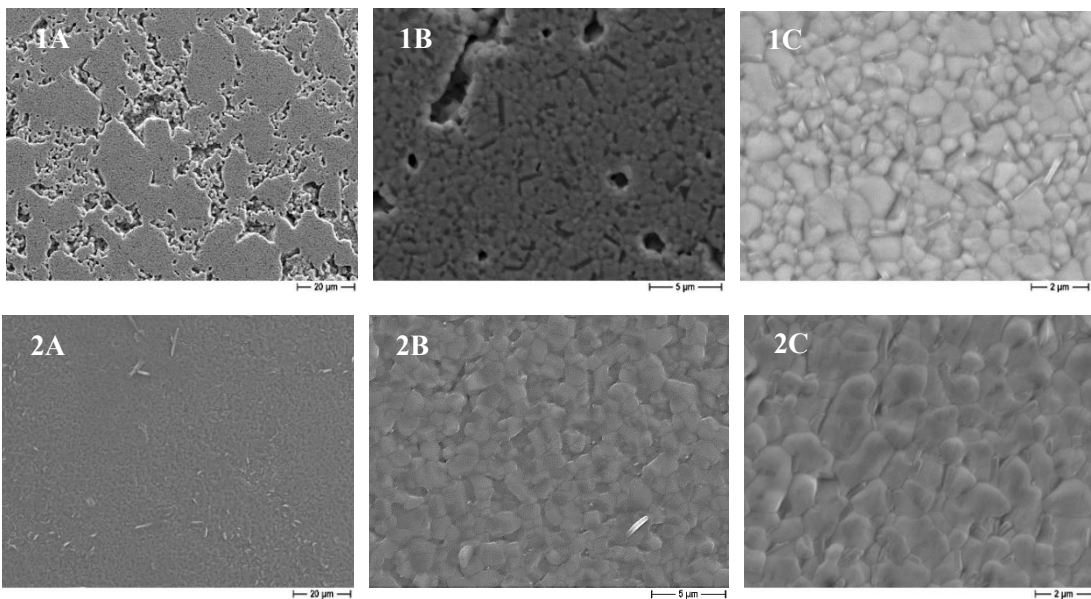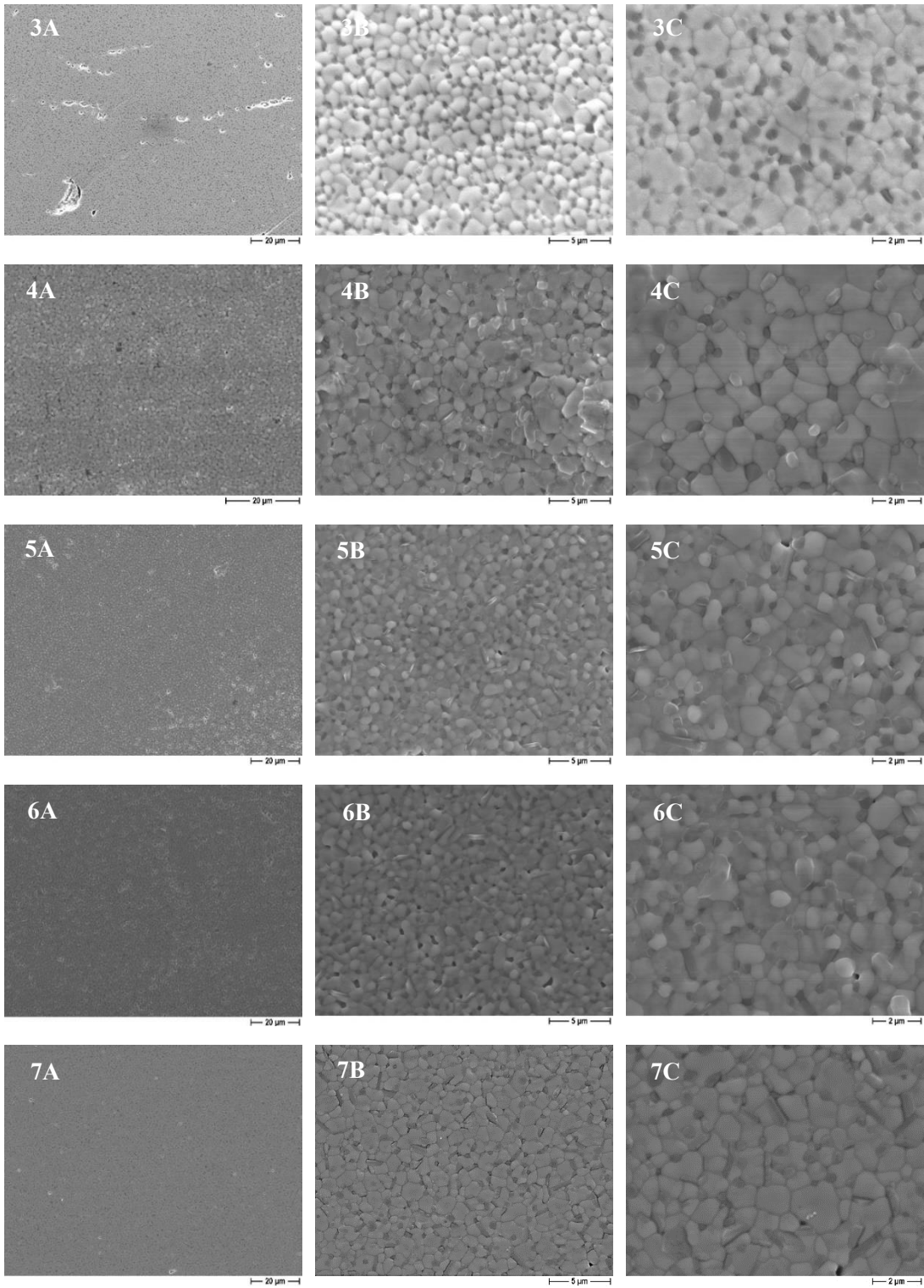
Figure 4.26 FESEM micrographs of *Ce₁₁ZA₈Sr₈* at 60 wt% (1 a-c), 62.5 wt% (2 a-c) and 65 wt% (3 a-c) without dispersant. The formulations 70 wt% +2.5 % Disperbyk-103 (4 a-c), 73 wt%+2 % Disperbyk-103 (5 a-c), 75 wt% + 2 % Disperbyk-103 (6 a-c), and 78 wt%+2.5 Disperbyk-103 (7 a-c) sintered at 1500 ∘C/1 h are also shown.

4.5 Conclusions

In this chapter, the production process of printable $Ce_{11}ZA_{16}$ and $Ce_{11}ZA_8Sr_8$ slurries for the development of dense materials was described. At first, the acrylic resin was studied in terms of thermal behaviour by means of TGA-DTA analysis. FT-IR analysis was performed to compare the behaviour of the resin after the curing and after the water debinding steps. $Ce_{11}ZA_{16}$ system was explored first. Stable photosensitive slurries with low viscosity were developed and with a shear-thinning behaviour. The addition of the dispersant (Disperbyk-103) to the formulation allows the increase of the solid loading maintaining favourable flowability and stability.

Through PCA analysis, the most convincing slurry formulation suitable for the production of parts with favourable mechanical properties was identified. The most promising slurry formulation for $Ce_{11}ZA_{16}$ was 78% of solid load (optimized for a mean particle size of 0.3 µm) with the addition of 2.5 wt% Disperbyk-103 as dispersant (related to the mass of powder). The optimized slurry had a viscosity of 2.8 Pa s at a shear rate of $160 s^{-1}$. The maximum density was achieved by the samples made from a slurry with 78 wt% solid loading, providing values of 98.3% and 99.4% after firing at 1500 ◦C/1 h and 1550 ◦C/1 h, respectively.

As a further development of the work, $Ce_{11}ZA_8Sr_8$ composite was printed too. Further studies will be necessary to better tailor the process in order to fully exploit the potential of this material. The maximum density was achieved again in the samples printed with the slurry with 78 wt% solid loading, providing values of 96 % and 96.6 % after sintering at 1500 ◦C/1 h and 1550 ◦C/1 h, respectively. Despite the good flowability of the printable slurries, with a shear-thinning behaviour that leads, for the slurries with the higher solid load, to a homogeneous microstructure, printing flaws and defects such as delamination of the layers are still present making them not suitable for the mechanical tests. The assumption of this material is very positive but further studies are necessary.

References

1. Salamon, D., Sokola, P., Kalina, M. & Krousk, J. Kinetic stability and rheological properties of photosensitive zirconia suspensions for DLP printing Tom a. 31–34 (2023). doi:10.1016/j.ceramint.2023.02.223

2. Coppola, B., Lacondemine, T., Tardivat, C., Montanaro, L. & Palmero, P. Designing alumina-zirconia composites by DLP-based stereolithography: Microstructural tailoring and mechanical performances. *Ceram. Int.* **47**, 13457–13468 (2021).

3. Camargo, I. L. de, Morais, M. M., Fortulan, C. A. & Branciforti, M. C. A review on the rheological behavior and formulations of ceramic suspensions for vat photopolymerization. *Ceram. Int.* **47**, 11906–11921 (2021).

4. Hinczewski, C., Corbel, S. & Chartier, T. Ceramic suspensions suitable for stereolithography. *J. Eur. Ceram. Soc.* **18**, 583–590 (1998).

5. Song, S. Y., Park, M. S., Lee, J. W. & Yun, J. S. A study on the rheological and mechanical properties of photo-curable ceramic/polymer composites with different silane coupling agents for SLA 3D printing technology. *Nanomaterials* **8**, (2018).

6. Griffith, M. L. & Halloran, J. W. Freeform fabrication of ceramics via stereolithography. *Journal of the American Ceramic Society* **79**, (1997).

7. Zhang, C., Jiang, Z., Zhao, L., Guo, W. & Gao, X. Stability, rheological behaviors, and curing properties of 3Y–ZrO2 and 3Y–ZrO2/GO ceramic suspensions in stereolithography applied for dental implants. *Ceram. Int.* **47**, 13344–13350 (2021).

8. LI Xing-Bang,ZHONG He,ZHANG Jing-Xian,DUAN Yu-Sen, J. D.-L. Powder Characteristics on the Rheological Performance of Resin-based Zirconia Suspension for Stereolithography. *J. Inorg. Mater.* 231–235 (2020).

9. Johansson, P. *et al.* Cycling stability of poly(ethylene glycol) of six

molecular weights: Influence of thermal conditions for energy applications. *ACS Appl. Energy Mater.* **3**, 10578–10589 (2020).

10. Xie, Z. P., Wang, L. L., Yang, X. F. & Zhang, Z. T. Water Debinding for Zirconia Powder Injection Molding. *Key Eng. Mater.* **368–372**, 732–735 (2008).

11. Zakeri, S., Vippola, M. & Levänen, E. A comprehensive review of the photopolymerization of ceramic resins used in stereolithography. *Addit. Manuf.* **35**, 101177 (2020).

12. Salmoria, G. V., Klauss, P., Pires, A. T. N., Roeder, J. & Soldi, V. Investigations on cure kinetics and thermal degradation of stereolithography Renshape™ 5260 photosensitive resin. *Polym. Test.* **27**, 698–704 (2008).

13. Zhang, K., Meng, Q., Cai, N., Qu, Z. & He, R. Effects of solid loading on stereolithographic additive manufactured ZrO 2 ceramic : A quantitative defect study by X-ray computed tomography. **47**, 24353–24359 (2021).

14. Richardson, R. P. C. and J. F. *Non-Newtonian Flow and Applied Rheology. Hypnosis: Developments in Research and New Perspectives* (2008). doi:https://doi.org/10.1016/B978-0-7506-8532-0.X0001-7

15. Cailliet, S., Roumanie, M., Croutxé-Barghorn, C., Bernard-Granger, G. & Laucournet, R. Y-TZP, Ce-TZP and as-synthesized Ce-TZP/Al2O3 materials in the development of high loading rate digital light processing formulations. *Ceram. Int.* **47**, 3892–3900 (2021).

16. Gentry, S. P. & Halloran, J. W. Light scattering in absorbing ceramic suspensions: Effect on the width and depth of photopolymerized features. *J. Eur. Ceram. Soc.* **35**, 1895–1904 (2015).

17. Mitteramskogler, G. *et al.* Light curing strategies for lithography-based additive manufacturing of customized ceramics. *Addit. Manuf.* **1**, 110–118 (2014).

18. Sun, J., Binner, J. & Bai, J. 3D printing of zirconia via digital light processing: optimization of slurry and debinding process. *J. Eur. Ceram. Soc.* **40**, 5837–5844 (2020).

19. Li, X. *et al.* Dispersion and properties of zirconia suspensions for stereolithography. *Int. J. Appl. Ceram. Technol.* **17**, 239–247 (2020).

20. Zhang, K. *et al.* High solid loading, low viscosity photosensitive Al2O3 slurry for stereolithography based additive manufacturing. *Ceram. Int.* **45**, 203–208 (2019).

21. Li, X. *et al.* Dispersion and properties of zirconia suspensions for stereolithography. *Int. J. Appl. Ceram. Technol.* (2020). doi:10.1111/ijac.13321

22. Li, K. & Zhao, Z. The effect of the surfactants on the formulation of UV-curable SLA alumina suspension. *Ceram. Int.* **43**, 4761–4767 (2017).

23. Tomeckova, V. & Halloran, J. W. Cure depth for photopolymerization of ceramic suspensions. *J. Eur. Ceram. Soc.* **30**, 3023–3033 (2010).

24. Bro, R. & Smilde, A. K. Principal component analysis. *Anal. Methods* **6**, 2812–2831 (2014).

25. Jolliffe, I. T. *Principal component analysis, 2nd ed*. (Springer US, 2002).

26. Cavallini, N. New tools for exploratory analysis fusing information from different sources. (University of Copehagen, 2019).

27. Jaadi, Z. A step-by-step explanation of Principal Component Analysis. *Originally published 4 September 2019 updated 25 March 2021. (2021)* Available at: https://builtin.com/data-science/step-step-explanation-principal-component-analysis.

28. Song, J. & Li, B. Nonlinear and additive principal component analysis for functional data. *J. Multivar. Anal.* **181**, 104675 (2021).

29. Booker, N. K., Knights, P., Gates, J. D. & Clegg, R. E. Applying principal component analysis (PCA) to the selection of forensic analysis methodologies. *Eng. Fail. Anal.* **132**, 105937 (2022).

30. Tan, Y., Zhang, J., Li, X., Xu, Y. & Wu, C. Y. Comprehensive evaluation of powder flowability for additive manufacturing using principal component analysis. *Powder Technol.* **393**, 154–164 (2021).

31. He, Y., Pang, Y., Zhang, Q., Jiao, Z. & Chen, Q. Comprehensive evaluation

of regional clean energy development levels based on principal component analysis and rough set theory. *Renew. Energy* **122**, 643–653 (2018).

32. Khalili, K. N. M. *et al.* Monitoring Molecular Weight Changes during Technical Lignin Depolymerization by Operando Attenuated Total Reflectance Infrared Spectroscopy and Chemometrics. *ChemSusChem* **14**, 5517–5524 (2021).

33. Kim, J. *et al.* Effect of dispersants on structural integrity of 3D printed ceramics. 968–978 (2022). doi:10.1111/ijac.13965

34. Shen, M. *et al.* E ff ects of exposure time and printing angle on the curing characteristics and fl exural strength of ceramic samples fabricated via digital light processing. *Ceram. Int.* **46**, 24379–24384 (2020).

35. Zhang, K. *et al.* Roles of solid loading in stereolithography additive manufacturing of ZrO2 ceramic. *Int. J. Refract. Met. Hard Mater.* **99**, 105604 (2021).

36. Di Anibal, C. V., Rodríguez, S., Albertengo, L. & Rodríguez, M. S. UV-Visible Spectroscopy and Multivariate Classification as a Screening Tool for Determining the Adulteration of Sauces. *Food Anal. Methods* **9**, 3117–3124 (2016).

Chapter 5

Post-printing processing and Characterization of dense $Ce_{11}ZA_{16}$ printed parts

In this chapter, the post-printing processing, the aim of which is a progressive removal of the organic matter, is described. After the 3D printing stage described in detail in chapter 4, the green samples underwent a water debinding step followed by a thermal debinding cycle, during which the organic fraction was eliminated, and the remaining ceramic parts were sintered. The influence of the debinding and the sintering on the final properties of the printed parts are discussed. The microstructure and phase composition were also studied. Great attention was dedicated to the mechanical characterization by means of Vickers hardness measurements, fracture strength, and phase transformability.

5.1 Post printing treatments

5.1.1 Water debinding

Once the samples were printed, extra and uncured slurry was gently removed with a paintbrush and distilled water. After that, the bars were submitted to the water debinding step by soaking the samples in a tank filled with distilled water maintained at the constant temperature of 36 °C. This is a crucial step where the water-soluble components of the resin are removed from the inner structure of the sample. In order to study the dimensional changes undergone by the specimens, their length was measured with a high-accuracy digital micrometer every two hours. In figure 5.1, the dimensional change curve is depicted in function of time. Initially, the samples expanded considerably as soon as they came into contact with the water. After the initial sharp expansion, the samples expanded slowly. A linear expansion of about 0.20% after 6 h debinding was reached. After this step, the specimen dimension remained unchanged.

After 10 h, when the parts were removed from the water, a shrinkage was detected due to the temperature change from the 36 °C of the water to the ambient temperature, according to material thermal expansion coefficient, [1].
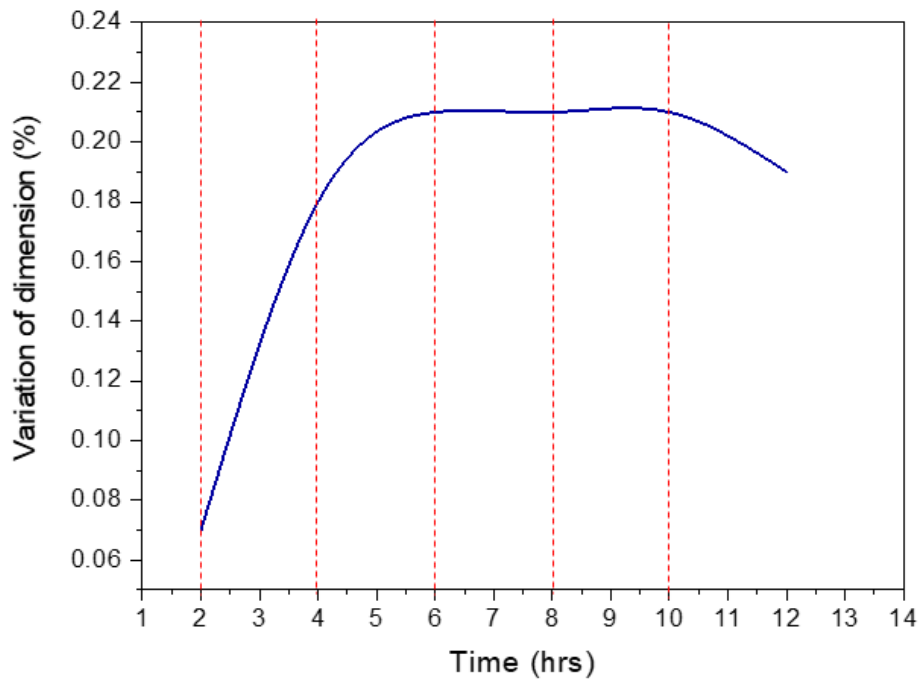
Figure 5.1 Length changes of the printed samples immersed in distilled water at 36 °C

The dissolution of the water-soluble fraction added to the acrylic resin is a slow procedure. Firstly, solvent molecules slowly diffuse into the binder to produce a swollen gel. If the molecular interaction is large because of cross-linking, crystallinity, or strong hydrogen bonding, then swelling of the binder occurs [1] (figure 5.2).
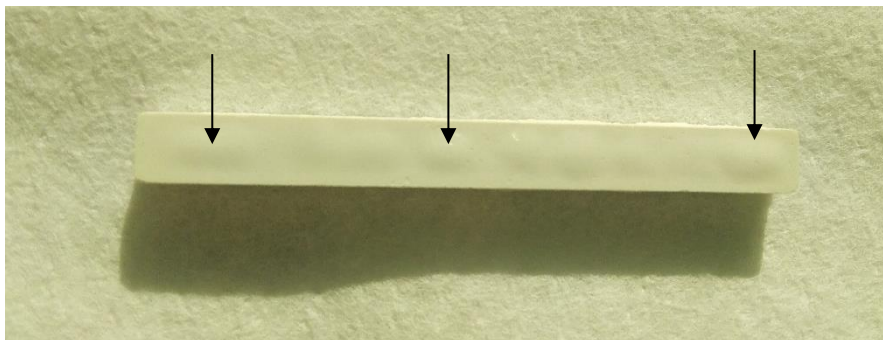
Figure 5.2 Effect of the swelling of the binder after water debinding

An incorrect water debinding may lead to incomplete removal of the water-soluble organic matter and, as a consequence, during the next thermal debinding step, the formation of defects could occur due to the gases released during the burnout of the binders provoking excessive thermal stress of the sample.

The absorbed water content could be defined as equilibrium water content (EWC). The dissolution starts when the water concentration in the soluble polymer is larger than the EWC of the soluble polymer. The water content decreases with the depth of the sample because the water diffuses from the outside to the inside through the porosity. New pores continue to form as water penetrates into the interior of the specimen gradually providing more binder-solvent interfaces. When the water reaches the bulk of the sample (after 5 h) the equilibrium polymer-water content is reached. Once the sample is removed from the bath, the insoluble binders remain inside; the pores formed during the dissolution of the water-soluble polymers can be used as escape paths for decomposition gases during the thermal debinding process.

Common water-soluble binders include polyethylene glycols, polyethylene oxides, polyvinyl alcohols, starches, and polyacrylamide [1–4]. For the sake of clarity, it should be specified that the type of water-soluble component present in the commercial Admatec resin is unknown. The penetration capability of the water depends on the bonding elements and their chemical interactions. Water is effective in removing these polymers since they contain monomers that include oxygen and nitrogen, which are hydrophilic. Water debinding time is related to the nature of the ceramic powder and the particles' dimension, the water temperature and circulation, and to the geometry of the green parts. Printed parts made with powders of larger grain size are faster and easier to debind using aqueous solvents than parts made with finer powder since there is more space between the particles. The water temperature is fundamental for the flow and mobility of polymers, the binder removal rate is enhanced by increasing the water bath temperature. On the other hand, a too fast removal may negatively affect the mechanical strength and warping such as bending can appear. Therefore, high bath temperatures during water

debinding are counterproductive [4]. In figure 5.3 an example of the delamination that occurs after water debinding is illustrated.
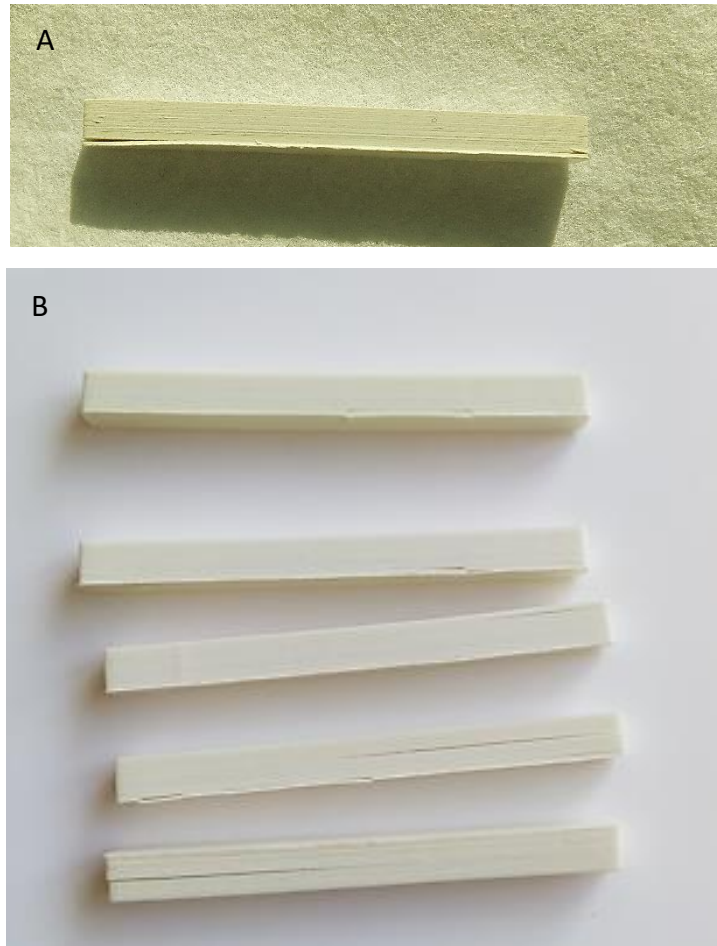
Figure 5.3 Delamination occurred after water debinding before sintering (A), and after sintering (B)

In-depth bibliography research was done in order to find an alternative solvent, in place of water, compatible with the acrylic resin, the stereolithographic process, and the characteristics of the printed parts. Besides the water, mild organic solvents were tested, in particular DBE (dibasic ester), isopropanol, and ethanol. However,

DBE also caused the delamination in the early stages of the soaking of the samples preventing further studies (figure 5.4).
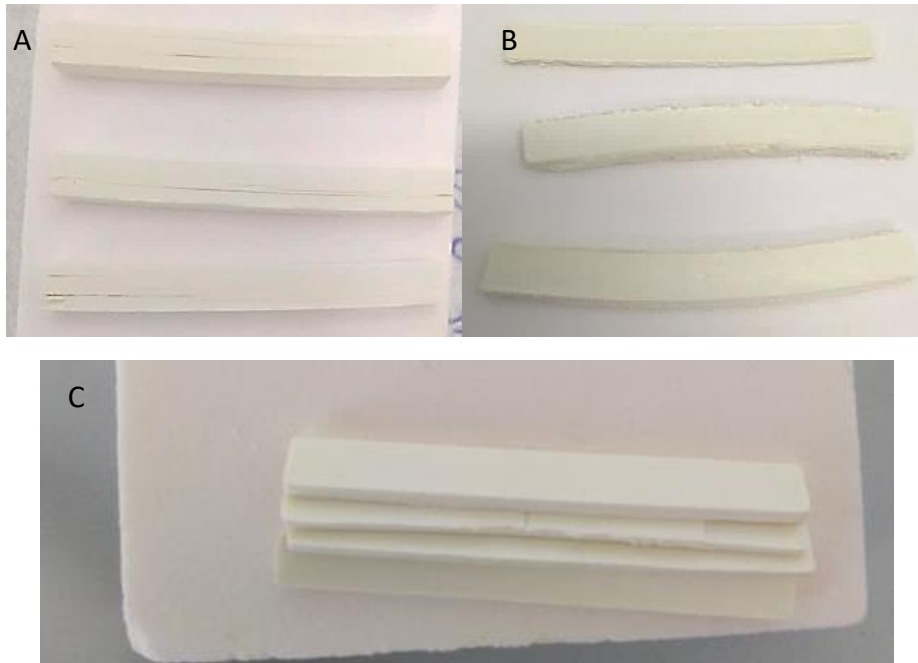
Figure 5.4 Defects caused by the debinding with isopropanol: A) delamination, B) warping. Severe delamination after debinding with DBE: C)

At this point, water debinding resulted the best option, it was preferable to organic solvent debinding because much safer for the health of the operator and more sustainable from the environmental point of view, as well as more effective for some binder polymers.

Even if the delamination also occured with water debinding (figure 5.4), it was maintained under control and considerably reduced by optimizing the printing parameters such as the led power, the thickness of the layer, and the exposure time. The optimum of these three printing process variables was found also with the help of the PCA (chapter 4). Furthermore, from the study of the dimensional variation

(figure 5.1) of the soaked samples in water, it is clear that, after an initial expansion, the length remains unchanged. In order to be sure that the removal of the water-soluble polymers was complete, the samples were soaked for 24 hours. Then, if the adhesion between the layers is not strong enough delamination occurs with severe consequences on the mechanical properties of the final sample. Once the samples were removed from the water, they were inserted in a glass desiccator in the condition of constant humidity to allow the gentle evaporation of the water from the pores.

Finally, the samples were oven dried at 60 °C for 6 h in order to be sure that all the water was removed, and the samples were completely dry.

5.1.2 The thermal debinding

Thermal debinding was performed in a high-temperature electric furnace (Carbolite 1200, Carbolite Gero GmbH) under air atmosphere, according to the thermal cycle depicted in figure 5.5.

The very slow heat treatment was tailored to the decomposition behaviour of the resins studied by TGA-DTA analysis (chapter 4). The dwells were fixed where an exothermic or endothermic peak was present, in order to prevent cracks during resin decomposition.

The evaporation of degradation products can cause pressure build-up within the green body and create voids at its center, bloating, and cracks at its surface if thermal debinding is carried out hastily. [1]

The sintering behaviour of the printed bars was investigated by dilatometry analysis and grain size study, as discussed in section 5.2.
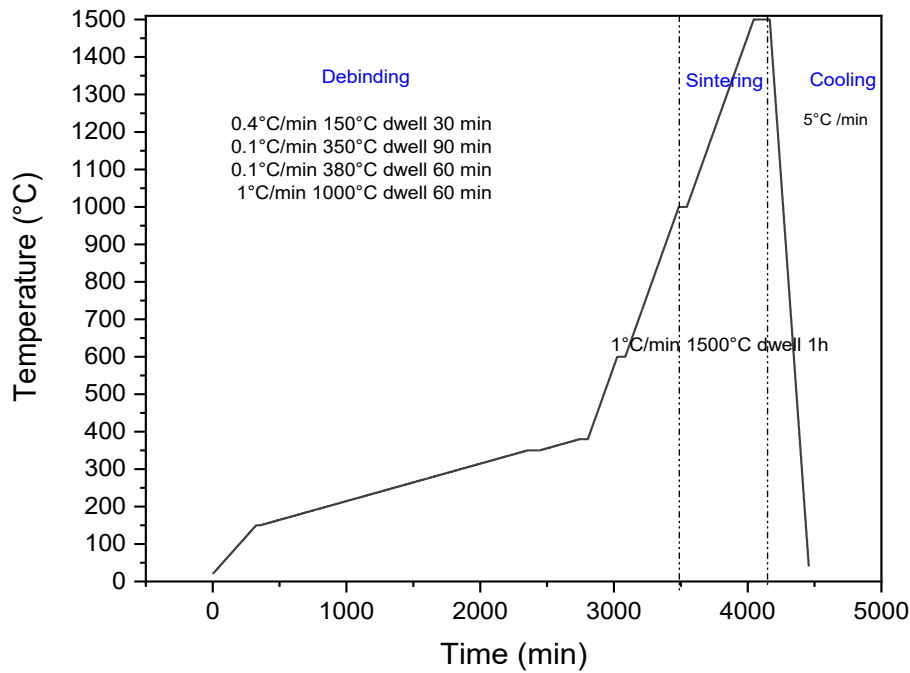
Figure 5.5 Thermal debinding cycle

5.1.3 Printing defects

The stereolithography process produces 3D objects by stacking layers one on top of the other. This interface might not be problematic during green, but during thermal treatment, it can lead to cracks and delamination due to the amount of organic binder that, during the thermal decomposition step, brings to the formation of defects. The printing defects can be classified into two types according to the printing plane direction. One type of defect is the crossing crack being perpendicular to the printing plane [5]. The other defect is the delamination parallel to the printing plane. The delamination occurs because the particle packing density between two layers is lower than that within layers and by the peel force/separation force during lifting of the platform of the printer. The delamination arises also due to an insufficient adhesion between the layers if the penetration depth of the UV radiation is less than the layer thickness [6]. Crossing cracks may occur due to the

shrinkage between the cured layer adhering to the platform or to the previously cured layer, leading to tensile stresses. Furthermore, the printed samples are inhomogeneous due to the presence of the ceramic powders; for this reason, the path of the decomposed species is tortuous and lead to a non-isotropic shrinking during the sintering [7]. Residual stresses generated during printing can be responsible for creep distortions which may cause cracks and delamination thus affecting final accuracy and quality of specimens [8]. The samples printed with the DLP-stereolithography showed only delamination as an issue to be managed but vertical cracks were never observed (figure 5.6). In this case, the delamination defects could have been caused by not suitable printing parameters that lead to insufficient adhesion between the adjacent layers.
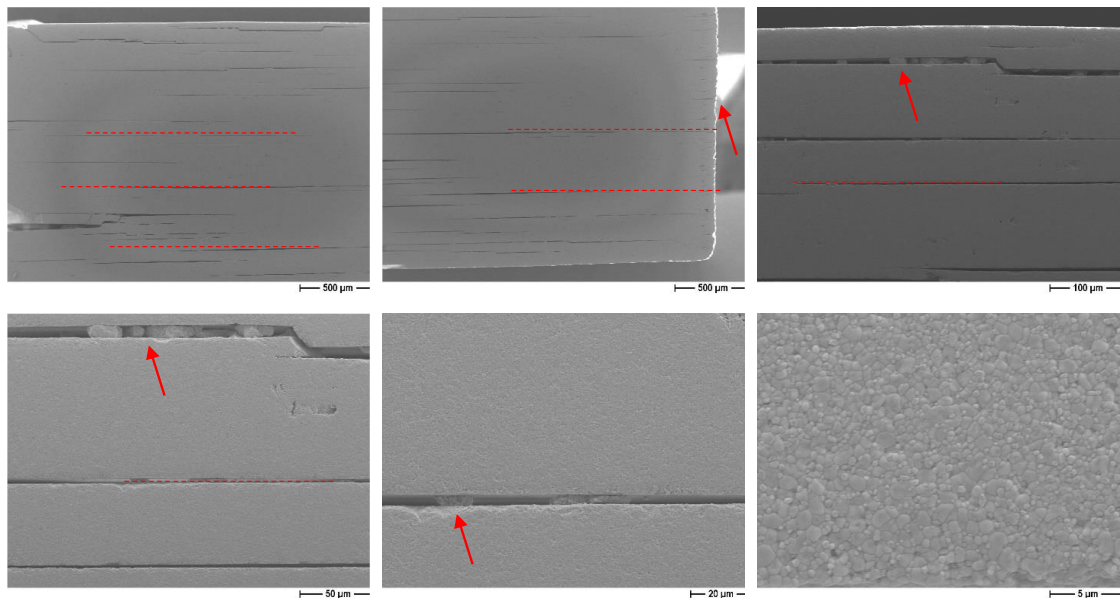
Figure 5.6 Cross-section micrographs of delaminated sintered samples

5.2 Phase and microstructural characterization of the printed parts

The sintering behaviour of the green bodies was investigated by dilatometric analysis by comparing pressed and printed $Ce_{11}ZA_{16}$ bodies (figure 5.7). The printing process may induce some variations in the thermal behaviour of the samples. Typically, the printed materials exhibit larger shrinkage compared to the pressed ones.

It can be seen that the printed sample was characterized by a lower green density as compared to the pressed one: a different interaction between the resin and the ceramic powder could influence the particle packing. The lower green density of the printed parts, 43.7 ± 1 %TD with respect to 46.5 ± 0.7%TD for the pressed parts (mean value calculated on 5 samples) leads also to a slightly higher temperature at which the maximum sintering rate happens, equals to 1245 °C [9] for printed materials, compared to 1225 °C for the pressed ones (figure 5.7B).

For dilatometry measurements, a heat treatment program was carried out at a heating rate of 5 °C/min from ambient temperature up to 1550 °C, a dwell time of 1 h, and a cooling rate of 5 °C/min down to the ambient temperature. The samples for dilatometry analysis were prepared by pressing 1 g of $Ce_{11}ZA_{16}$ powder, poured into a 17 x 5 mm^2 rectangular die, using a 15 Ton *Specac* manual hydraulic press with a pressure of 0.1 MPa.

The green density was evaluated by the geometrical method while the fired density was assessed by the buoyancy method. The main data obtained by the dilatometric study of printed and pressed bodies are collected in Table 5.1.
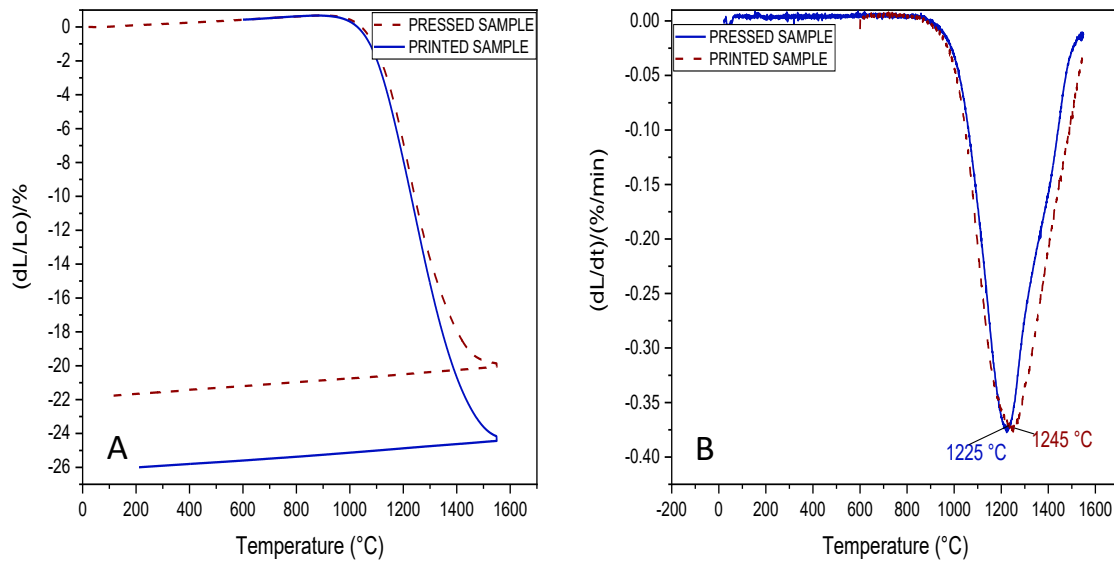
Figure 5.7 A-B Comparison of a *Ce₁₁ZA₁₆* pressed bar (dotted red line) and a printed one at 73 wt% of solid loading (solid blue line). Dilatometric (A) and derivative (B) curves.

A linear shrinkage of about 26% and 22% was found in the printed and pressed sample, respectively. The printed sample showed a lower green density. The presence of the acrylic resin and the dispersant among the ceramic particles could affect the particle packing in the forming step and during the sintering as well, even if the results are almost superimposable up to a certain temperature.

For the printed specimen the onset sintering temperature was detected at about 1050 °C and the inflection point was identified at 1245 ∘C. A slightly lower onset temperature, equal to 996 °C, was detected for the pressed one with an inflection point at 1225 °C. The sintered densities of 97.8 and 100 TD% were respectively yielded for printed and pressed samples.

For the printed samples, the densification is not complete whereas, for the pressed one, full densification was achieved. It can be stated that the stereolithographic process has an effect on the sinterability of the composite powder, in accordance

with the literature [10], because if defects are formed during the printing than cannot be eliminated anymore during the following steps.

This discrepancy may be the result of the ceramic particles organization and porosity size/distribution due to the shaping technique applied and to the removal of the organic matter during the debinding step. The densification of printed ceramics sintered at 1500 °C for one hour was however excellent.

On the ground of these results, the most appropriate sintering conditions of printed materials were fixed at 1500 °C for 1 h in order to limit the grain growth.

Sample	Green density (TD%)	Fired density (TD%)	T_{onset} (°C)	T_{max} (°C)	Total linear shrinkage (%)
Printed	42.4	97.8	1050	1245	26
Pressed	46.5	100	996	1225	22

Table 5.1 Data determined by the dilatometric study of $Ce_{11}ZA_{16}$ printed and pressed bodies sintered at 1550 °C for 1 h

The microstructural evolution and sintering behaviour of $Ce_{11}ZA_{16}$ was studied again on a 73 wt% solid loading printed bar by means of dilatometric analysis after thermal debinding treatment (figure 5.8). On the dilatometric curve and its derivative four significant temperatures of the sintering cycle were selected: 1000 °C, the sintering onset temperature, 1170 °C, corresponding to ~ 5 % less shrinkage than the maximum shrinkage rate, 1300 °C, equivalent to ~ 5 % greater shrinkage as respect to the maximum shrinkage rate, and 1500 °C, that matches with ~ 98 % of the total linear shrinkage.

At these representative temperatures, the fracture surface of $Ce_{11}ZA_{16}$ printed samples was analysed through Field Emission Scanning Electron Microscope (FESEM) in order the study the microstructure evolution step by step (figure 5.9). At 1000 °C a homogeneous microstructure, devoid of significant flaws, can be observed. At higher magnifications, 100–200 nm particles can be observed,

coherent with the starting particle size distribution. No agglomeration can be observed, indicating that the three initial powders' homogeneous and fine dispersion was maintained after being introduced to the polymeric component. From 1170 °C to 1500 °C the printed layers take shape. At 1170 °C, at higher magnification, limited grain growth, with particles of 150–300 nm, was noted. At 1300 °C and 1500 °C, due to their differing sizes, α-Al_2O_3 and Ce-ZrO_2 particles might be discerned because of larger zirconia grains.

At 1300 °C, grain development was still constrained with an average particle size of ~ 250 nm and ~ 450 nm for alumina and zirconia, respectively. From 1300 °C to 1500 °C the grain dimension increases in an important way generating particles of ~ 1 μm and 0.5 μm for zirconia and alumina, respectively.

The fired theoretical density (TD%) was 51.0 % at 1170 °C, 69.6 % at 1300 °C, and 95.5 % at 1500 °C. A layer thickness of approximately 11 μm was measured at the end of the sintering.
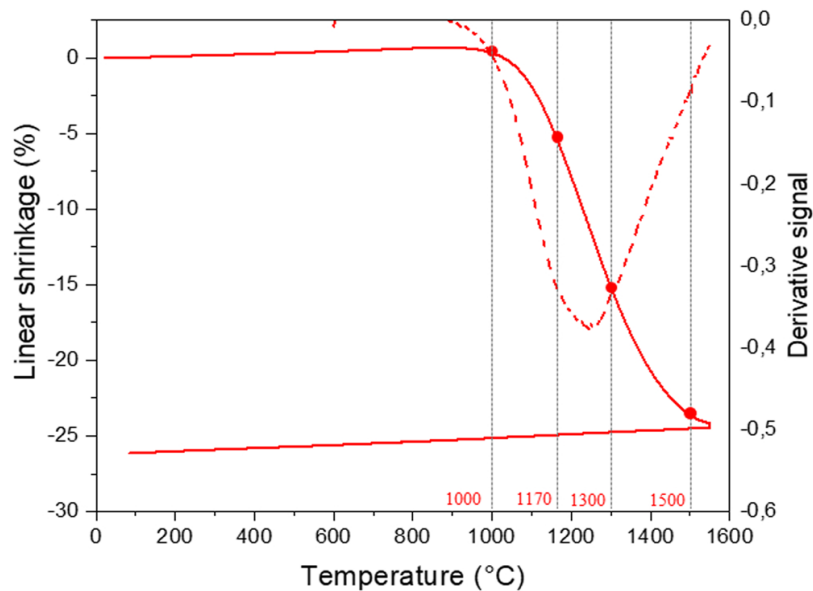
Figure 5.8 Dilatometric curves: linear shrinkage (solid line) and derivative (dotted line) of a 73 wt% printed bar.
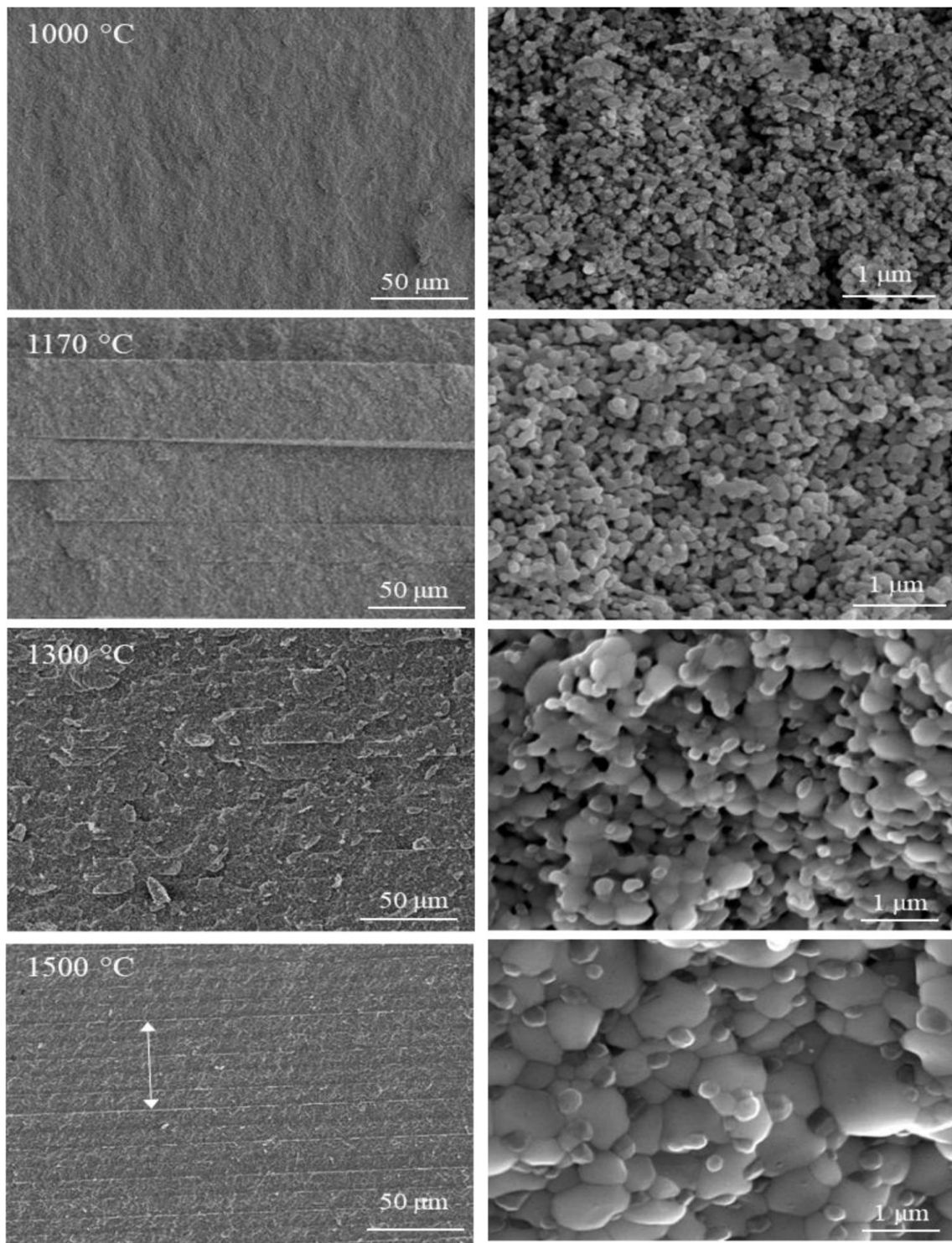
Figure 5.9 Microstructural evolution of printed samples with formulation 73 wt% +2.5 Disperbyk-103 fired at different temperatures.

5.2.1 Grain size - solid loading relationship of $Ce_{11}ZA_{16}$

As discussed in Chapter 1, density, grain size, and homogeneity are the main features of the ceramics' microstructure. A high density is an important parameter since a low density, most of all if open porosity is present, leads to material cohesion losses, and the decrease in mechanical properties can be dramatic [11]. It is widely recognized the beneficial effect of reducing the grain size on the ageing kinetics [12] but an excessive reduction leads to a decrease in toughness and slow crack propagation threshold due to a less effective phase transformation toughening [13]. Ceria-doped zirconia ceramics show exceptional toughness (up to 20MPa $\sqrt{m}$) and are less sensitive to aging (due to the tetravalent nature of cerium ions). According to the literature, the grain size of a fully dense Ce-TZP is typically above 1.5–2 mm and this is one of the principal disadvantages of this material as compared to Y-TZP which exhibits grain size lower than 0.5 mm and higher strength (1000 MPa for a fully dense material against 600 MPa for CE-TZP) [14].

The effect of the grain size on transformation and on transformation toughening has been explored on 12 mol% Ce-TZPs.

It was found that the temperature for the t-m transformation, the transformation zone size, and the transformation toughening, all increase continuously with grain size. Furthermore, a grain-localized tensile stress can promote the t-m transformation, this factor is influenced by the mismatch strains at grain boundaries due to the difference in the thermal expansion coefficients in the c- and a-axes of the tetragonal phase. This anisotropy increases with an increase in grain size [15]. Larger grain size diminishes also the flexural strength [16][17] (the relationship between grain size and mechanical properties in Ce-TZP ceramics is explained in detail in chapter 1.1.1).

In order to study the evolution of the zirconia and alumina grain size, FE-SEM micrographs of samples at different solid loadings were collected. In detail the formulations with 68 wt%+1.5 Disperbyk-103, 70 wt%+2 Disperbyk-103, 73

wt%+2.5 Disperbyk-103, and 78 wt%+2.5 Disperbyk-103 were printed and sintered both at 1500 °C/ 1h and 1550 °C/1h and studied. The aim was to evaluate the influence of the solid loading and the sintering temperature on the zirconia and alumina grains' growth.

The specimens were polished, using SiC discs up to P1200, and thermal etched specimens were analysed after being sputter-coated with gold for 2 minutes to prevent charge accumulation.

The average grain size was evaluated by ImageJ software using the linear intercept method. For each phase, ~ 300 grains were measured. From the FE-SEM micrographs, a good distribution of the zirconia and alumina phases can be observed. Alumina grains showed a sub-micrometric average size at all solid loadings investigated, and at both 1500 °C and 1550 °C. Zirconia grains showed larger size distributions but free of abnormal growth. Alumina grains were mostly present at ZrO_2 grain boundaries, as expected. In general, fine ceramics typically have a low coefficient of thermal expansion; among these materials, zirconia shows the highest value, 10 x 10^{-6}/°C while alumina shrinks less, 8 x 10^{-6}/°C [18]. The thermal expansion's mismatch between zirconia and alumina strengthened the material by inducing residual stresses.

In figure 5.10 A and B, it can be noticed that from 1500 °C to 1550 °C an increase in the particle size was revealed for the two phases.

On the contrary, a progressive decrease of both alumina and zirconia particle size by increasing the solid load was detected. This result could be due to the higher stress concentration in the samples because of the above cited mismatch in the respective coefficient of thermal expansion. Further studies should be done to investigate the exact reason, but this phenomenon was observed, for example, during high pressure sintering of alumina [19].

In the samples made from slurries with lower solid loading (68 wt% and 70 wt%), the binder volume to remove is higher and, as a consequence, the packing density is reduced. After the debinding treatment, voids were left behind in the microstructure and the interparticle distance is greater limiting the diffusion gap

and the points of contact [20]. The contact points are necessary for the starting neck growth through surface diffusion, followed by grain growth and pore rounding. The relatively minor lower contact points postpone the densification since the shrinkage and densification happen through grain boundary and volume diffusion phenomena and not surface diffusion. On the other hand, at higher solid loadings (73 wt% and 78 wt%), the packing densities increased leaving smaller voids and lesser pores between particles allowing the achievement of higher densities (for both the green and the sintered parts) [20]. As assessed in the literature, solid loading is a key factor that affects the physical and mechanical properties of printed parts [21]. As observed by Xia et al. with a higher solid loading they observed a better grain size "consistency" [21]. Probably, these concurrent physical phenomena during sintering lead to this discrepancy in the zirconia grains' growth.

This phenomenon is more evident for the zirconia grains that, on equal terms, passing from a 68 wt% to a 78 wt% slurry, the ZrO_2 grains dimension decreased by 27.7% and 28% at 1500 °C and 1550 °C respectively. For the alumina grains, less noticeable grain growth can be detected; from 68 wt% to 78 wt% slurries, the Al_2O_3 grains dimension decreased by 25.9% and 25% at 1500 °C and 1550 °C respectively. This is a further confirmation of the beneficial effect of the augmentation of the slurry's solid load that, as well known, strongly influences the curing behaviour, and the microstructure of the ceramic core. A high-solid loading slurry can successfully enhance the sintering densification of ceramic particles, interlayer bonding strength, and mechanical properties [22] [23].
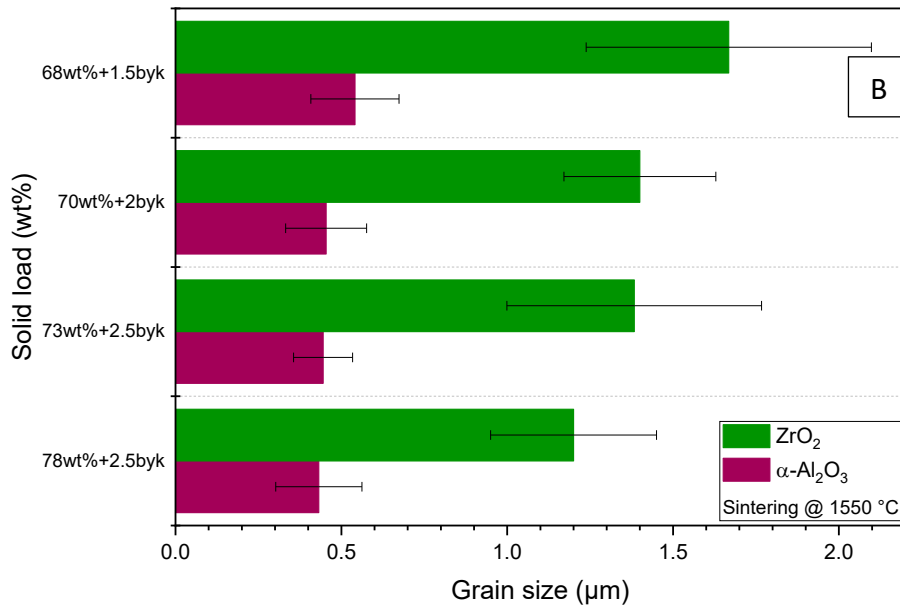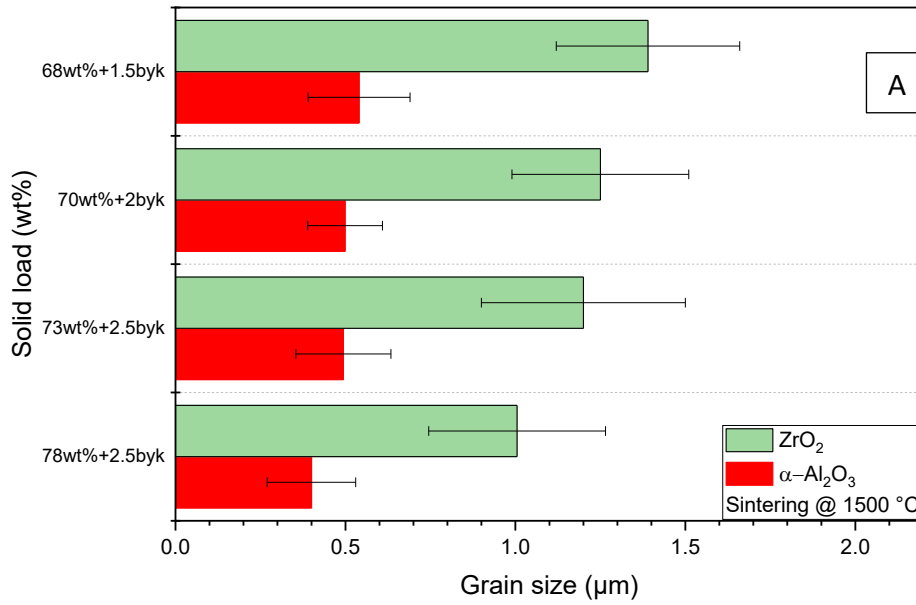
Figure 5.10 Al$_2$O$_3$ and ZrO$_2$ grain size at increasing solid loadings sintered at 1500 °C (A) and 1550 °C (B)

On the basis of the rheological properties, the curing behaviour of the slurries, and the PCA analysis, as discussed in detail in chapter 4, the formulation 78 wt% + 2.5 Disperbyk-103 was identified as the most promising formulation. The study on the grain size is a further confirmation. At 1500 °C, the grain growth was moderate; this should be favouring the mechanical performances. For this reason, the bending strength was performed on printed bars fired at this temperature (see next section). FE-SEM micrograph and related particle size distribution of the 78 wt% + 2.5 Disperbyk-103 formulation are depicted in figure 5.11. A good distribution of the two phases can be appreciated. Zirconia grains were bigger compared to alumina ones, this last phase was also characterized by a narrower grain size distribution, as expected, considering the very good dispersion achieved.
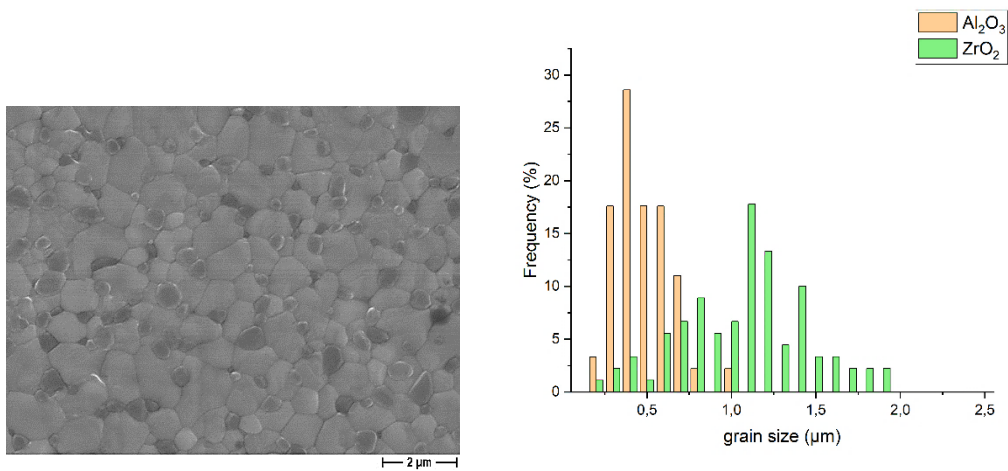
Figure 5.11 FE-SEM micrograph of *Ce₁₁ZA₁₆*, at 78 wt% of solid loading, and related grain size distribution. Sintering at 1500 °C

5.3 Mechanical characterization

In this section, the mechanical properties of $Ce_{11}ZA_{16}$ are determined by means of Vickers hardness and three-point bending tests.

At the beginning of each paragraph, a brief description of the characterization techniques and the samples preparation process is presented too.

$Ce_{11}ZA_{16}$ printed samples were sintered at 1500 °C for 1 h and are characterized by a high fired density (99.8 TD%) and a low monoclinic volume content (<1%).

5.3.1 Vickers hardness

Vickers hardness was measured with a diamond pyramid with 90° base angles and a 136° face angle. The hardness was measured following the ASTM E384-17 Standard Test Method for Microindentation Hardness of Materials, and the hardness value was calculated with the equation:

$$Hv = \frac{1.8544 \cdot P(Kgf)}{d2(mm2)} \tag{1}$$

where d is the mean length of the two imprint diagonals and P is the force in Kg_f. All the measurements were performed with a load of 1 kgf with 15 seconds of holding time.

A MicroMet 6000 Series Buehler equipment was employed. The hardness unit recognized is Vickers Pyramid Number (Hv).

For the preparation of the specimens, printed and sintered bars were embedded into an acrylic resin and the surfaces were polished down to 1 μm.

As reported by Chinn [24], the use of the resin doesn't influence the hardness values for test loads up to 30 kgf. With the aim to obtain two perfectly plane surfaces both

faces of the resin were polished. A series of 20 indentations were performed on each sample.

The imprints were investigated with the optical microscope Leica DMI 5000 M. In order to have correctly performed hardness measurements, special care was taken to the indentation shape and dimension. The lengths of the diagonals should not deviate more than 5% from each other, the distance between indents should be a minimum of three times the diagonal length and the thickness of the sample should be at least 1.5 times the diagonal length of the indentation (figure 5.12).
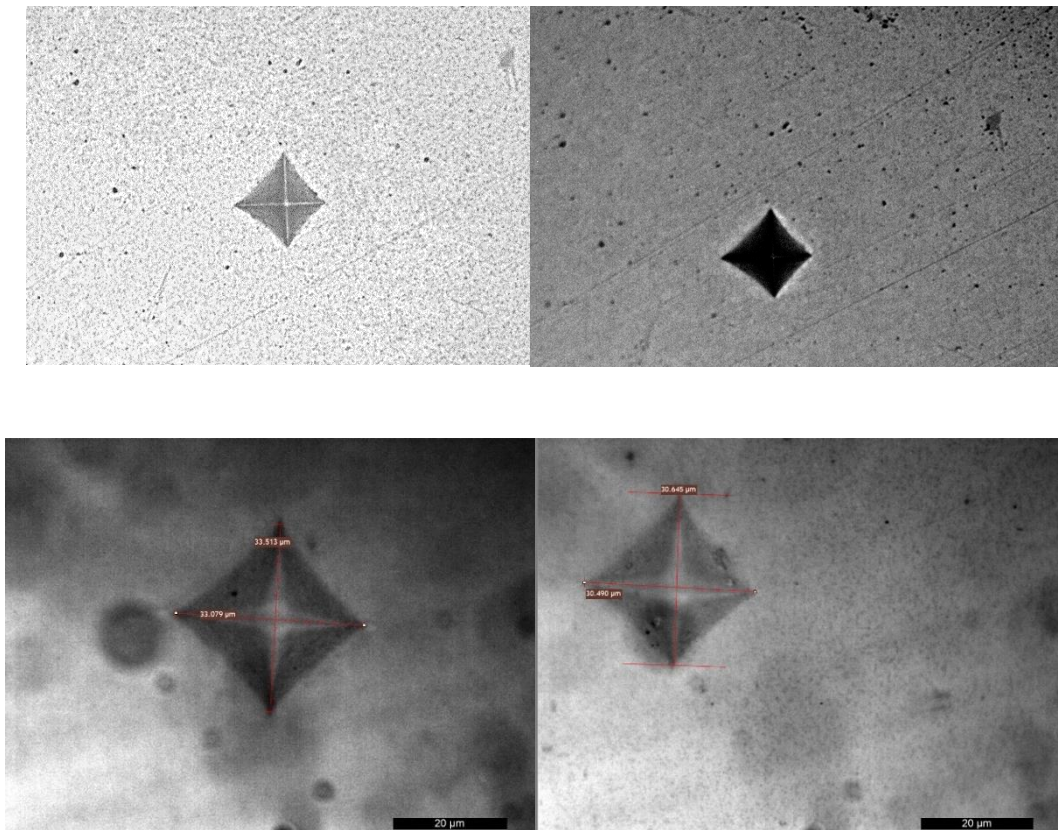
Figure 5.12 Images of the 1 kg$_f$ indentations on $Ce_{11}ZA_{16}$ composite

The Vickers hardness mean value of the $Ce_{11}ZA_{16}$' bars sintered at 1500 °C was 15.3 ± 0.6 GPa obtained by measuring 20 indentations. In table 5.2, according to the literature, Vickers hardness of zirconia-based materials are reported.

Hardness (GPa)	Material	Load (N)	Technique	TD (%)	Mean grain size (µm)	Reference
9.8-10.6	ZA_8Sr_8 (Ce 10 to 11.5)	300	Slip cating	>99.9	0.6 ± 0.2 ($CeZrO_2$) 0.3 ± 0.1 (α-Al_2O_3)	[25]
11-12	Ce-TZP/30 vol% Al_2O_3 composites	490	Isostatic pressing	//	0.9 (ZrO_2)	[26]
15-21	AZ85	4.9 (500 gf)	sla	99.2	0.61 ± 0.19 (ZrO_2) 0.65 ± 0.27 (Al_2O_3)	[27]
16.2	ZTA	9.8	sla	96.6 ± 0.6	1.36 ± 0.64 (Al_2O_3) 0.55 ± 0.18 (ZrO_2)	[28]
17.76	ZTA	98	sla	99.5	1.08 (Al_2O_3) 0.35 (ZrO_2)	[29]
12.14	(3Y-TZP) (Fe_2O_3) doped	98	sla	99.2± 0.01	0.46	[30]
13.06	ZrO_2	98	sla	97.14	//	[31]

11.24-12.5	Y-TZP	196.1	sla	99.44	≤ 0.4 (ZrO_2)	[32]
12.75	Ce-TZP	49	sla	98.9	0.42 ± 0.01	[33]
16	ZrO_2	//	sla	//	>0.5-1.8<(Al_2O_3)	[34]
6.2	10Ce-TZP	490	Slip casting	//	1.2 (ZrO_2)	[35]
10 ± 0.1	10 Ce-TZP/15α-Al_2O_3	294	Slip casting	96.5 ± 0.1	0.54 ± 0.06	[35]
13.525 ± 2.556	CeZTA_50	0.001	Hydraulic press	//	//	[36]
12.75 ± 0.15	Ce-TZP	49	Sinter-HIP	98.9	0.42	[37]
15.3±0.6*	$Ce_{11}ZA_{16}$	98.1	sla	99.8	1±0.2 (ZrO_2)	This work

Table 5.2 Vickers hardness of zirconia-based materials

5.3.2 Three-point bending test

The flexural strength of the printed bars was evaluated by three-point bending (3PB). Prior to the 3PB the specimens were not machined but tested as printed, without further polishing. The main goal was to measure the bending strengths values of the printed parts process-dependent and sensitive to defects generated during the stereolithographic technique. Before the 3PB tests, the samples were submitted to XRD analysis; all showed a monoclinic volume fraction < 5 vol% on the upper surface of the printed bar, namely that subjected to compressive stress.

Monotonic loading tests up to failure were performed using a 20 mm span. The tests were carried out using a testing machine (Zwick Roell) equipped with a Linear Variable Differential Transformer (LVDT) in displacement control mode. The load was measured thanks to a 50 kN force sensor under the loading pin. All mechanical tests were performed at room temperature (22 ± 2∘C) in air.

The flexural strength in MPa was calculated with the equation:

$$\sigma = (3 \times F \times L) / (2 \times W \times H^2) \tag{2}$$

where F is the maximum force to failure (N), L is the distance between the lower supports (mm), W is the sample width (mm), and H is the sample height (mm).

Ten printed samples (78 wt% + 2.5 wt% Disperbyk-103) of dimensions $25 \times 2 \times 1.5$ mm^3 (L x W x H) sintered at 1500 °C/1 h were tested.

Young's modulus was calculated from the linear slope of the load-displacement curves obtained. The samples exhibited a bending strength of 436 ± 28 MPa and a Young's modulus of ~200 ± 19 GPa. In table 5.3 different bending strength values of 3D-printed alumina-zirconia composites are reported.

The comparison between different literature data could be very difficult since the final results strongly depend on the applied test, the sample preparation, the solid load, the printing parameters, and so on. As can be observed, the literature values are slightly higher compared to this work, but all the specimens were chamfered and mirror-like polished before the mechanical test in order to remove superficial flaws. In our case, the bars were tested as printed in order to study and improve the reliability of the printing process and fully exploit the high potential of DLP-stereolithography.

The obtained values evidence the sample's consistency and low surface defect rate. Since the material is very sensitive to processing flaws and delamination, by continuing the work on the printing process, there are good assumptions so that in the future the bending strength values could increase.

Composition	3D Printing method	Test method	Fired density (TD%)	σ (MPa)	Pre-treatment	Ref.
48 vol% Al_2O_3-ZrO_2	LCM-DLP	4 PB	98.5	574	edges of the tensile side were chamfered	[38]
Mass ratio (Al_2O_3: ZrO_2) 3:1	DLP	3PB	99.4	516.7	not declared	[39]
Ce–ZrO_2/Al_2O_3	SLA	3PB	//	530.25	polished	[40]
3Y-TZP	Material jetting	4PB	99.7	733 ± 152	chamfered and mirror-polished bars	[41]
$Ce_{11}ZA_{16}$ 78 wt% + 2.5 Disperbyk-103	SLA	3PB		436 ± 28	none	This work

Table 5.3 Bending strength data of 3D printed materials from the literature

In figure 5.13 the bending strength values versus the fired density (TD%) are plotted for the compositions 70 wt%, 73 wt%, and 78 wt%. While all the compositions show a rather high densification, the bending strength increases as the solid loading also increases demonstrating the beneficial effect of a higher solid load. It is eloquent how as the density increases, the defects decrease, mechanical strength increases, and the distribution of MOR values is reduced.
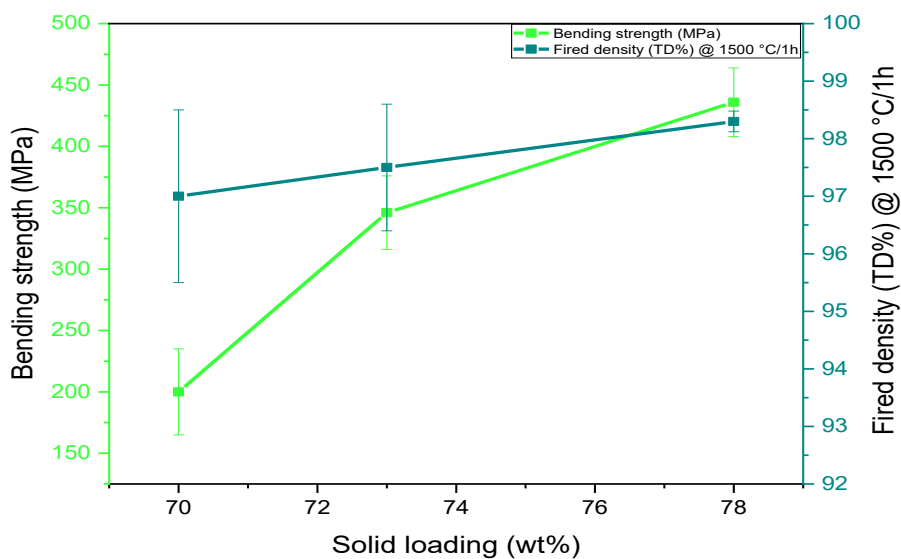
Figure 5.13 Bending strength vs fired density TD%) at different solid loading

5.3.3 Phase characterization of $Ce_{11}ZA_{16}$

With the aim to investigate the phase composition, 78 wt% + 2.5 Disperbyk-103 printed samples were submitted to XRD analyses, as shown in figure 5.14.

The phase composition was determined by X-ray diffraction in Bragg-Brentano configuration (X'Pert Powder DY 3539), in the 5–70° 2θ range. Phases were identified by JCPD file n. 10-0173 for α-Al_2O_3 phase, 82-1398 for tetragonal zirconia stabilized with ceria, and 74-0815 for monoclinic zirconia. The intensities of the monoclinic (−111) and (111) peaks and the (101) tetragonal peak were investigated to calculate the monoclinic zirconia fraction, according to the Toraya [43] method.

Mostly tetragonal zirconia was detected on the polished SLA sample surface meaning that, after sintering, relevant tetragonal zirconia volume fraction was successfully kept at room temperature and only traces of monoclinic one was

178

observed (figure 5.14). Furthermore, the presence of stiffer alumina grains can improve the stability of the tetragonal zirconia phase at room temperature with a constraining effect [44].
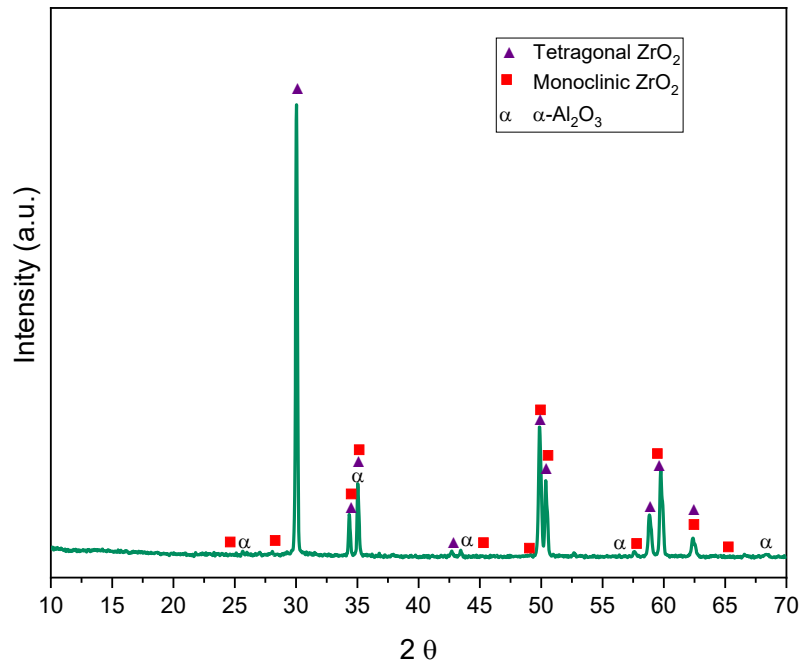
Figure 5.14 XRD pattern of 78 wt% + 2.5 Disperbyk-103 sintered at 1500 °C/1 h

5.3.4 T-m zirconia transformability assessed by Micro-Raman spectroscopy

Raman spectroscopy is a non-destructive technique that allows to analyse a material by irradiating it with a laser spotlight. That incident radiation by interacting with the vibrational levels of matter produces an energy emission at a wavelength different from the one of the incident light. The analysis of the scattering radiation allows to single out at the different energies the components of the vibrational modes related to the constituting chemical bonds. Here, thanks to the coupled

microscope, the technique is adopted to analyse the zirconia transformability performed on sintered $Ce_{11}ZA_{16}$ samples after having indented the surface for measuring the Vickers hardness. Samples with the highest hardness were chosen for the Micro-Raman analysis. This spectroscopic technique allows the evaluation of the occurrence of the tetragonal to monoclinic zirconia transformation in the area around the indentation.

The spectra were acquired with a Renishaw InVia Reflex micro-Raman spectrometer (Renishaw plc, Wottonunder-Edge, UK), equipped with a cooled CCD camera. The Raman source was a 514.5 nm diode laser (Toptica Photonics AG, Gräfelfing, Germany) which a maximum power equal to ~100 mW. Samples inspection occurred in backscattering light collection configuration through a 20x microscope objective (N.A. 0.25). Optical images were acquired with a Nikon Eclipse ME600 microscope (Nikon, Tokyo, Japan).

Mapping mode spectra were acquired with 3 s of exposure time and 3 accumulations for each one, in the 100 - 1800 cm^{-1} range, on a region of 75 × 75 μm^2 with a step size of 5 μm (225 spectra). The spatial resolution of the equipment was ~1 μm.

Before the indentation, the sample was submitted to X-ray diffraction (XRD) measurements that exhibited pure tetragonal peaks on the polished down to 1 μm and as-sintered surface.

The spectral map analysis was performed by means of the Renishaw WiRE 3.2 software. At first, the indentation area was mapped by creating the 15 x 15 (points) grid. Each spectrum was collected at the crossing points of the grid axes (figure 5.15). The map analysis was performed in the 100 - 1800 cm^{-1} range where the most significant peaks corresponding to the monoclinic and tetragonal phases are present.
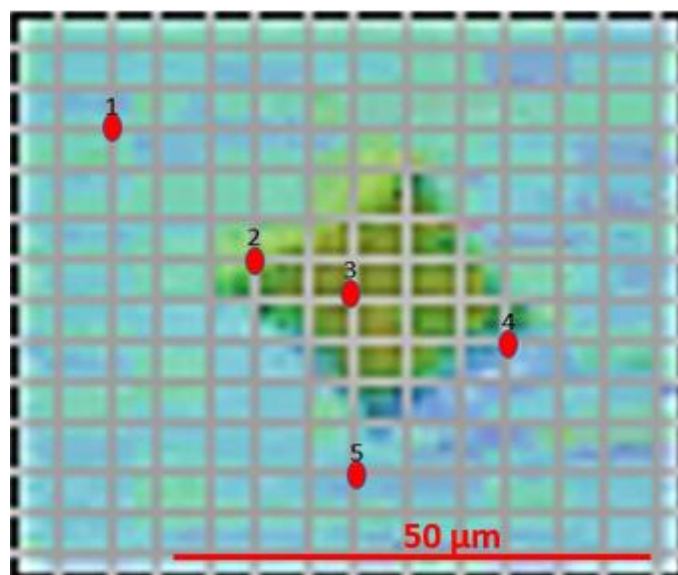
Figure 5.15 Optical microscopic image of the mapped area around the indentation. 225 spectra were recorded by as many points. The red points indicate the most significant analysed locations for the t-m transformation.

After a deep analysis of the collected spectra, the five most representative points were selected (figure 5.15): two close to the edges (points 2-4), one in the centre of the indentation (point 3), and two far from the indented area (point 1-5).

In table 5.4 Raman shift corresponding to the tetragonal and monoclinic phase are reported. Tetragonal phase peaks were assigned at $\sim$ 142, 256, 316, 460, and 635 cm^{-1} [37]. Monoclinic phase peaks were assigned at $\sim$ 178, 190, 375, 534, 559, and 615 cm^{-1} [45]. The α-Al$_2$O$_3$ peak was located near 1400 cm^{-1} [46].

Raman shift (cm^{-1})	
Tetragonal ZrO$_2$	Monoclinic ZrO$_2$
142	178
256	190
316	375
460	534
635	559
	615

Table 5.4 Raman peaks of monoclinic and tetragonal phases [46]

As expected, Raman analyses have shown an increase of the monoclinic ZrO$_2$ content closer and inside the indentation. The spectra showed monoclinic peaks in the points 2-3-4-5) and then decreased drastically at the point 1, ~3 µm far away from the indentation area (figure 5.16).
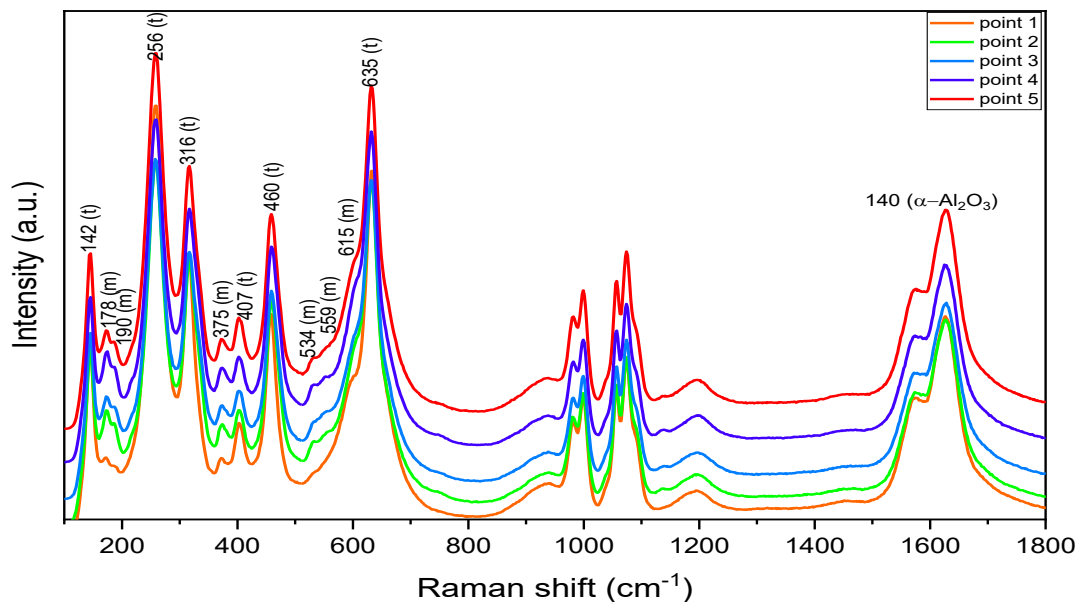
Figure 5.16 Micro-Raman spectra recorded from positions 1-2 (see figure 5.2)

Two-dimensional Raman maps in false colour images underpin what was already seen with the collected spectra; the transformation from tetragonal to monoclinic zirconia phase occurred in the optically observed transformed zones. The highest amount of monoclinic phase was localized at the centre of the indentation and then decreased moving away (table 5.5 - 5.6 - 5.7). The peaks at 256, 466, and 637 cm^{-1} were analysed for the tetragonal phase, while the peaks 178, 190, 375, 534, and 559 cm^{-1} were analysed for the monoclinic one.

Each map is related to a specific peak that is in turn correlated to a specific point of the indentation. Two typologies of maps are compared, rainbow colours based, and red shades. For the former, the increase in the peak intensity corresponds with the toning from blue to red while, for the second, the increase of the peak intensity corresponds to a more intense red colour tone.
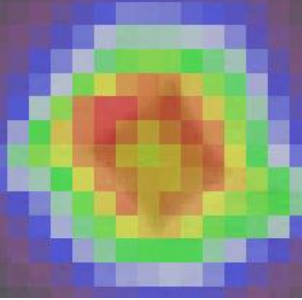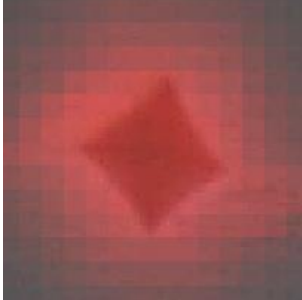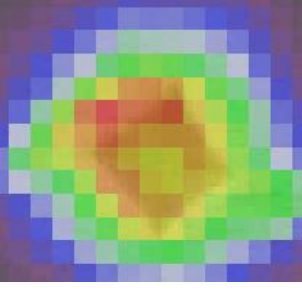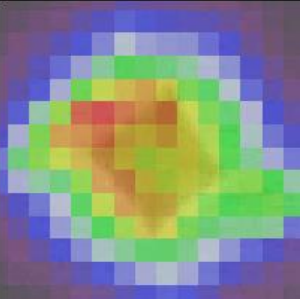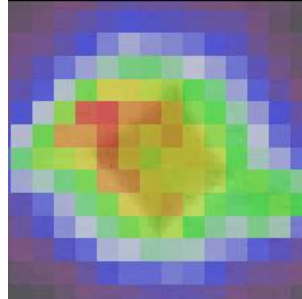
Regarding the false colour maps of the monoclinic peaks, the colour veers to red while gradually approaching the indentation. The opposite behaviour can be appreciated in the false colour maps of the tetragonal peaks, the colour veers to blue while gradually approaching the indentation, meaning that the amount of the tetragonal ZrO_2 phase is very low or zero. For the red maps related to the tetragonal peaks, the colour intensity decreases until disappearance near and inside the indentation. For the monoclinic peaks, an intense red can be detected close to the indentation for then blend moving away from it.

No quantitative calculations were made since the aim was to investigate the t-m transformations from a qualitative point of view.

The martensitic transformation occurs in the area around the indentation creating stress fields in the surrounding material due to volumetric misfit [47].

The maximum phase transformation might be expected just below the indentation. However, the dilatation related to the phase transformation amplifies the residual tensile forces, which in turn enhances subsurface transformation and transformation around the indentation impression, giving rise to higher monoclinic peak intensities [47].

Point	Raman shift (cm⁻¹)	Zirconia monoclinic phase peaks	
1	178		
	190		
	375		
	534		
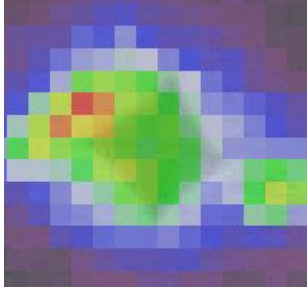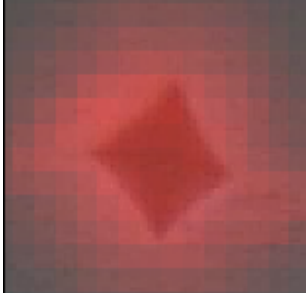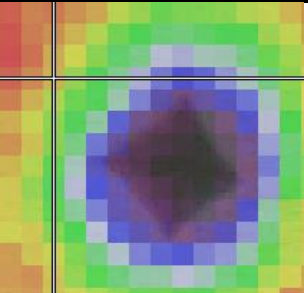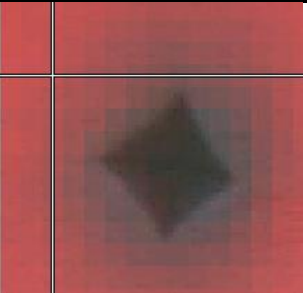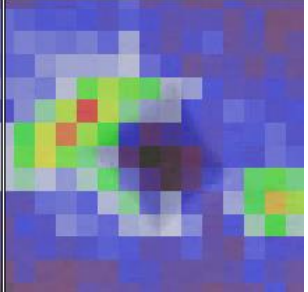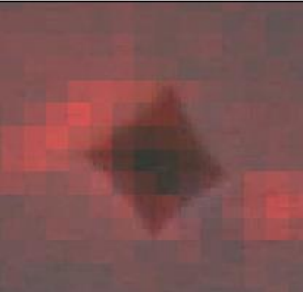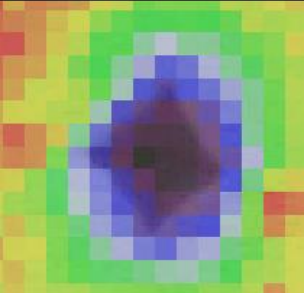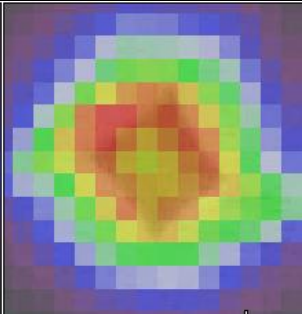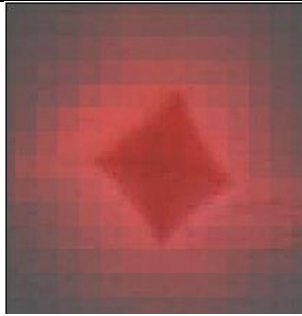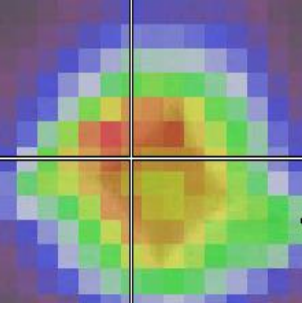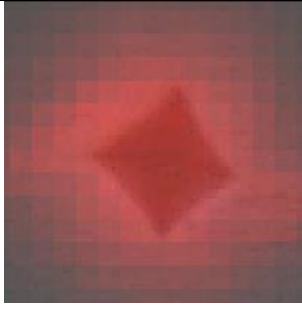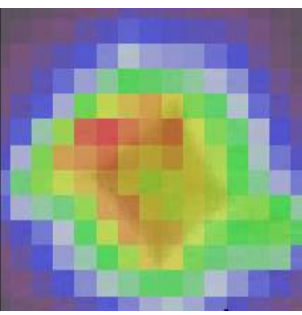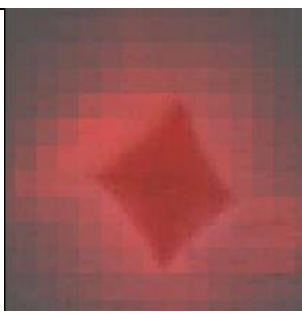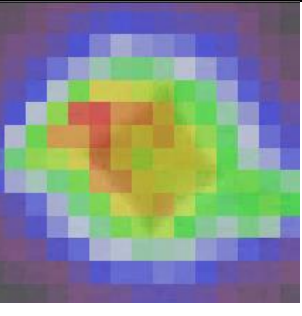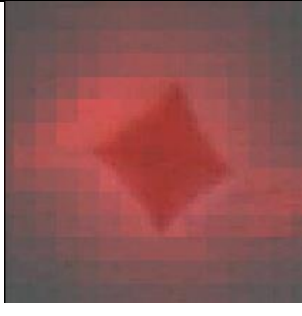
Position	Raman shift cm^{-1}	Zirconia tetragonal phase peaks	
	559		
1	256		
	466		
	637		

Table 5.5 Micro-Raman mapping of the indentation induced phase transformation for a 1 kg indented $Ce_{11}ZA_{16}$ sample at point 1 from the map of figure 5.15

Position	Raman shift (cm^{-1})	Zirconia monoclinic phase peaks	
2	178		
	190		
	375		
	534		

186
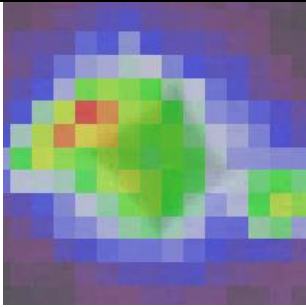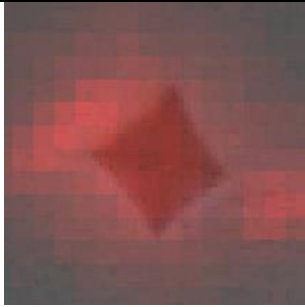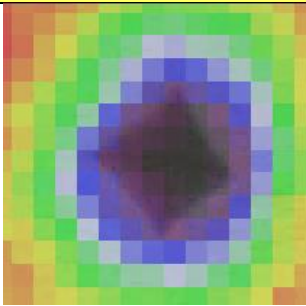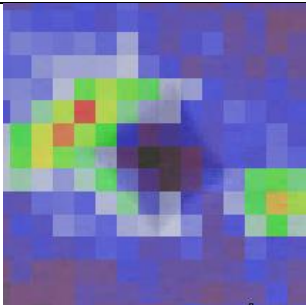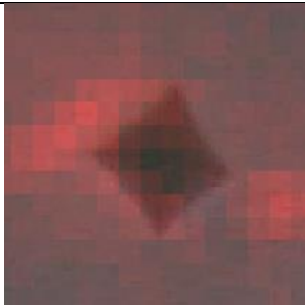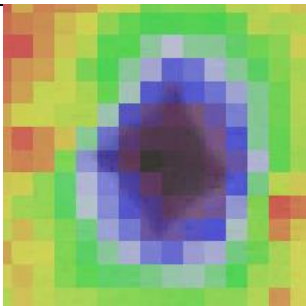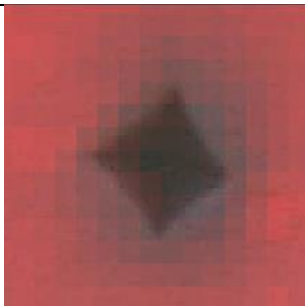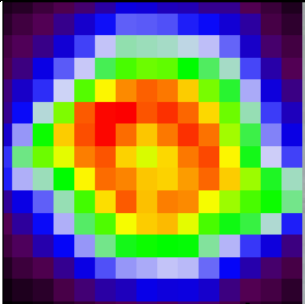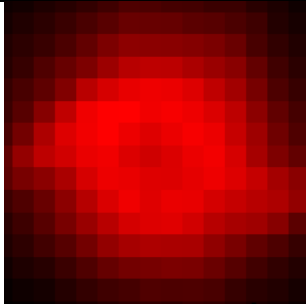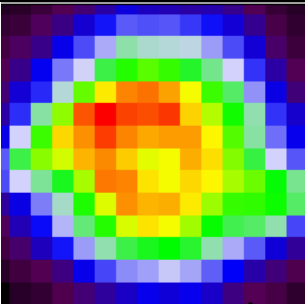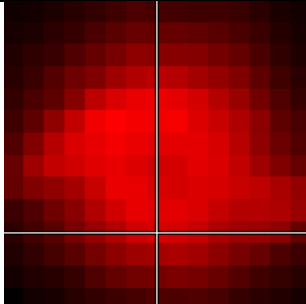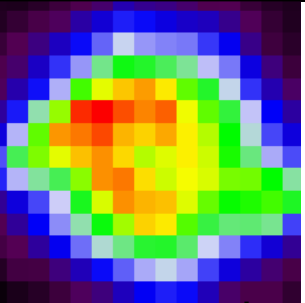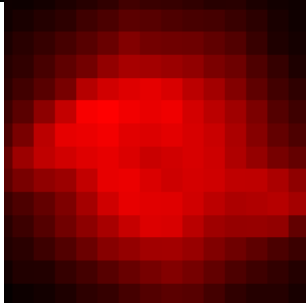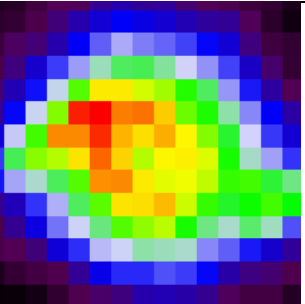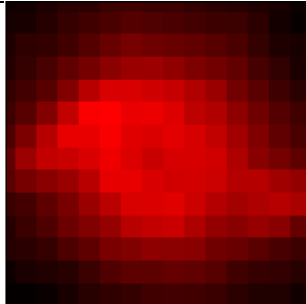
Position	Raman shift (cm^{-1})	Zirconia tetragonal phase peaks	
	559		
2	256		
	466		
	637		

Table 5.6 Micro-Raman mapping of the indentation induced phase transformation for a 1 kg indented $Ce_{11}ZA_{16}$ sample at point 2 from the map of figure 5.15

Position	Raman shift (cm^{-1})	Zirconia monoclinic phase peaks	
3	178		
	190		
	375		
	534		
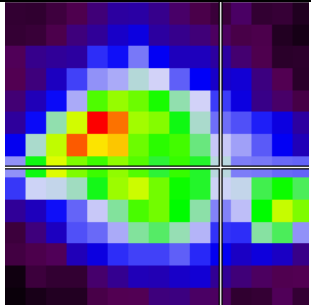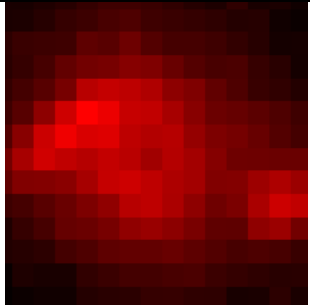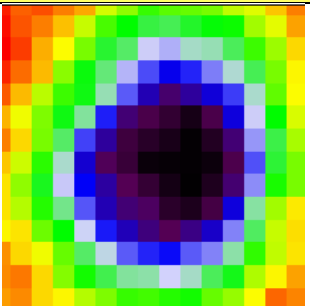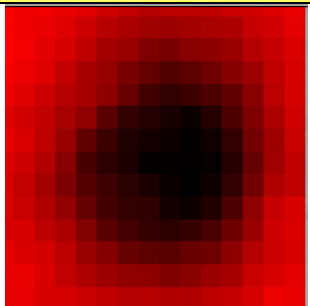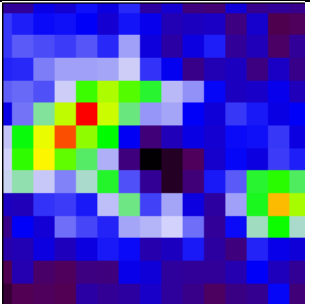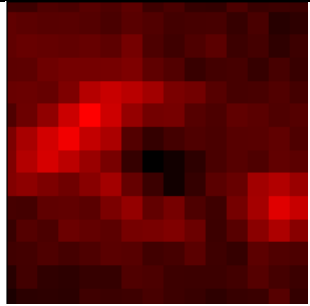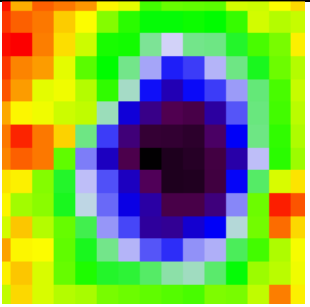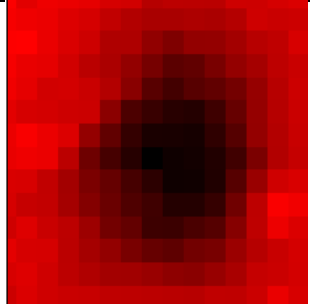
Position	Raman shift (cm^{-1})	Zirconia tetragonal phase	
	559		
3	256		
	466		
	637		

Table 5.7 Micro-Raman mapping of the indentation induced phase transformation for a 1 kg indented $Ce_{11}ZA_{16}$ sample at point 3 from the map of figure 5.15

5.3.4.1 Transformability of $Ce_{11}ZA_{16}$

As stated in chapter 1, tetragonal to monoclinic phase transformation is the basis of the toughness of ATZ composites. Zirconia provides toughness also due to the interaction of the crack front with microcracks induced by the t-m transformation, while alumina gives high strength [48]. In order to study the transformability, printed bars with the formulation 78 wt% + 2.5% Disperbyk-103, sintered at 1500 °C/ 1 h were submitted to the X-Ray Diffraction analysis (XRD). The fractured surfaces of bars after the 3-point bending test were analysed and compared with polished and thermal etched surfaces before the mentioned mechanical test to check the starting and final tetragonal amount. A high transformability was revealed, since the monoclinic phase, absent on the sample's surface, was preponderant on the fracture surface (figure 5.14). A monoclinic volume fraction of 82 vol% was detected on the fracture surface, while the bar's polished upper surface was fully tetragonal, confirming the reliability of the printing process.
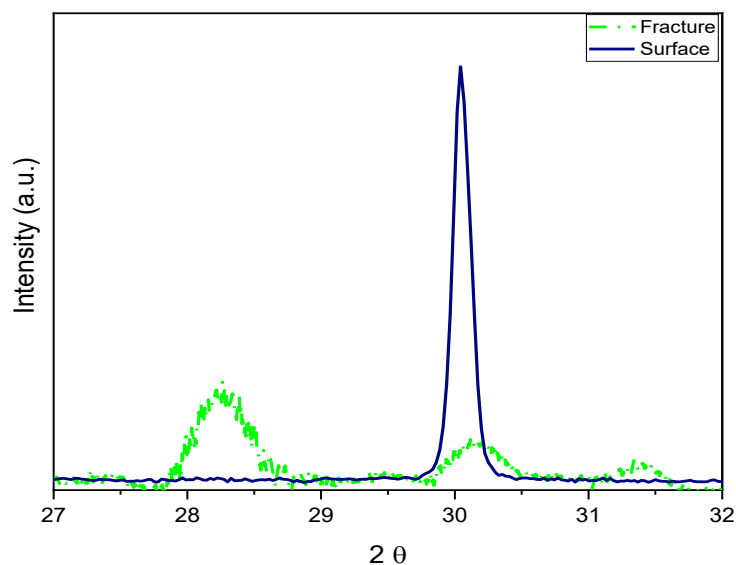
Figure 5.14 X-ray diffraction pattern of the printed bar's fracture surface, after a 3-point bending test (dotted green line) compared with the bar's polished upper surface (solid blue line)

5.4 Conclusions

In this last chapter, fully dense $Ce_{11}ZA_{16}$ composites with a low monoclinic volume fraction were obtained by DLP-stereolithography.

In the first part of the chapter, post-printing treatments such as water debinding and thermal debinding, were analysed in depth. The debinding process with water results as the best option compared to the debinding with solvents such as DBE (dibasic ester), isopropanol, or ethanol. The defects generated from the post-treatment and the best solutions found to reduce them or to maintain them under control were discussed as well.

The sintering behaviour of the green bodies was investigated by microstructural evolution and dilatometric analysis; a linear shrinkage of about 26% and 22% was found in the printed and pressed samples, respectively.

The grain size was measured with the aim to evaluate the influence of the solid loading and the sintering temperature on the zirconia and alumina grains' growth. The sintering cycle at 1500 °C/1 hour was found to be the best compromise for the restriction of the grains' growth.

In the second part, the characterization in terms of transformability and mechanical properties was reported.

The printed samples with the formulation 78 wt% +2.5 Disperbyk-103 showed a Vickers microhardness of ~15 GPa, in line with the values found in the literature for the ATZ materials produced with the same technique.

Micro-Raman spectroscopy and mapping were utilized effectively to investigate the spatial distribution of indentation-induced phase ZrO_2 transformations. The excellent spatial resolution of the instrument permitted the mapping of the transformed monoclinic phase in and around the indentations. The monoclinic peaks intensity increased closer to the indentation.

Three-point bending tests were performed on printed bars with the formulation 78 wt% +2.5 Disperbyk-103 showed a reasonably good bending strength of 436 ± 28 MPa, considering the fact that the samples were not polished.

Further studies will be necessary to better tailor the printing process and improve the mechanical properties, but the potential of the material is very high.

References

1. Yang, W. W., Yang, K. Y., Wang, M. C. & Hon, M. H. Solvent debinding mechanism for alumina injection molded compacts with water-soluble binders. *Ceram. Int.* **29**, 745–756 (2003).

2. Chen, G., Cao, P., Wen, G. & Edmonds, N. Debinding behaviour of a water soluble PEG/PMMA binder for Ti metal injection moulding. *Mater. Chem. Phys.* **139**, 557–565 (2013).

3. Hayat, M. D., Wen, G., Zulkifli, M. F. & Cao, P. Effect of PEG molecular weight on rheological properties of Ti-MIM feedstocks and water debinding behaviour. *Powder Technol.* **270**, 296–301 (2015).

4. Lotfizarei, Z., Mostafapour, A., Barari, A., Jalili, A. & Patterson, A. E. Overview of debinding methods for parts manufactured using powder material extrusion. *Addit. Manuf.* **61**, 103335 (2023).

5. Hsiang, H. I. *et al.* Polycrystalline alumina ceramic fabrication using digital stereolithographic light process. *Ceram. Int.* (2021). doi:10.1016/j.ceramint.2021.08.293

6. Johansson, E., Lidström, O., Johansson, J., Lyckfeldt, O. & Adolfsson, E. Influence of resin composition on the defect formation in alumina manufactured by stereolithography. *Materials (Basel).* **10**, (2017).

7. Santoliquido, O., Camerota, F. & Ortona, A. The influence of topology on DLP 3D printing, debinding and sintering of ceramic periodic architectures designed to replace bulky components. *Open Ceram.* (2021). doi:10.1016/j.oceram.2021.100059

8. Karalekas, D., Rapti, D., Gdoutos, E. E. & Aggelopoulos, A. Investigation of shrinkage-induced stresses in stereolithography photo-curable resins. *Exp. Mech.* (2002). doi:10.1177/001448502321548283

9. Chaim, R., Levin, M., Shlayer, A. & Estournes, C. Sintering and

densification of nanocrystalline ceramic oxide powders: A review. *Adv. Appl. Ceram.* **107**, 159–169 (2008).

10. Fournier, S. *et al.* Ceria-stabilized zirconia-based composites printed by stereolithography: Impact of the processing method on the ductile behaviour and its transformation features. *J. Eur. Ceram. Soc.* (2022). doi:10.1016/j.jeurceramsoc.2022.11.006

11. Chevalier, J. & Gremillard, L. *Zirconia as a biomaterial*. *Comprehensive Biomaterials* **1**, (Elsevier Ltd., 2011).

12. Lawson, S. Environmental degradation of zirconia ceramics. *J. Eur. Ceram. Soc.* **15**, 485–502 (1995).

13. Chevalier, J. & Gremillard, L. *Zirconia ceramics. Bioceramics and their Clinical Applications* (Woodhead Publishing Limited, 2008). doi:10.1533/9781845694227.2.243

14. Chevalier, J. & Gremillard, L. Zirconia as a biomaterial. In: Comprehensive Biomaterials. in 95–108 (Elsevier, 2011).

15. Liu, T., Mai, Y. W., Swain, M. V. & Grathwohl, G. Effects of grain size and specimen geometry on the transformation and R-curve behaviour of 9Ce-TZP ceramics. *J. Mater. Sci.* **29**, 835–843 (1994).

16. Wang, L., Yu, H., Hao, Z., Tang, W. & Dou, R. Fabrication of highly translucent yttria-stabilized zirconia ceramics using stereolithography-based additive manufacturing. *Ceram. Int.* (2023). doi:10.1016/j.ceramint.2023.02.081

17. Tsukuma, K. & Shimada, M. Strength, fracture toughness and Vickers hardness of CeO2-stabilized tetragonal ZrO2 polycrystals (Ce-TZP). *J. Mater. Sci.* **20**, 1178–1184 (1985).

18. Yu, Y. *et al.* Microstructural evolution and mechanical properties of nano-ATZ ceramics by solid solution precipitation. *J. Mater. Res. Technol.* **16**, 1293–1304 (2022).

19. Zhang, J., Liu, F., Liu, P. & He, D. Transparent Alumina Nanoceramics Prepared under High Pressure and Low Temperature. **2101413**, 1–6 (2023).

20. Chuah, Y. D. & Teng, W. D. 1 P re r f. (2023). doi:10.1016/j.ceramint.2023.05.011

21. Xia, X. & Duan, G. Effect of solid loading on properties of zirconia ceramic by direct ink writing. *Mater. Res. Express* **8**, (2021).

22. Mu, Y. *et al.* Effect of synergism of solid loading and sintering temperature on microstructural evolution and mechanical properties of 60 vol% high solid loading ceramic core obtained through stereolithography 3D printing. *J. Eur. Ceram. Soc.* **43**, 661–675 (2023).

23. Fornabaio, M. Composites in the Alumina-Zirconia system: an engineering approach for an effective tailoring of microstructural features and performances. (Politecnico di Torino, 2014).

24. Chinn, R. E. *Ceramography: Preparation and Analysis of Ceramic Microstructures*. (ASM International, 2002).

25. Reveron, H. *et al.* Towards long lasting zirconia-based composites for dental implants: Transformation induced plasticity and its consequence on ceramic reliability. *Acta Biomater.* **48**, 423–432 (2017).

26. Nawa, M., Nakamoto, S., Sekino, T. & Niihara, K. Tough and Strong Ce-TZP/Alumina Nanocomposites Doped with Titania. *Ceram. Int.* **24**, 497–506 (1998).

27. Coppola, B., Lacondemine, T., Tardivat, C., Montanaro, L. & Palmero, P. Designing alumina-zirconia composites by DLP-based stereolithography: Microstructural tailoring and mechanical performances. *Ceram. Int.* **47**, 13457–13468 (2021).

28. Zhu, L. *et al.* Microstructure, mechanical properties, friction and wear performance, and cytotoxicity of additively manufactured zirconia-toughened alumina for dental applications. *Compos. Part B Eng.* **250**, 110459 (2023).

29. Wu, H. *et al.* Fabrication of dense zirconia-toughened alumina ceramics through a stereolithography-based additive manufacturing. *Ceram. Int.* **43**, 968–972 (2017).

30. Wang, L., Yao, L., Tang, W. & Dou, R. Effect of Fe2O3 doping on color and mechanical properties of dental 3Y-TZP ceramics fabricated by stereolithography-based additive manufacturing. *Ceram. Int.* 1–11 (2022). doi:10.1016/j.ceramint.2022.12.062

31. He, R. *et al.* Fabrication of complex-shaped zirconia ceramic parts via a DLP- stereolithography-based 3D printing method. *Ceram. Int.* (2018). doi:10.1016/j.ceramint.2017.11.135

32. Tan, X. *et al.* Effect of high-speed sintering on the microstructure, mechanical properties and ageing resistance of stereolithographic additive-manufactured zirconia. *Ceram. Int.* **48**, 9797–9804 (2022).

33. Zhao, R., Liu, X., Li, H., Song, L. & Ma, J. Stronger and tougher nanosized dense ceria-doped tetragonal zirconia polycrystals by sinter-HIP. *J. Eur. Ceram. Soc.* **43**, 2282–2288 (2022).

34. Olhero, S. M. *et al.* Conventional versus additive manufacturing in the structural performance of dense alumina-zirconia ceramics: 20 years of research, challenges and future perspectives. *J. Manuf. Process.* **77**, 838–879 (2022).

35. Tovar-Vargas, D., Roitero, E., Anglada, M., Jiménez-Piqué, E. & Reveron, H. Mechanical properties of ceria-calcia stabilized zirconia ceramics with alumina additions. *J. Eur. Ceram. Soc.* **41**, 5602–5612 (2021).

36. Ponnilavan, V. & Kannan, S. Structural, morphological and mechanical characteristics on the role of excess ceria additions in zirconia toughened alumina systems. *J. Alloys Compd.* **694**, 1073–1082 (2017).

37. Zhao, R., Liu, X., Li, H., Song, L. & Ma, J. Stronger and tougher nanosized dense ceria-doped tetragonal zirconia polycrystals by sinter-HIP. *J. Eur. Ceram. Soc.* **43**, 2282–2288 (2023).

38. Borlaf, M., Szubra, N., Serra-Capdevila, A., Kubiak, W. W. & Graule, T. Fabrication of ZrO2 and ATZ materials via UV-LCM-DLP additive manufacturing technology. *J. Eur. Ceram. Soc.* **40**, 1574–1581 (2020).

39. Zheng, T., Wang, W., Sun, J., Liu, J. & Bai, J. Development and evaluation

of Al2O3–ZrO2 composite processed by digital light 3D printing. *Ceram. Int.* **46**, 8682–8688 (2020).

40. Wu, H. *et al.* Sintering kinetics involving densification and grain growth of 3D printed Ce–ZrO2/Al2O3. *Mater. Chem. Phys.* **239**, 1–6 (2020).

41. Willems, E. *et al.* Additive manufacturing of zirconia ceramics by material jetting. *J. Eur. Ceram. Soc.* **41**, 5292–5306 (2021).

42. Courtois, N. Développement de nouveaux matéeriaux céramiques à base de zircone pour application dentaire. (Institute National des Sciences Appliquées de Lyon, 2011).

43. Toraya, H., Yoshimura, M. & Somiya, S. Calibration Curve for Quantitative Analysis of the Monoclinic-Tetragonal ZrO2 System by X-Ray Diffraction. *J. Am. Ceram. Soc.* **67**, C-119-C-121 (1984).

44. CLAUSSEN, N. Fracture Toughness of Al2O3 with an Unstabilized ZrO2Dispersed Phase. *J. Am. Ceram. Soc.* **59**, 49–51 (1976).

45. Hirata, T. Raman-active modes and the tetragonal-monoclinic phase transition in ZrO2 doped with 12mol% CeO2. *J. Phys. Chem. Solids* **56**, 951–957 (1995).

46. Wulfman, C., Sadoun, M. & Lamy De La Chapelle, M. Interest of Raman spectroscopy for the study of dental material: The zirconia material example. *Irbm* **31**, 257–262 (2010).

47. Paul, A., Vaidhyanathan, B. & Binner, J. Micro-Raman spectroscopy of indentation induced phase transformation in nanozirconia ceramics. *Adv. Appl. Ceram.* **110**, 114–119 (2011).

48. Hannink, R. H. J., Kelly, P. M. & Muddle, B. C. Transformation toughening in zirconia-containing ceramics. *J. Am. Ceram. Soc.* **83**, 461–487 (2000).

Chapter 6

General Conclusions and Perspectives

This chapter concludes the study, summarizing the major results in connection to the research objectives and questions and analysing their importance and contribution. Additionally, it will discuss the short comings of the study and suggest areas for future investigation.

The main aim of the present PhD project was to exploit Digital Light Processing (DLP) Stereolithography to investigate the printability of composites in the zirconia-alumina system with appropriate compositional and microstructural characteristics for the purpose of tailoring physical and mechanical features. The novelty of this research topic is that the current applications of DLP-stereolithography are based on the 3D printing of yttria-stabilized tetragonal zirconia (Y-TZP), while few works in the scientific literature have reported on the printability of $Ce-ZrO_2/Al_2O_3$ composites through DLP. Zirconia-alumina composites display a strategic combination of mechanical properties: alumina shows outstanding hardness and wear resistance, while zirconia presents remarkable bending strength and fracture toughness, paving the way for several applications in the biomedical, orthopedic, and dental fields.

In the first chapter of the thesis, an introduction was given to the transformation toughening property of zirconia and the beneficial effect of alumina addition in the powder composition, and the advantageous influence of ceria in the aging resistance of zirconia. After that, the 3D printing technology used in this work, i.e. Digital Light Processing (DLP) was described in detail.

The first part of the research activity was devoted to the preparation and characterization of zirconia-based composite powders suitable for the preparation of printable slurries. The dispersion process of the powders was carried out through wet ball-milling, obtaining powders with a particle size distribution below 1 μm, suitable for the preparation of slurries with a low viscosity.

In detail, in the second chapter, Ce-TZP based bi-phase materials, particularly 84 vol% ZrO_2 (11 mol% CeO_2) and 16 vol% Al_2O_3 (denoted $Ce_{11}ZA_{16}$), was successfully prepared. A study of the dispersibility was carried out and a good dispersion with a monomodal narrow particle size distribution was reached after 18 hours of ball-milling. The suspension was dried on a hot plate magnetic stirrer until the evaporation of the liquid medium and then sieved down to 125 μm.

In the third chapter, the procedure for obtaining the three-phase composites (referred to as $Ce_{11}ZA_8Sr_8$) was described. More in detail, 11 mol% ceria-stabilized ZrO_2 (a mix of the 10 mol% and the 12 mol% ceria-stabilized ZrO_2 powder) was dispersed in water to achieve a fine particle size distribution. Afterward, the inorganic precursors of the secondary phases, round-shaped $α$-Al_2O_3 and elongated $SrAl_{12}O_{19}$, were dissolved in distilled water and drop-wised into the ceramic slurry, the former for retaining the zirconia grain growth during sintering, and the latter for further improving the fracture toughness of the material.

The doped suspension was then homogenized under magnetic stirring and spray-dried to induce the precipitation of the precursors onto the surface of the zirconia particles by liquid evaporation. The powder obtained was then thermal treated to produce the crystallization of the second phases.

The second part of the activity was focused on the preparation of slurries at several solid loadings with $Ce_{11}ZA_{16}$ or $Ce_{11}ZA_8Sr_8$ as matrix powders. The ambitious goal of this part of the research was to obtain high solid loading slurries which were particularly homogeneous and stable. A high solid loading slurry is in fact beneficial to obtain a high green and sintered density, and to reduce the shrinkage during the sintering step. A key aspect of this slurry is its low viscosity (3000 mPa.s at the operative shear rate) and a shear-thinning behavior. In this way, the slurry

can be properly spread on the foil during the layer-by-layer printing process of an object, preventing its spontaneous flow and achieving a uniform layer under the action of the doctor blade.

The behavior of the $Ce_{11}ZA_{16}$ slurries was explored first. As a preliminary study, dispersant-free slurries were prepared at 50.0 to 62.5 wt% solid loadings. A second set of slurries was prepared with the addition of 1.0–4.0 wt% dispersant (with respect to the dry powder), which allowed particle–particle interactions to be managed and a low viscosity to be maintained to achieve solid loadings in the range of 65 to 80 wt%. Finally, the slurries were printed, and the as-obtained samples were submitted to the debinding and sintering treatments. Bars suitable for mechanical characterization were then produced.

Through PCA analysis, the most convincing slurry formulation suitable for the production of parts with favorable mechanical properties was identified. The most promising slurry formulation for $Ce_{11}ZA_{16}$ was 78 % of solid load with the addition of 2.5 wt% Disperbyk-103 as dispersant. The optimized slurry had a viscosity of 2.8 Pa s at a shear rate of 160 s^{-1}. The maximum density was achieved at 78 wt% solid loading, providing values of 98.3 % and 99.4 % after firing at 1500 ◦C/1 h and 1550 ◦C/1 h, respectively.

With the tri-phasic $Ce_{11}ZA_8Sr_8$ composition, sintered samples were obtained with a TD% of 96 % and 96.6 % at 1500 ◦C/1 h and 1550 ◦C/1 h, respectively. The maximum density was achieved again with the 78 wt% + 2.5 Disperbyk-103 slurry. The most important limitation in printing the $Ce_{11}ZA_8Sr_8$ lies in the fact that the procedure to obtain the amount of the composite powder, sufficient for only one print, was time-consuming and the several steps necessary for the preparation could introduce variables that are difficult to manage and control in the whole process.

The most challenging goal of the tri-phasic powder was achieved, i.e. the crystallization of the second phases in the matrix ZrO_2 powder, but in the printed parts some printing flaws were still present, impeding the mechanical characterization. Notwithstanding these limitations, this work offers valuable and fruitful insights for further researches.

Further research might explore the printability of $Ce_{11}ZA_8Sr_8$ by using a commercial tri-phasic powder in order to focus on the optimization of the printing process, and on reducing the printing flaws with the aim of obtaining homogeneous microstructure and a fully dense material with mechanical properties suitable for biomedical application.

Another limitation of this study was the occurrence of delamination of the sample during the water debinding step. Actually, the factors leading to delamination took place well beforehand, mainly being bubbles between the new layers and the previous one, insufficient power of the UV light, which does not allow a firm cohesion between the layers, shrinkage of the sample, and inhomogeneous slurry. In this work, great effort was dedicated to controlling all these variables and the PCA analysis helped a lot in this regard. The delamination was greatly reduced, even if not completely, but bending and cracks, as well as printing flaws characteristic of the stereolithographic process, were totally avoided. These findings provide interesting inputs for future research and pave the way to obtaining delamination-free samples. Further research should be undertaken to explore how to obtain thicker layers (hindered by the presence of Ceria, a known UV-blocking material), for example by the addition to the slurry of some additives that avoids this negative aspect.

In the last section, the sintering behavior of the $Ce_{11}ZA_{16}$ green bodies was investigated by microstructural evolution and dilatometric analysis; a linear shrinkage of about 26% was found.

The grain size was measured with the aim of evaluating the influence of the solid loading and the sintering temperature on the zirconia and alumina grains' growth. The sintering cycle at 1500 °C/1 hour was found to be the best compromise for the restriction of the grains' growth. The characterization in terms of transformability and mechanical properties was reported.

The printed samples with the formulation 78 wt% +2.5 Disperbyk-103 showed a Vickers microhardness of ~15 GPa, in line with the values found in the literature for the ATZ materials produced with the same technique.

Micro-Raman spectroscopy and mapping were utilized to investigate the spatial distribution of indentation-induced phase ZrO_2 transformations. The mapping of the transformed monoclinic phase in and around the indentations was done. The monoclinic peaks intensity increased closer to the indentation.

Three-point bending tests were performed on printed bars with the formulation 78 wt% +2.5 Disperbyk-103 showed a reasonably good bending strength of 436 ± 28 MPa, considering the fact that the samples were not polished.

Undertaking this thesis project has proven that deep knowledge of all the mechanisms involved in the stereolithographic process is fundamental for achieving a full control of the microstructural features of the final printed parts.

It has highlighted the importance of an engineering approach and how the tailoring of the composite powders affects the properties of the final printed parts.

The reputation of zirconia as a biocompatible material undoubtedly opens the doors to the development of materials for biomedical applications.

However, these devices must fulfil strict requirements in terms of cytocompatibility and dimension of the objects. In the near future, the high resolution of DLP-stereolithography could be exploited to produce biomedical devices tailored to every single patient, avoiding the current invasive methods.

A preliminary study on the technological transfer at the industrial level of the procedure described could be done to avoid reproducibility issues that could arise due to the "laboratory scale" utilized. Furthermore, the same elaboration route could be extended to other ceramic composites.